Characterization Techniques for Aggregated Nanomaterials in Biological and Environmental Systems

A Dissertation
SUBMITTED TO THE FACULTY OF
UNIVERSITY OF MINNESOTA
BY

Seongho Jeon

IN PARTIAL FULFILLMENT OF THE REQUIREMENTS
FOR THE DEGREE OF
DOCTOR OF PHILOSOPHY

Professor Christopher J Hogan Jr.

June 2016

Acknowledgements

Foremost, I would like to express my sincere gratitude to my advisor (maybe more than this) Prof. Chris Hogan for the continuous support of my PhD studies from 2012 spring to 2016 summer. He directed my graduate work with patience, motivation, enthusiasm, and immense knowledge. Besides my advisor, I would like to thank the rest of my dissertation committee: Prof. Cari Dutcher, Prof. John Bischof, and Prof. Christy Haynes for their encouragement and insightful comments on my PhD studies.

My sincere thanks also go to Prof. Carlos Larriba, Prof. Ranga Gopalakrishnan, Dr. Thaseem Thajudeen, Dr. Siqin He, Dr. Anne Maisser and Dr. Hui Ouyang for helping me to be on the right track of PhD studies all the time. I also want to say 'thank you' to Gary Van Schooneveld and Dr. Derek Oberreit for giving me opportunities to experience highly advanced aerosol techniques.

I have special thanks to Vivek Rawat who had four years with me in Nanoparticle Physics Laboratory, sharing lots of unforgettable moments. I also want to show appreciation to Jikku Thomas and David Buckley for many valuable scientific discussions and all the fun we have had together. I also thank our lab junior members Chenxi Li, Xiaoshuang Chen and Huan Yang, and I hope you guys will have wonderful PhD studies in next three or four years. My thankfulness should reach to MN Futures group people. In particular, I am grateful to Dr. Katie Hurley, Dr. Michael Etheridge, Dr. Zhe Gao and Connie Chung for helping iron oxide nanoparticle studies.

Last but not the least, I would like to thank my parents and my sister for supporting me both financially and spiritually throughout my life. Finally, I would like to thank all people around me when I was toward the PhD degree in University of Minnesota, twin cities from 2011 September to 2016 June.

Thank you Again!!

Seungho Jeon

To

My parents

Abstract

Nanoparticles, which are defined as objects with characteristic lengths in the 10^{-9} – 10^{-7} m (nanoscale) size range, are used with increasing frequency in a wide of applications, leading to increases in nanomaterial interactions with biological and environmental systems. There is therefore considerable interest in studying the influence nanomaterials can have when inside the human body or dispersed in the ambient environment. However, nanoparticles persist as homo aggregates or heterogeneous mixtures with organic matters, such as proteins, in biological and environmental systems. A large and growing body of research confirm that nanomaterial morphology as well as the degree of aggregation between nanomaterials influences nanomaterial interactions with their surroundings. Specifically, the structures/morphologies of nanoparticles determine their overall surface areas and corresponding surface reactivity (e.g. their catalytic activity). Nanoparticle transport properties (e.g. diffusion coefficient and extent of cellular uptake) are also determined by both their structures and surface properties. Unfortunately, techniques to characterize nanomaterial size and shape quantitatively, when nanomaterials have complex geometries or persist as aggregates, are lacking. Hydrodynamic sizes of nanoparticles and their aggregates can be inferred by dynamic light scattering (DLS) or nanoparticle tracking analysis (NTA). However, since these techniques are relied on the scattering light intensity properties, sizes of polydisperse sub 30 nm particles cannot be effectively measured in those techniques. For structure inference of aggregated nanomaterials, microscopy images have been used for qualitative visual analysis, but the quantitative morphology analysis technique is yet to be developed. Five studies in this dissertation are hence aimed to develop

new techniques to provide improved morphology characterization of aggregated nanomaterials in various biological and environmental colloidal systems. Aggregation mechanism and behavior of nanoparticles in surrounding were examined as a function of their quantified aggregate morphologies. The first three studies (Chapters 2, 3, and 4) introduced a new gas-phase particle size measurement system, a liquid nebulization-ion mobility spectrometry (LN-IMS) technique, to characterize nanomaterials (down to 5 nm in characteristic size) and nanoparticle-protein conjugates. In other two studies (Chapters 5 and 6), three dimensional structures of homo-aggregates were quantified with the fractal aggregate model, and resulted fractal structures of aggregates were correlated to their transport properties in surroundings.

Table of Contents

List of Tables

List of Figures

Chapter 1 Introduction

1.1 Motivation

Nanoparticles or nanomaterials, which are defined as objects with characteristic lengths in the 10^{-9} – 10^{-7} m (nanoscale) size range, are widely used in industrial products such as cosmetics [1, 2], paints [3], food ingredients [4, 5], pharmaceuticals [6-8], and heat transfer media [9]. In addition, nanoparticles have shown high potential in biomedical applications [10], such as in cancer treatment [11-13] and in acting as optical sensors [14, 15]. These latter applications of nanoparticles necessitate investigation of their physical properties in biological media and in the ambient environment, as after use nanoparticles may be released into ambient water and soil systems. Nanoparticle physical properties, which include size, shape, extent of aggregation and aggregate morphology, as well as surface characteristics, strongly influence nanoparticle performance and the influence they have on their surroundings [16]. Specifically, the structures/morphologies of nanoparticles determine their overall surface areas and corresponding surface reactivity [17, 18] (e.g. their catalytic activity). Nanoparticle transport properties (e.g. diffusion coefficient [19, 20] and extent of cellular uptake [21, 22]) are also determined by both their structures and surface properties. A growing number of studies in nanomedicine [23, 24] and nanotoxicology [25] confirm that the behavior of nanoparticles and the influence they have on their environment is strongly affected by their morphological states and their chemical compositions. Therefore, accurate morphological analysis of nanomaterials is required in wide variety of circumstances.

However, in large part, synthesized nanomaterials are not morphologically and structurally characterized in the media in which they will be applied or dispersed.

Subsequent to synthesis, most nanoparticles are dispersed with a surfactant in a solvent where aggregation between particles or with other species is prevented (through either electrostatic or steric stabilization) [26-29]. Such stabilization is not always possible in biological systems and in the ambient environment, as the solvent, pH, ionic strength, and surfactant concentration are not controllable in these circumstances [28, 30, 31]. Nanoparticles in these environments, including the blood stream and natural water bodies, hence often persist as aggregates, which are large clusters with random and complex structures [29, 32, 33]. Aggregates may be composed solely of nanoparticles of one type (homoaggregates) or may be composed of nanoparticles and macromolecules/proteins [34, 35] deriving from their surroundings (heteroaggregates). Examples of homoaggregates aggregates are depicted in Figure 1.1. Irrespective of whether aggregates are homogeneous or heterogeneous in composition, their existence complicates both physical characterization and subsequent prediction of nanoparticle behavior [32, 36].

The need to characterize the onset of aggregation, as well as aggregate morphology is the main motivation for the work performed in this dissertation. Five specific studies were performed to develop new approaches to characterize nanoparticles/nanomaterials in aqueous systems: (1) Development of a liquid nebulization-ion mobility spectrometry (LN-IMS) technique for the characterization of nanomaterials (down to 5 nm in characteristic size) in aqueous systems, (2) application of the LN-IMS system to quantify binding of bovine serum albumin to gold nanoparticles (the onset of heteroaggregation), (3) application of the LN-IMS system to quantify bovine serum albumin binding to superparamagnetic iron oxide nanoparticles, (4) development of an image processing technique to characterize the extent of aggregation of nanomaterials in intracellular and

extracellular media (using cyro-electron microscopy images), and (5) the development of non-invasive approaches to characterize the extent of aggregation of nanomaterials in high volume fraction (1%) nanoparticles slurries. The specific objectives of each of these studies are discussed in the following section. Subsequent to this, a brief overview of the characterization techniques to be employed is provided in this chapter. Chapters 2-6 describe the individual studies. Each chapter is intended to be a stand-alone contribution (adapted from a published, peer-reviewed manuscript, or a manuscript in preparation for submission), with its own abstract, introduction, methods, results & discussion, conclusions, and references section. For this reason, some information contained in each chapter is repetitive with prior chapters. A general description of conclusions of all described studies and future prospects is provided in Chapter 7.

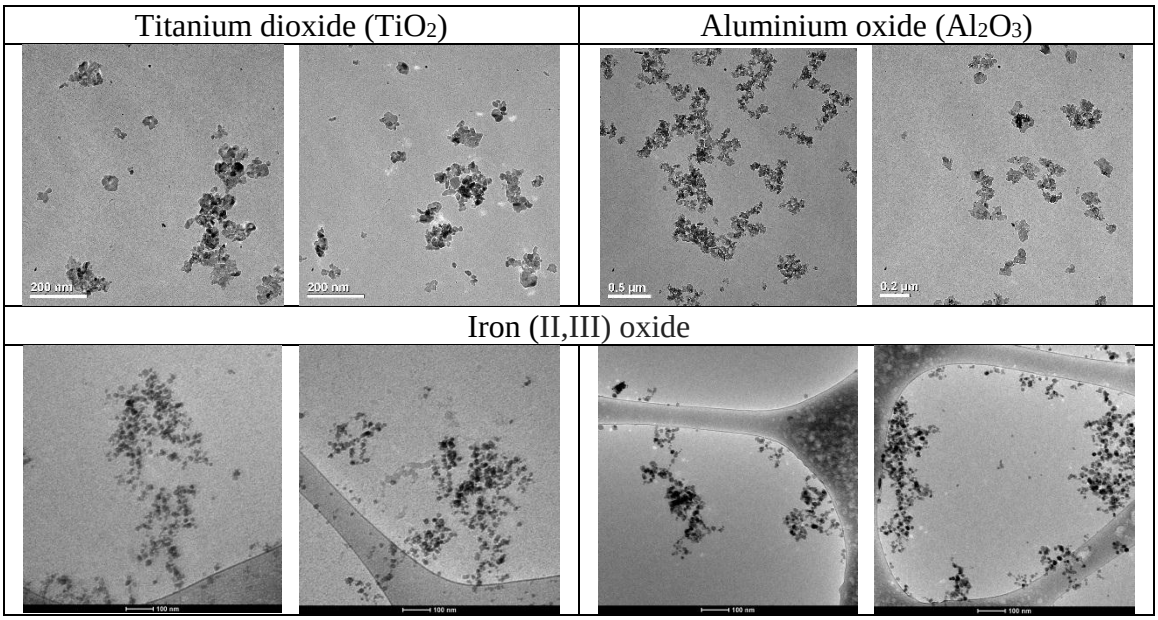

Figure 1.1. Selected transmission electron micrographs of aggregate nanomaterials. TiO_2 and Al_2O_3: standard transmission electron microscopy of aggregates dried from aqueous suspension. Iron Oxide: Cryo-EM images of aggregates in aqueous suspension.

1.2 Objectives

The objectives of the studies performed are as follows:

Chapter 2: Chapter 2 focuses on the application of a liquid nebulizer (LN) with online dilution using ultra-high purity water to transition hydrosol particles to aerosol particles. This transition enables size distribution function analysis via ion mobility spectrometry (IMS), a technique typically restricted to electrosprayed macromolecules and small organic compounds. Importantly, it is shown that ion mobility spectrometry can be used to quantify the sizes of both spherical and non-spherical (nanorod) materials, their size distributions are preserved during the hydrosol to aerosol transition, and that a size and material independent calibration curve linking measurement concentrations in the gas phase to the liquid phase concentration can be developed.

Chapter 3: Chapter 3 focuses on application of the LN-IMS system described in chapter 2 to examine the onset of heteroaggregation between gold nanoparticles (nominal diameters of 20 nm, 30 nm, and 50 nm) and bovine serum albumin. A Langmuir-like adsorption model is applied in analyzing results and is used to infer the binding site surface density (proteins per unit area) on gold nanoparticles as well as effective protein concentration above binding sites (which determines the dissociation rate). Results are found to be in good agreement with binding site density measured by alternative techniques, verifying that the LN-IMS system can be used to quantify heteroaggregate formation. Further, through constant number Monte Carlo modeling, a demonstration of how IMS inferred size distribution functions evolves for irreversible binding, reversible binding, and coagulation.

Chapter 4: With the ability to examine protein binding via LN-IMS measurement

established in Chapter 3, in Chapter 4 the extent of bovine serum albumin binding to superparamagnetic iron oxide particles and the formation of serum albumin-iron oxide heteroaggregates is quantified. The extent of aggregation is correlated with extent of heat generated when particles are placed with an alternating magnetic field. The extent of protein absorption on bare iron oxide is compared to that on mesoporous silica coated and PEGylated iron oxide nanoparticles.

Chapter 5: Chapter 5 focuses on the application of an image processing technique to extrapolate probable 3-dimensional structures for aggregates observed in 2-d dimensional electron microscopy image to infer the morphologies of iron oxide aggregates in intra- and extracellular environments of LNCaP cells. For morphological quantification aggregates are assumed to be quasifractal in nature, in which there is a power law relationship between the number of particles in an aggregate and the aggregate's radius of gyration (where the exponent is termed the fractal dimension).

Chapter 6: Chapter 6 focuses on the application of nanoparticle tracking analysis as well as viscosity measurements to develop a data inversion approach to infer the most probably fractal dimension for aggregates within a nanoparticle slurry.

1.3 Nanoparticle morphology characterization techniques

1.3.1 Nanomaterial size characterization techniques

First and foremost, nanoparticles are characterized by a relative size, which is most the diameter for spherical particles and a measurement equivalent diameter for non-spherical particles. The size distribution function for a suspension quantifies the variation in particle number concentration with measurement equivalent diameter. Here I describe

three methods for size distribution function inference and their present limitations; the latter two of these are employed in the studies described in later chapters. A number of alternative size distribution measurement techniques which are not employed in this study, are briefly mentioned in the introduction subsections of individual chapters.

First, in the liquid phase, the size distribution function is frequently monitored using dynamic light scattering (DLS) [37-40], which is also referred to as photon correlation spectroscopy (PCS). The DLS technique relatively simple to apply with commercial instruments, and measurements only require a short period of time to complete. In this method, a nanosuspension is placed in the path of a laser beam, and the size distribution function is inferred from fluctuations of scattered light intensity due to the Brownian motion of nanoparticles (hence the equivalent diameter in DLS is a hydrodynamic diameter). DLS consistently yields accurate size measurements of monodisperse nanoparticles, i.e. those which have narrow distributed size distribution functions. However, DLS measurements are usually biased to larger particles because scattered light intensity is proportional to the sixth power of particle diameter [41-43]. For this reason DLS measurements are typically used for qualitative characterization; they are used to infer a mean equivalent diameter for particles, but there is considerable uncertainty in other properties inferred from these measurements.

The diffusion of particles is also monitored in recently developed Nanoparticle Tracking Analysis (NTA) [43-46], but unlike DLS, single particle motion is monitored. For this reason NTA results are less biased towards presence of large particles, and NTA is capable of distinguishing different size populations in mixture samples (i.e. polydisperse analysis is possible). Figure 1.2 displays the schematic of a NTA system and a captured

NTA video frame of Al_2O_3 nanoparticles in water as an example. While single particle measurement capability is a major advance over DLS, the minimum measurable nanoparticle size of NTA is approximately 30 nm [47-49]; particles smaller than this equivalent size do not scatter light sufficiently for detection, particularly in samples containing larger particles.

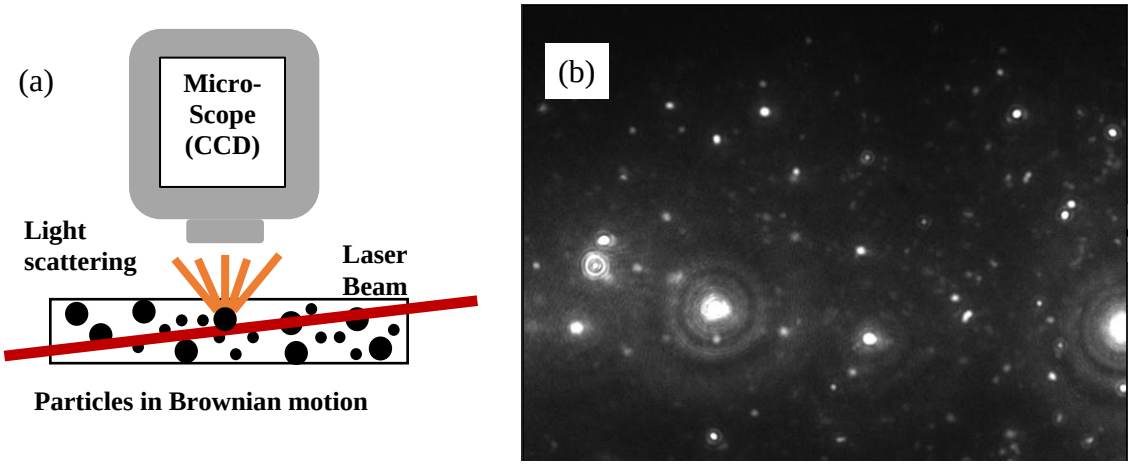

Figure 1.2. (a) Schematic of nanoparticle tracking analysis (NTA) system and (b) an example of the NTA video frame of nanoparticles (Al_2O_3) under Brownian motion captured by a CCD camera

The limitations of liquid phase measurements for smaller nanoparticles and polydisperse samples are not encountered with existing aerosol instrumentation. In aerosol science, the ion mobility spectrometry (IMS) technique, typically composed of a differential mobility analyzer (DMA) [50-52] and a condensation particle counter (CPC) [53, 54], has been commonly used for accurate aerosol particle size distribution characterization in a 2 – 500 nm range. DMAs act as mobility equivalent size filters; they isolate particles based on their electrical mobility (Z_p). Particle electrical mobility is expressed in Equation (1.1). This equation is derived from the balance between electrical

force and drag force on a particle [55, 56];

$$Z_p = \frac{neC_c}{3\pi\mu d_p} \tag{1.1}$$

where n is the number of unit charges on a particle (typically +1 or -1 for charge particles and a DMA only selects particles of a prescribed polarity), e is the unit electrical charge (1.6×10^{19} C), μ is the gas kinematic viscosity, C_c is the Cunningham slip correction factor and d_p is the mobility equivalent particle diameter. Upon being transmitted through a DMA, particles enter a CPC, wherein a working fluid vapor (typically water or butanol) condenses onto them, growing them to micrometer sizes, enabling size particle detection (with size known from the DMA) at the singe particle level. By systematically varying the electrical mobility selected by the DMA and measuring transmitted particle concentration with a CPC, aerosol nanoparticle size distribution functions can be monitored, and algorithms have been developed for both automated operation of these two instruments (as a scanning mobility particle spectrometer) [57, 58], and to directly invert the size distribution function from raw data. Though this type of IMS technique is applied almost universally to examine nanoparticles in the ambient atmosphere, emitted from combustion engines, and produced in gas phase synthesis systems. However, to apply the DMA-CPC technique to liquid suspensions, an appropriate device is necessary to convert colloidal particles into aerosols while preserving their size distribution functions [59, 60]. Demonstrations of liquid suspension to aerosol conversion have been made and are described in prior studies [60-62]; unfortunately a universal method (even for samples restricted aqueous suspensions) has not been developed.

1.3.2 Nanomaterial aggregate structure characterization techniques

Precise description of the geometries of aggregates, such as those depicted in Figure 1.1, is often not feasible, as there is a near-infinite set of possible morphologies, even for aggregates composed of tens of primary particles. Instead, for quantitative structural characterization of non-spherical aggregates, it is common (and more practical) adopt the quasi-fractal aggregate model. The most basic form of this model assumes that all aggregates are composed of identical primary particles, and they are spherical with without overlap. The quasi-fractal aggregate model can be described by the scaling law [63];

$$N_p = k_f \left(\frac{R_g}{a_p}\right)^{D_f} \tag{1.2}$$

where N_p is the number of primary particles in an aggregate, k_f is the pre-exponential factor, usually in the range from 1.0 to 2.0, R_g is the radius of gyration, a_p is the primary particle radius, and D_f is the fractal dimension. D_f can theoretically vary from 1.0 to 3.0, and lower fractal dimension aggregates are more chain-like, while higher fractal dimension aggregates are much more spherical. k_f has a much more subtle influence on the visible structure of an aggregate, is relate to the density of particles in the aggregate structure [64]. Therefore, D_f and k_f can be used as quantitative shape parameters of an aggregate, while N_p quantifies the size of an aggregate. Simulation techniques exist to produce aggregates computationally with prescribed D_f, k_f, and N_p. Figure 1.3 displays examples of simulated fractal aggregates with N_p= 20, 50, & 100, and selected D_f and k_f. As depicted in Figure 1.3, lower values of D_f and k_f lead more linear aggregates, while more dense aggregates have higher values of D_f and k_f.

	D_f 1.5	D_f 2.0	D_f 2.4
k_f 1.2	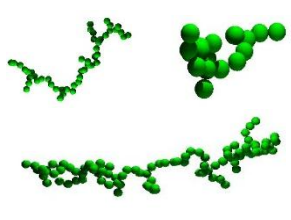	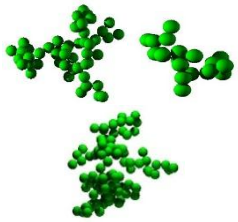	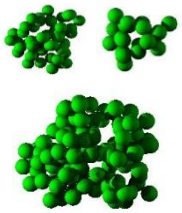
k_f 1.7		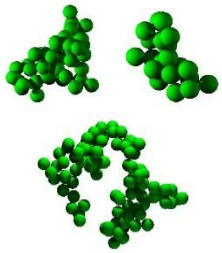	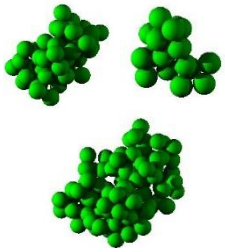

Figure 1.3. Computational generated (with a cluster-cluster algorithm, CCA) quasifractal aggregates with the noted fractal dimension (D_f) and pre-exponential factor (k_f).

There have been prior several attempts to infer fractal descriptors (D_f, k_f, and N_p) of aggregates by using transmission electron microscopy (TEM), primarily for soot particles generated in combustion systems [65-69]. In these studies two-dimensional (2D) geometric parameters of projected aggregates were measured and used to predict three dimensional (3D) structures. In other studies, empirical correlations have been developed between three-dimensional and two-dimensional projected properties with the fractal aggregate model. However, prior image analysis approaches relied on only one or two geometric parameters, leading to large uncertainties in the 3D structure of the examined aggregates. Additionally, the described studies were primarily focused on the prediction of D_f, not k_f and N_p, and were limited to a narrow D_f range. These limitations motivate the development of a more advanced image analysis technique in this dissertation.

1.4 Publications from this dissertation

As noted, subsequent chapters are adapted from works submitted, or to be submitted for peer-reviewed publication. At the time of writing this dissertation, several have also been accepted for published and published. The specific manuscript titles are:

Chapter 2
"Nanomaterial Size Distribution Analysis via Liquid Nebulization Coupled with Ion Mobility Spectrometry (LN-IMS)"
Seongho Jeon, Derek R. Oberreit, Gary Van Schooneveld, & Christopher J. Hogan Jr; Analyst, 2016, 141, 1363-1375

Chapter 3
"Liquid Nebulization-Ion Mobility Spectrometry Based Quantification of Nanoparticle-Protein Conjugate Formation" Seongho Jeon, Derek R. Oberreit, Gary Van Schooneveld, & Christopher J. Hogan Jr;
Submitted to Analytical Chemistry, 2016

Chapter 4
"Quantification of Surface Coating Dependent Binding of Serum Albumin to Superparamagnetic Iron Oxide Nanoparticles" Seongho Jeon, Derek R. Oberreit, Gary Van Schooneveld, Zhe Gao, John C. Bischof, Christy L. Haynes, & Christopher J. Hogan Jr.;
Ready for Submission to ACS Applied Materials & Interfaces, 2016

Chapter 5
"Quantifying Intra- and Extracellular Aggregation of Iron Oxide Nanoparticles and its Influence on Specific Absorption Rate"
Seongho Jeon, Katie R. Hurley, John C. Bischof, Christy L. Haynes, & Christopher J. Hogan Jr.;
Submitted to Nanoscale 2016

Chapter 6
"Evaluation of Nanoparticle Aggregate Morphology during Wet Milling"
Seongho Jeon, Thaseem Thajudeen, & Christopher J. Hogan Jr.;
Powder Technology, 2015, 272, 75-84

Chapter 2

Nanomaterial Size Distribution Analysis via Liquid Nebulization Coupled with Ion Mobility Spectrometry (LN-IMS)

Summary

We apply liquid nebulization (LN) in series with ion mobility spectrometry (IMS, using a differential mobility analyzer coupled to a condensation particle counter) to measure the size distribution functions (the number concentration per unit log diameter) of gold nanospheres in the 5–30 nm range, 70 nm × 11.7 nm gold nanorods, and albumin proteins originally in aqueous suspensions. In prior studies, IMS measurements have only been carried out for colloidal nanoparticles in this size range using electrosprays for aerosolization, as traditional nebulizers produce supermicrometer droplets which leave residue particles from non-volatile species. Residue particles mask the size distribution of the particles of interest. Uniquely, the LN employed in this study uses both online dilution (with dilution factors of up to 10^4) with ultra-high purity water and a ball-impactor to remove droplets larger than 500 nm in diameter. This combination enables hydrosol-to-aerosol conversion preserving the size and morphology of particles, and also enables higher non-volatile residue tolerance than electrospray based aerosolization. Through LN-IMS measurements we show that the size distribution functions of narrowly distributed but similarly sized particles can be distinguished from one another, which is not possible with Nanoparticle Tracking Analysis in the sub-30 nm size range. Through comparison to electron microscopy measurements, we find that the size distribution functions inferred *via* LN-IMS measurements correspond to the particle sizes coated by surfactants, *i.e.* as they persist in colloidal suspensions. Finally, we show that the gas phase particle concentrations inferred from IMS size distribution functions are functions of only of the liquid phase particle concentration, and are independent of particle size, shape, and chemical composition. Therefore LN-IMS enables characterization of the size, yield, and polydispersity of sub-30 nm particles.

2.1 Introduction

Methods to efficiently determine the size, polydispersity, and concentrations of nanomaterials in liquid suspensions are extremely important in nanomanufacturing systems, particularly for nanomaterials (nanoparticles) in the sub 30 nm size range. Nanoparticles in this size range can exhibit strong size dependent optoelectronic[70, 71] and catalytic [72, 73] properties; extremely accurate and reliable techniques to quantify not only the mean size, but the polydispersity and yield are hence critical in liquid phase synthesis process monitoring. Unfortunately, commonly applied size analysis techniques are limited in capabilities below 30 nm. Aside from electron microscopy (which is time consuming, particularly to infer size and shape distributions with appropriate counting statistics), nanoparticles size distribution functions (the particle number concentration per unit diameter or per unit log diameter, quantifying the size, concentration, and polydispersity) are frequently determined *via* photon correlation spectroscopy/dynamic light scattering [37-40]. Because of the indirect nature of the measurement, it is difficult to apply photon correlation spectroscopy to infer the size distribution functions of highly polydisperse or multimodal samples, and inferred distributions are commonly biased towards larger particles [74]. Further, quantification of nanoparticle concentrations is often not possible. Recently developed Nanoparticle Tracking Analysis (NTA), [43, 48, 75-77], in which the motion of individual particles is monitored and used to infer the size distribution function, does not require the fitting procedures normally associated with photon correlation spectroscopy. However, NTA is difficult to apply to particles appreciably smaller than the wavelengths of visible light, *i.e.* particles smaller than 30 nm are not easily detected. Sub 10 nm particles can often be analyzed by size exclusion

chromatography [78], but particles can clog columns, and the resolution of this technique reduces with increasing size. Finally, flow field fractionation [79] and analytical ultracentriguation[80, 81], can be applied for sub 30 nm particle analysis, though both need to be coupled to appropriate detectors for particles.

Overall, the development of easy-to-apply size distribution measurement procedures remains a critical issue in nanomanufacturing, as synthesis process monitoring must be applied repeatably (*i.e.* to each "batch" of nanomaterials). Further, different size distribution measurement procedures have been found to give results in disagreement with one another in several circumstances [74, 82], with the underlying origins of disagreement still unclear. Additional comparison of the performance of existing techniques amongst one another, as well as comparison to newly developed techniques for a variety of nanomaterials, remains necessary.

In converse to the issues confronted when analyzing nanoparticles in liquids, in aerosols, nanoparticle size distribution analysis is facilitated by ion mobility spectrometry (IMS), specifically using a differential mobility analyzer [83] coupled with a condensation particle counter [53] (DMA-CPC analysis). DMA-CPC measurements require no assumptions regarding the shape or modality of the size distribution function, and when a proper inversion routine is applied [84], this type of analysis facilitates size distribution function determination in the 2–500 nm range. Application of the DMA-CPC technique to liquid suspensions is also possible, provided that the particles of interest can be aerosolized preserving their size distribution function. Along these lines, several studies [62, 85] have examined the use of pneumatic nebulization to spray nanoparticle suspensions and evaporate the solvent, leaving aerosol nanoparticles amenable to IMS. Unfortunately,

traditional nebulizers produce supermicrometer droplets; such droplets typically contain high enough concentrations of non-volatile solute (even with high purity-solvents) such that aerosolization leads to a residue coating on nanoparticles and to the production nanoparticles composed entirely of previously dissolved solute. Residue coating can shift the sizes of sub-30 nm particles by several to tens of nanometers, and the size distribution function of residue nanoparticles can mask entirely the particles of interest [86]. This limits analysis to >50 nm particles in most circumstances. Additionally, multiple nanoparticles can be present within the same droplet, and these nanoparticles will agglomerate with one another upon solvent drying. As an alternative to pneumatic nebulization, Fernandez de la Mora and coworkers [87], Kaufman and coworkers,[86, 88, 89] Lenggoro and coworkers,[90-92] and more recently Tsai, Zachariah & coworkers[93-100] have examined the use of electrosprays followed by charge reduction[101, 102] to produce submicrometer (down to 100 nm) droplets. Electrosprays facilitate the aerosolization of aqueous particles with minimal shifts in the size distribution function. Though this technique has been successfully applied to metal nanoparticles [91, 97, 103], polymers [104-106], proteins[88, 89, 107], as well as viruses and virus-like particles [108-115], there are still drawbacks to using electrosprays for aerosolization; namely, (1) there are rather strict requirements on the electrical conductivities of suspensions which can be electrosprayed [116, 117], and (2) non-volatile solutes need to be removed from the suspension prior to electrospray based aerosolization (*i.e.* electrospray based aerosolization still leads to the formation of residue particles from solutes) [86]. These requirements have limited the application electrospray-DMA based analyses to highly purified protein and virus samples. In total, because of the lack of robust aerosolization techniques, though fast

and relatively inexpensive, IMS approaches have not been widely adopted for nanoparticle size distribution analysis in liquids.

In the interest of improving the utility of IMS in nanoparticle analysis, here we apply a recently developed liquid nebulizer (LN) to aerosolize nanoparticles, and subsequently show that their size distributions can be analyzed *via* IMS, *i.e.*with a DMA-CPC combination. Unique from most pneumatic nebulizers, the LN applied in this work utilizes online dilution with ultrapure water (UPW) with dilution factors (UPW flowrate/sample flow rate) in excess of 10^2, and an inertial impactor to remove large droplets prior to analysis. The dilution-impaction combination leads to minimal perturbation of the particle size distribution during aerosolization. Using the LN, we made IMS measurements of sub 30 nm gold nanospheres (down to 5 nm in nominal diameter), gold nanorods, and albumin proteins in aqueous suspensions with variable pH and concentration of phosphate buffered saline. Importantly, we show that independent of particle size, shape, and solute concentration, a calibration curve can be developed linking measured aerosol concentrations to the nanoparticle concentrations in suspension. Results are compared to electron microscopy and NTA. To our knowledge, this is the first demonstration of quantitative, IMS-based size distribution function measurement of sub-20 nm nanomaterials in which nanomaterials were aerosolized without the use of electrospray.

2.2 Materials and methods

2.2.1 Nanoparticle suspensions

Gold nanospheres of five nominal diameters (5, 7, 10, 15, and 30 nm, which had manufacturer reported mean diameter ± standard deviations of 5.06 ± 0.77 nm, 7.20 ± 0.82 nm, 12.05 ± 0.99 nm, 17.06 ± 1.70 nm, 30.02 ± 3.86 nm, respectively) as well as 980 nm resonant gold nanorods (GNRs, which were nominally 70.5 nm in length × 11.7 nm in diameter) were all purchased from Nanocomposix, Inc. (San Diego, CA, USA). To stabilize suspensions, gold nanospheres were pretreated with tannic acid and the surface of gold nanorods was coated with citrate anions (subsequent to synthesis). Bovine serum albumin (BSA, CAS registration #: 9048-46-8) and ovalbumin (OVA, albumin from chicken egg white, CAS registration #: 9006-59-1) were also examined and were purchased from Sigma Aldrich (Saint Louis, MO, USA). Suspensions were prepared with a variety of solutes and with number concentrations in the 2.00×10^{9} mL^{-1} to 8.16×10^{14} mL^{-1} range. First, gold nanosphere suspensions were either used directly (with tannic acid included) in experiments or diluted offline (to vary concentrations) with UPW, which had total organic carbon and non-volatile residue levels below 1 ppbv, was treated with 165 nm UV-light and was passed 10 nm & 20 nm particle filtration systems as well as a mixed bed ion exchange resin. The pH of suspensions was controlled to be 5.0–9.7 by adding either acetic acid (BDH Aristar) or ammonium hydroxide (Macron Fine Chemicals). Second, gold nanospheres were diluted (to varying concentration levels) in 0.001×–0.01× phosphate buffered saline (PBS, Corning Life Science, CA, USA). At this PBS concentration level, gold nanospheres were found stable in suspension for more than seven days (by visual examination). GNR suspensions were found to contain significantly

higher concentrations of non-volatile solutes, hence prior to measurement GNR suspensions were diluted one-hundred fold in de-ionized (DI) water (produced using a SpectraPure, Tempe, USA filtration system, and not filtered to the extent of the UPW), centrifuged twice (7600 rpm for 15 minutes with a model 5418 centrifuge, Eppendorf, Hamburg, Germany), and finally resuspended in DI water. We note that this preparation procedure is considerably simpler than that used in preparing GNRs for electrospray based aerosolization previously [118, 119]. BSA and OVA samples were prepared by dissolving known weights (from which number concentrations were determined) in UPW, with the suspension pH similarly varied by addition of acetic acid and ammonium hydroxide. BSA and OVA samples were also prepared in 0.01× and 0.05× PBS.

2.2.2 Liquid nebulizer - ion mobility spectrometry (LN-IMS) Measurements

A schematic diagram of the LN is provided in Figure 2.1, and a schematic diagram of the LN coupled with a DMA and CPC for IMS measurements is shown in Figure 2.2. The LN (LiquiTrak® Model 7788, Fluid Measurement Technologies, Inc., St Paul, MN, USA), similar to the model employed by Fissan et al [62], was designed to have (1) a small air-liquid mixing chamber to maximize the breakup of liquid into droplets, (2) a small existing orifice diameter, generating back pressure on the sample flow and further promoting droplet formation, and (3) a ball-type inertial impactor at the exit of the nebulizer to efficiently remove larger droplets from the generated aerosol. The generated droplet size distribution function has been measured by the residue method [117], and is reported on in the results and discuss section. Briefly, the droplet size distribution function is found to be approximately lognormal, with a geometric mean diameter of 99.8 nm and a

geometric standard deviation of 2.32. For LN operation, a colloidal suspension is pumped at a flow rate in the 0.01 to 1.0 milliliter per minute (mL min^{-1}) range; this flow is mixed with UPW flowing at 100 ml min^{-1}, with combined outlet inline with the UPW inlet, and the sample flow inlet oriented perpendicular to the UPW inlet and combined outlet. The ratio of these two flow rates defines a dilution factor (DF) for the sample, which can be varied from 10^2 to 10^4. After mixing, ~98 mL min^{-1} of the flow is diverted to a waste stream, while 2 mL min^{-1} is directed into a single nozzle, where it is mixed with 0.6 standard L min^{-1} of air at 19 ^{o} C (monitored continuously during measurement). Upon exiting the nebulizer, an evaporator (at 57-60^{o} C) facilitates solvent volatilization, leaving a flowing aerosol composed of particles and non-volatile solutes originally in the liquid sample.

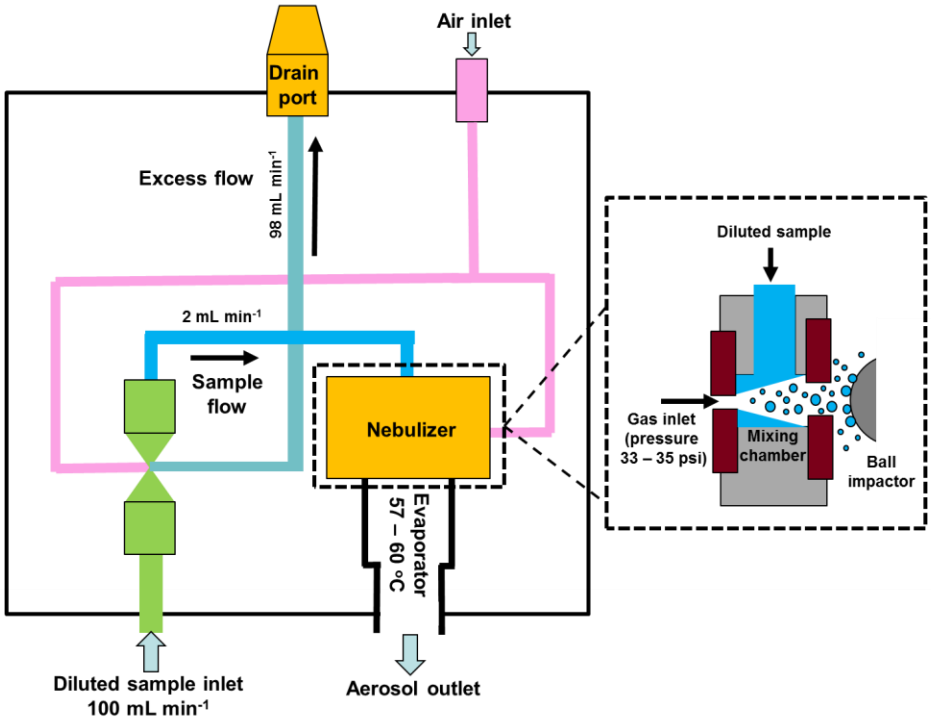

Figure 2.1. Schematic diagram of the liquid nebulizer (LN)

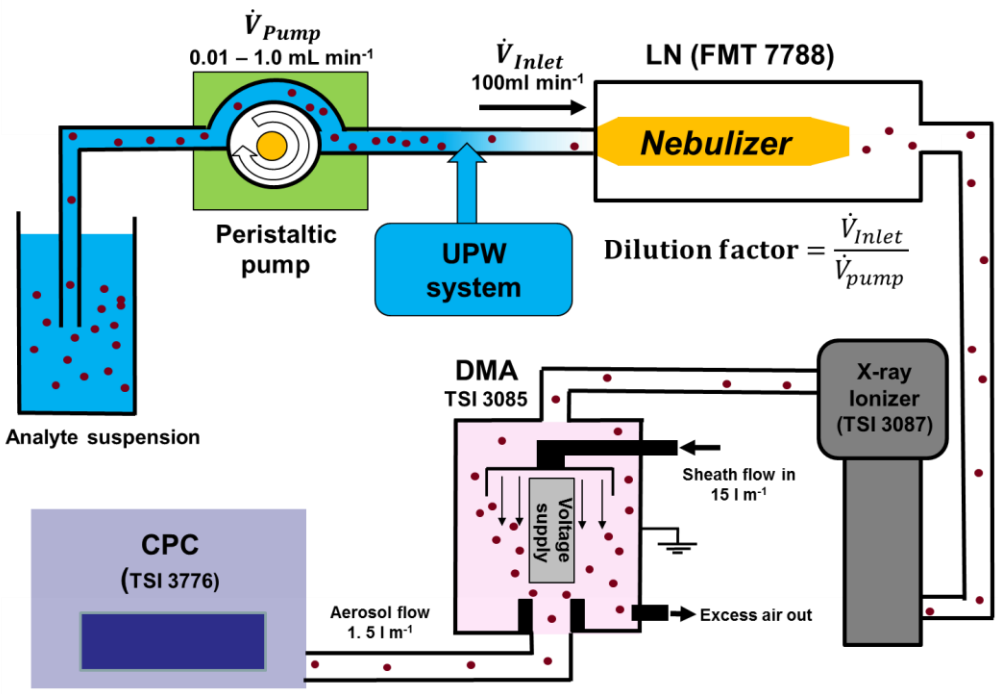

Figure 2.2. Schematic diagram of the LN coupled with a differential mobility analyzer (DMA) and condensation particle counter (CPC) for IMS measurements

For IMS measurements, 1.5 l min^{-1} of the nebulized particle flow is introduced into a soft X-ray ionization chamber (Advanced Aerosol Neutralizer 3087, TSI Inc., Shoreview, MN, USA) [120]. Soft X-ray irradiation generates roughly equal concentrations of positive and negative ions from trace organic molecules (at part-per-trillion levels) in air (photoionization) [121, 122]; these ions subsequently collide with particles and transfer charge to them upon collision. After remaining in the ionization chamber for a sufficient amount of time, the particles achieve known size-dependent charge distribution function, wherein most particles are neutral and the majority of charged particles are singly charged [123, 124]. Particles are then directed into a DMA (model 3085, TSI Inc.) [52]; DMAs act as narrow band mobility filters, only transmitting particles in a mobility range governed by their sheath flowrate (15 l min^{-1}) and the applied potential difference between electrodes.

Particles transmitted through the DMA are detected by a CPC (model 3776, TSI Inc.). The DMA and CPC are operated in tandem as a scanning mobility particle spectrometer (SMPS) [125] with 120 second upward voltage scans applied, 15 second downscans, and ~60 seconds between scans.

The LN-IMS measurements reported here were performed as follows. First, the gold nanospheres, GNRs, and the two proteins were nebulized separately and examined at variable analyte concentrations and dilution ratios, as well as variable PBS concentration and pH. Subsequently, six mixtures, each composed of two different sized sub-30 nm gold nanospheres were measured. Tables listing each sample analyzed, its initial number concentration, pH, PBS concentration, and online dilution factor is provided in Tables 2.1 and 2.2.

2.2.3 Nanosight™ and transmission electron microscope

LN-IMS measurements were compared to NTA measurements made with a Nanosight™ LM-14 (Malvern Instruments LTD, Malvern, Worcestershire, UK), as well as transmission electron microscopy (TEM, FEI, Hillsboro, OR, USA) measurements. With NTA, we examined the size distributions of both monodisperse (10, 15, 30, and 60 nm in diameter) and polydisperse (15 & 30 nm, and 30 & 60 nm, mixtures) gold nanospheres. Because the recommended particle concentration for NTA measurements is $<10^9$ particles per mL, the original gold nanosuspensions were diluted with DI water (SpectraPure, Tempe, USA) by a factor of 10^2–10^3. At least 5 measurements were performed for each sample and the hydrodynamic size distribution function was inferred

using the procedure described by Jeon *et al.*[126], in lieu of using the Nanosight™ software program.

Table 2.1. The LN-IMS experiment conditions for 5, 7 and 10 nm gold nanospheres.

Material	Suspension Properties	particle # concentration (# mL^{-1})	Dilution factor
5 nm gold nanosphere	DI Water	4.80×10^{13}	2000
			5000
		8.00×10^{12} (mixture)	500, 1000
		4.80×10^{12}	500, 1000, 2000
		4.80×10^{11}	500
		4.80×10^{10}	200
7 nm gold nanosphere	DI Water	1.70×10^{13}	1000
			2000
		2.83×10^{12} (mixture)	500
		2.83×10^{12} (mixture)	250, 500
		2.83×10^{12} (mixture)	250
		8.50×10^{12}	2000
		1.70×10^{12}	500, 1000
		8.50×10^{11}	500, 1000
		1.70×10^{11}	500, 1000
		8.50×10^{11}	200
		8.50×10^{9}	125
10 nm gold nanosphere	DI Water	3.40×10^{12}	2000
			1000
		2.83×10^{12} (mixture)	500
			1000
		2.83×10^{12} (mixture)	500
		3.40×10^{11}	1000
		3.40×10^{10}	200
			500
		3.40×10^{9}	125
	pH 6.0	3.04×10^{12}	2000
	pH 9.7	3.04×10^{11}	500
	PBS 0.01	3.04×10^{12}	2000
	PBS 0.005	3.04×10^{12}	1000

Table 2.2. The LN-IMS experiment conditions of 15 and 30 nm gold nanospheres, GNRs, BSA and OVA.

Materials	Suspension Properties	particle # concentration (# mL^{-1})	Dilution factor
15 nm gold nanosphere	DI Water	1.10×10^{12}	1000
		9.17×10^{11} (mixture)	250, 500
		1.83×10^{11} (mixture)	250, 500
		1.10×10^{11}	500
		1.10×10^{10}	125
	pH 6.0	1.00×10^{12}	2000
	pH 9.7	1.10×10^{11}	500
	PBS 0.005	9.90×10^{11}	1000
30 nm gold nanosphere	DI Water	2.00×10^{12}	125
			200
		1.67×10^{11} (mixture)	250, 500
		1.67×10^{11} (mixture)	250
		1.67×10^{11} (mixture)	250
			500
		2.00×10^{10}	200
			500
		2.00×10^{9}	125
Gold nanorod	DI Water	7.45×10^{10}	125
			200
BSA	DI Water	4.53×10^{14}	10000
		2.26×10^{14}	10000
		4.53×10^{13}	2500
		1.13×10^{14}	5000
		8.48×10^{13}	2500
			5000
		5.65×10^{13}	2500
		2.26×10^{13}	2000
		2.26×10^{12}	1000
		2.26×10^{11}	250
		2.26×10^{10}	125
	PBS 0.01	2.00×10^{14}	10000
	PBS 0.05	4.04×10^{14}	10000
	pH 5.0	2.26×10^{14}	10000
	pH 9.7	2.26×10^{14}	10000
OVA	DI Water	6.12×10^{14}	10000
		6.12×10^{13}	1000, 2000, 2500
	PBS 0.01	5.54×10^{14}	10000
	pH 9.7	8.16×10^{14}	10000

For TEM measurements, an FEI Tecnai T12 TEM (in the University of Minnesota Characterization Facility) was used to image the gold nanospheres and the GNRs. 10–30 μl of each analyte suspension were dropped onto a carbon grid (200 mesh, Ted Pella INC, CA, USA) and the solvent was allowed to evaporate. The software 'ImageJ' was employed to measure particle sizes in TEM images. More than 300 individual particles were examined for each sample to establish an accurate particle size distribution. The TEM was calibrated monthly and measurements are expected to be accurate to within 0.1 nm. For the GNRs, the measurement of the width and length of each rod enabled the inference of its hydrodynamic radius (R_H) and projected area (PA), which enabled direct comparison to LN-IMS measurements [118].

2.3 Results & discussion

2.3.1 Size distribution functions

Size distribution function measurements involve inversion of the function $\frac{dn}{dlog_{10}(d_p)}$, the number concentration per unit $\log_{10}$ of particle diameter (d_p). In LN-IMS mesaurements, this distribution is determined not in the liquid phase, but the gas phase, via measurement of particle number concentrations (n_i) with a DMA operated under voltage settings "i". n_i and $\frac{dn}{dlog_{10}(d_p)}$ are linked via the equation:

$$n_i = \sum_{z=+1}^{z=+\infty} \int_{-\infty}^{\infty} \eta_{CPC}(d_p)\theta_i(d_p,z)\eta_D(d_p)f_z(d_p,z)\frac{dn}{dlog_{10}(d_p)}dlog_{10}(d_p) \qquad (2.1)$$

where $\eta_{CPC}(d_p)$ is size dependent detection efficiency of the CPC, $\theta_i(d_p, z)$ is the DMA tansfer function under settings "*i*" (with settings corresponding to sheath flowrate, aerosol inlet and outlet flowrates, and applied voltage), $\eta_D(d_p)$ is the size dependent fraction of particles transmitted through the DMA-CPC system (i.e. those that did not diffusionally deposit), and $f_z(d_p,z)$ is the fraction of particles of integer charge state *z* exiting the soft X-ray photoionizer. To determine $\frac{dn}{dlog_{10}(d_p)}$, measurements must be at a sufficient number of settings "i", an inversion routine must be applied to solve equation (2.1), and all functions except n_i (the observable) and $\frac{dn}{dlog_{10}(d_p)}$ must be known *a priori*. We applied the built-in SMPS software and DMA transfer function available with TSI instruments for inversion (Aerosol Instrument Manager), in which the CPC detection efficiency in the size range of interest was unity, the Stokes-Millikan equation[127, 128] was used to link the mobility to the particle diameter, transmission efficiencies were calcuated using the Gormely-Kennedy equations [129], and $f_z(d_p, z)$ was calculated via the regression equations of Wiedensohler [124] (which recent studies suggest are reasonably valid for spheres and nanorods [123, 130]). None of these functions are strongly dependent on the chemical nature of the particles examined. We thus postulate that when plotted against the analyte suspension concentration, the dilution corrected number concentration of particles (n_{tot}), described by the equation:

$$n_{tot} = DF \int_{-\infty}^{\infty} \frac{dn}{dlog_{10}(d_p)} dlog_{10}(d_p) \quad (2.2)$$

should collapse to an analyte (size, shape, and chemical composition) and solute independent function. In the remaining sub-sections, we (1) report the inverted size distribution functions from LN-IMS for all samples, (2) examine (numerically) the LN conditions required to preserve size distribution functions during aerosolization, (3) compare LN-IMS measurements to NTA and TEM analysis, and (4) demonstrate that the dilution factor corrected aerosol number concentration is in fact solely dependent on the original suspension number concentration.

2.3.2 Droplet size distribution functions

Most pneumatic nebulizers create droplet size distribution functions which have mode diameters between 2 and 5 μm; such droplets are not well suited for aerosolization of nanoparticles without distortion of the particle size distribution function. To measure the droplet diameter, we applied the residue method [117], in which we mixed sucrose with UPW at an original sucrose volume fraction (V_f) of 0.0654. This high concentration solution was then nebulized with DFs of 17.39 and 42.11, and after solvent evaporation, the size distribution functions of the residual sucrose particles were measured with the DMA-CPC. Droplet diameters (d_D) were linked to the measured sucrose particle diameters (d_S) through the relationship: $d_D = (\frac{DF}{V_f})^{1/3} d_S$. Inferred droplet size distribution functions are plotted in Figure 2.3. The good agreement between measurements with different DFs suggests that solutions are well mixed after dilution and prior to nebulization, and further suggests that the residue method enabled reliable estimation of the droplet size distribution function. The droplet size distribution function is found to be approximately lognormal, with a geometric mean diameter of 99.8 nm and a geometric standard deviation of 2.32.

This geometric mean diameter is similar to many charge reduction electrospray sources [86]; however, the geometric standard deviation is much larger than cone-jet mode electrosprays (which are typically closer to 1.1)[117]. Nonetheless, more than 95% of the droplets generated and exiting the nebulizer (i.e. transmitted around the impactor) are smaller in diameter than 350 nm, suggesting that the LN examined here will minimally distort nanoparticle size distributions during aerosolization.

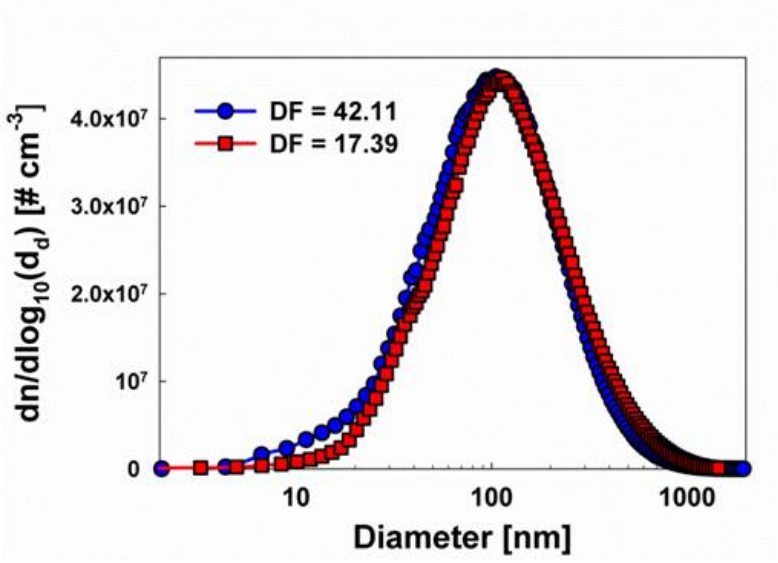

Figure 2.3. LN generated droplet size distribution functions, inferred using the residue method.

2.3.3 LN-IMS size sistribution functions

The size distribution functions (averaged over 10 consecutive scans) of 5, 7, 10, 15 and 30 nm diameter gold nanospheres and GNRs, nebulized at a pH near 7, are shown in Figure 2.4. Best fit lognormal distribution functions are also displayed on these plots, with the geometric mean diameter (d_{pg}) and geometric standard deviation (σ_g) are also noted on the figure. For all examined particles, σ_g values were below 1.2, indicating that narrowly distributed particles were detected. Similar plots for BSA and OVA are shown in Figure

2.5, where we obtained mode diameters of 6.4 nm and 5.7 nm, respectively. These protein effective diameters are in good agreement with higher resolution IMS measurements of low charge state BSA and OVA collision cross sections [131-133]. We additionally found the geometric mean diameter and standard deviation to be independent of DF, provided that DF was sufficiently high to reduce the sizes of residue particles well below the sizes of the particles and to mitigate droplet induced aggregation. While in total these results suggest that LN-IMS measurements enable accurate size distribution function inference, for the gold nanospheres, all d_{pg} values were slightly larger than the nominal diameters and manufacturer reported mean diameters for several samples; we remark further on this observation in comparison to TEM measurements in section 2.3.5.

The non-volatile residue present in the samples examined in Figure 2.4 derives from surfactants used in stabilizing nanoparticles in suspension as well as salts used during particle synthesis. Of interest is also examination influence additional solutes may have on LN-IMS measurements, as well as changes in pH. Figure 2.6 displays the size distribution functions of 10 nm and 15 nm gold nanospheres from DI water (with non-volatile residue remaining from their original suspension), 0.005X PBS, and in pH 9.7 suspensions. The initial suspension concentration and dilution factor are labelled for each measurement. Similar results were obtained for gold nanospheres of other sizes, and both protein samples. Figure 2.7 shows the size distribution functions of BSA and OVA proteins in DI water, pH 4.7, and PBS 0.01X suspensions. Evident by comparison of the Figures 2.6 and 2.7 plots to one another is that the peak diameter of the distribution functions corresponding to gold nanospheres and proteins do not shift from DI water to PBS or pH suspensions. Further,

we did not observe any changes to size distribution functions over time, suggesting that gold nanoparticles and proteins did not aggregate in any of the test suspensions.

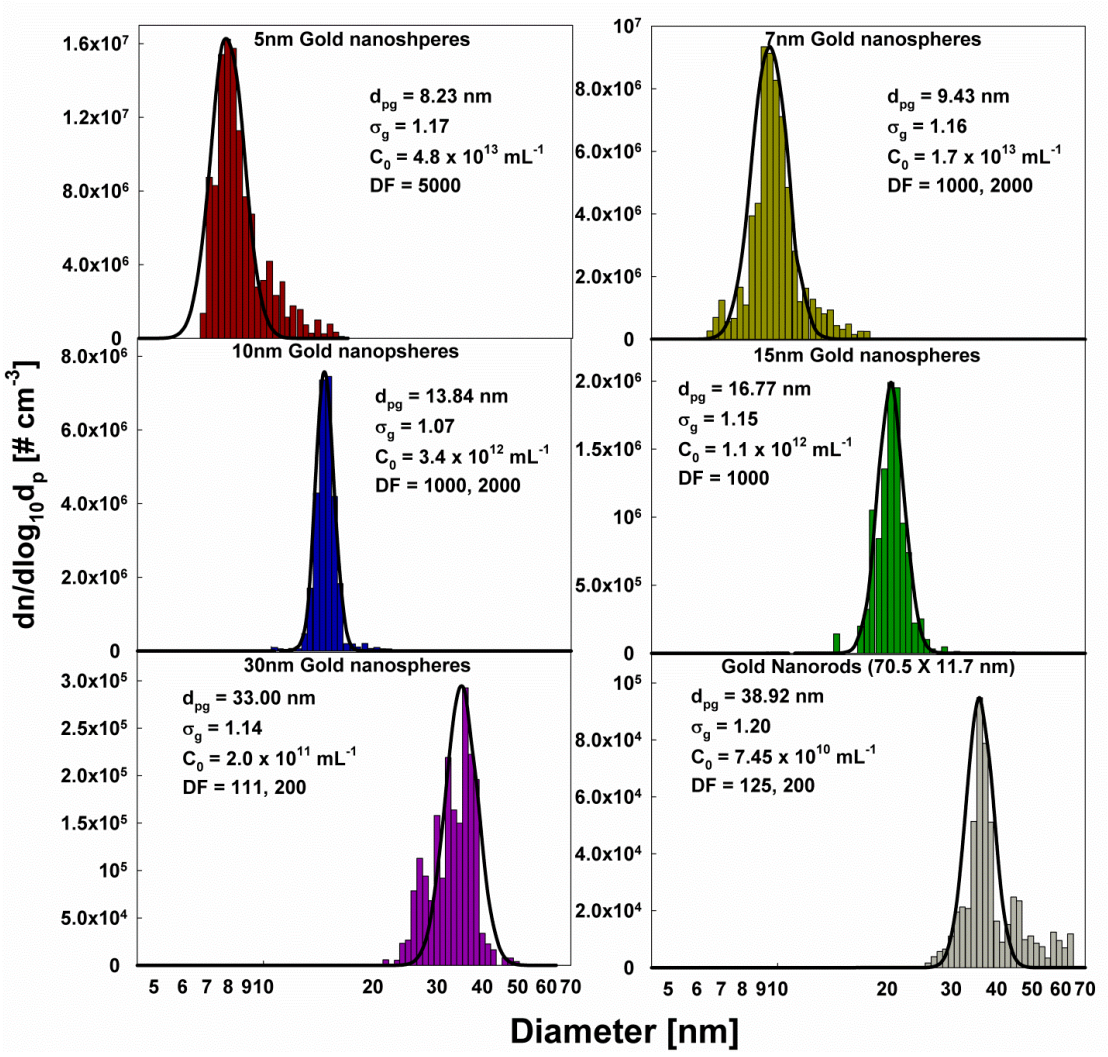

Figure 2.4. LN-IMS inferred size distribution functions for gold nanospheres and GNRs.

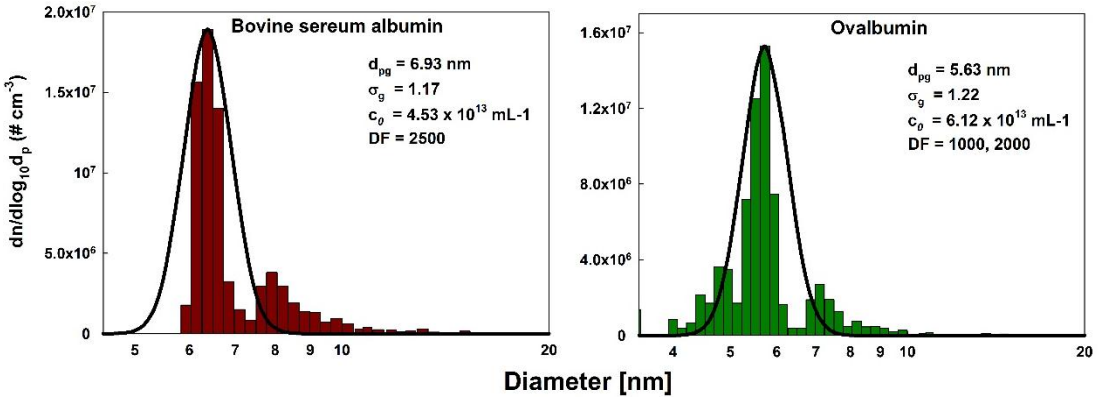

Figure 2.5. LN-IMS inferred size distribution functions for bovine serum albumins (BSA) and ovalbumins (OVA) dispersed in DI water.

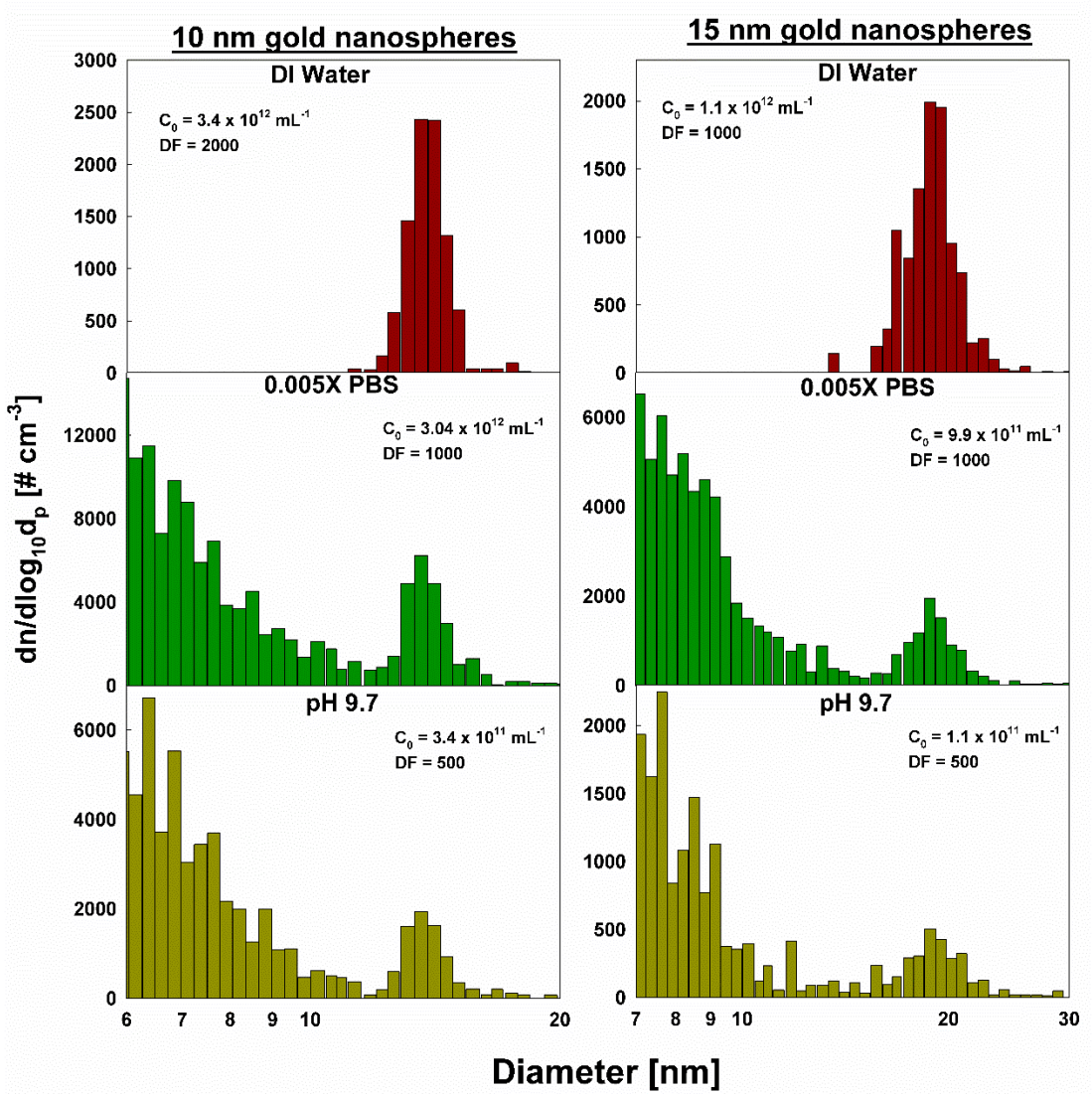

Figure 2.6. LN-IMS inferred size distribution functions for nominal 10 nm and 15 nm gold nanospheres in DI water (upper), 0.005 X PBS (middle), and a pH 9.7 suspension.

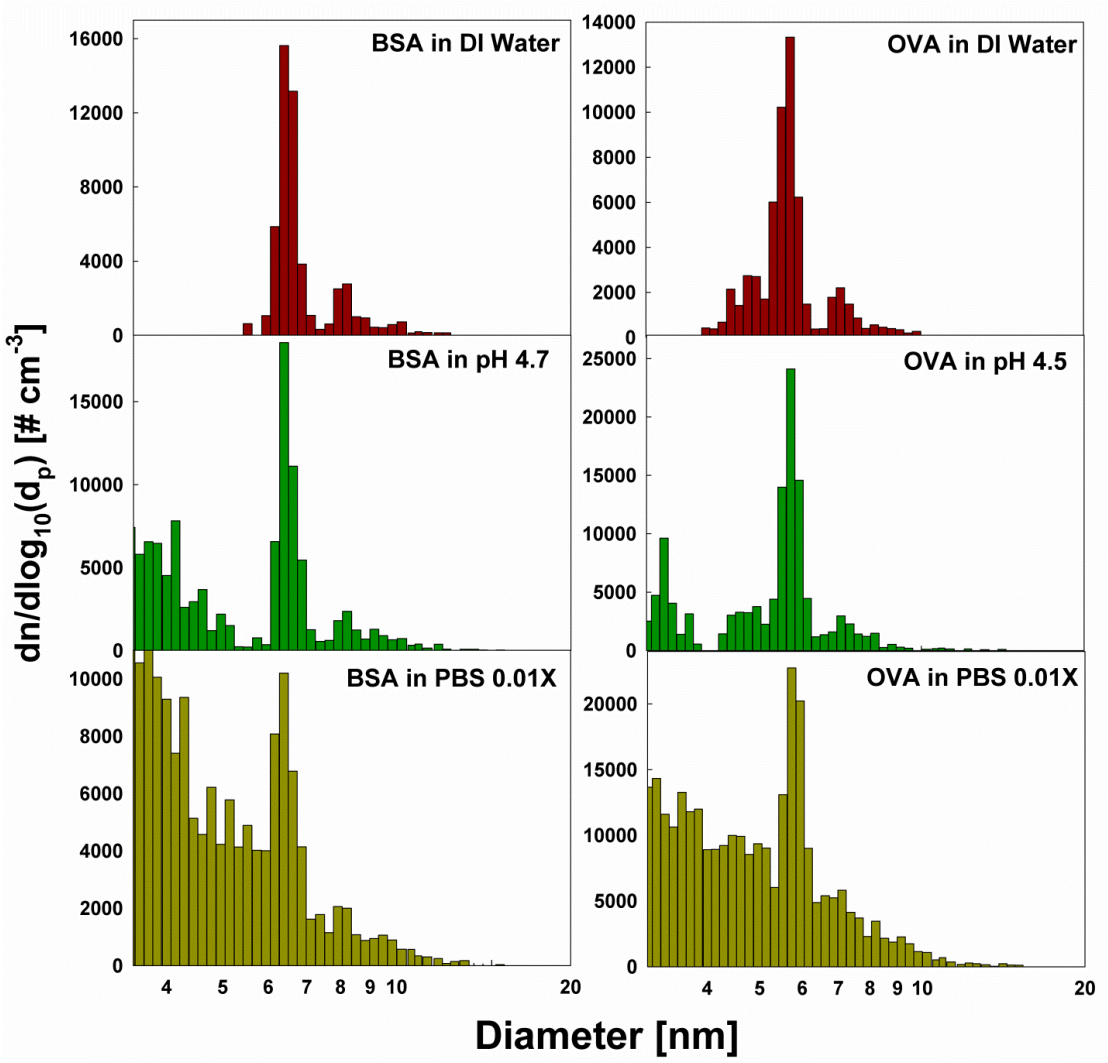

Figure 2.7. Size distribution functions of bovine serum albumin (BSA) and ovalbumin (OVA) in various suspensions. As with gold nanospheres, peaks below 5 nm in diameter correspond to non-volatile residue formed during the aerosolization process.

However, also visible in distribution functions are residue particles at separate, smaller diameter, modes in both the PBS and pH solution size distribution functions; such peaks arise because (1) these suspensions were of lower concentration than the original and lower dilution factors were used, and (2) the concentrations of non-volatile solutes were higher in these suspensions. Nonetheless, these results show that it is possible to identify and measure the size distribution functions of sub 30 nm particles via LN-IMS in

suspensions with non-volatile residue present (which is not possible with electrospray based ionization[86]).

The size distribution functions of six gold nanosphere mixtures (7 & 15 nm, 5 & 10 nm, 15 & 30 nm, 7 & 10 nm, 7 & 30 nm and 10 & 30 nm in diameter) were also examined and are plotted in Figure 2.8. The concentration ratios in suspension as well as the dilution factors utilized in measurements are noted. In all instances, we were able to clearly identify both particle types in mixtures. These results are compared to NTA measurements in section 2.3.5.

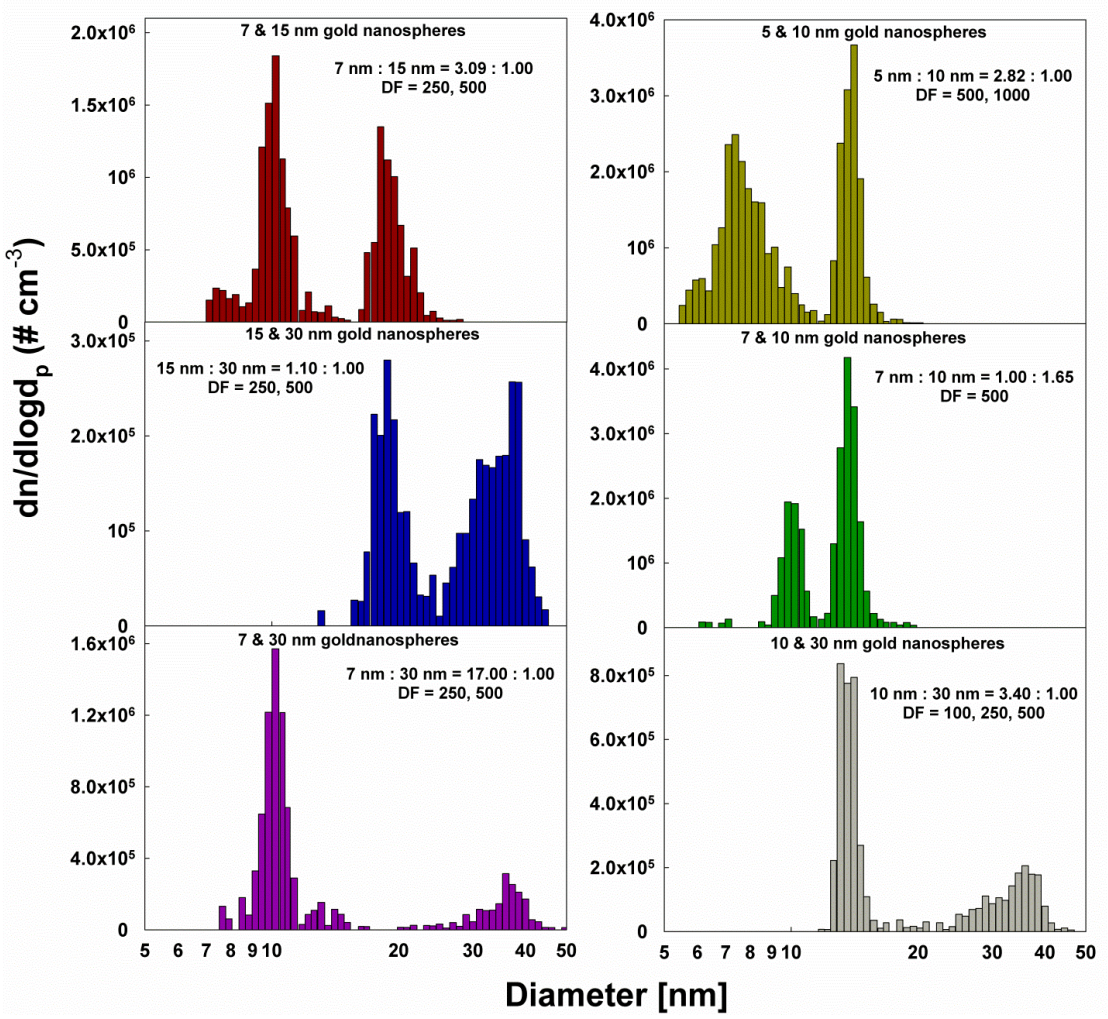

Figure 2.8. LN-IMS inferred size distribution functions for gold nanosphere mixtures.

2.3.4 Simulation of hydrosol to aerosol conversion

The results presented in the previous section demonstrate that the LN-IMS approach is applicable to size distribution function analysis of sub 30 nm particles when appropriate dilution factors are employed. However, it does not make clear how to select such dilution factors. In this section, we present a simulation method, based upon prior simulation efforts [134-137] to predict the LN-IMS inferred size distribution function. In simulations, first, we sample a droplet diameter from an input droplet size distribution function. Second, we compute the average number of analyte particles in the droplet based upon the suspension concentration and dilution factor, and use this average to sample the number of analyte particles in the droplet from a Poisson distribution. Third, the diameters for each particle in the droplet are sampled from an input particle size distribution function. Finally, the solid volume and solid diameter (after solvent evaporation) are determined based upon the total analyte particle volume present in the droplet as well as the volume of non-volatile residue (which is also an input). This sampling procedure is repeated for 10^6 droplets and a hypothetical size distribution function is then reconstructed for a given input particle size distribution function, non-volatile solute volume fraction, dilution factor, and droplet size distribution function. When an appropriate droplet size distribution function (determined by the nebulizer operating conditions) and dilution factor are chosen, the size distribution function recovered from the simulation should be faithful to the input function. As a case study, we examine the aerosolization of nominally 15 nm gold nanospheres as well as a mixture of nominally 15 & 30 nm gold nanospheres, with the normalized size distribution functions (based on TEM measurements) shown in Figures 2.9 (a.) and 2.9 (b.), respectively. We assumed a suspension concentration $C_0 = 10^{14}$ mL^{-1} for the 15 nm

spheres and C_0 = 2 x 10^{14} mL^{-1} for the mixture, respectively. A non-volatile solute concentration of 13.7 mM NaCl (equivalent to 0.1X PBS) was also assumed.

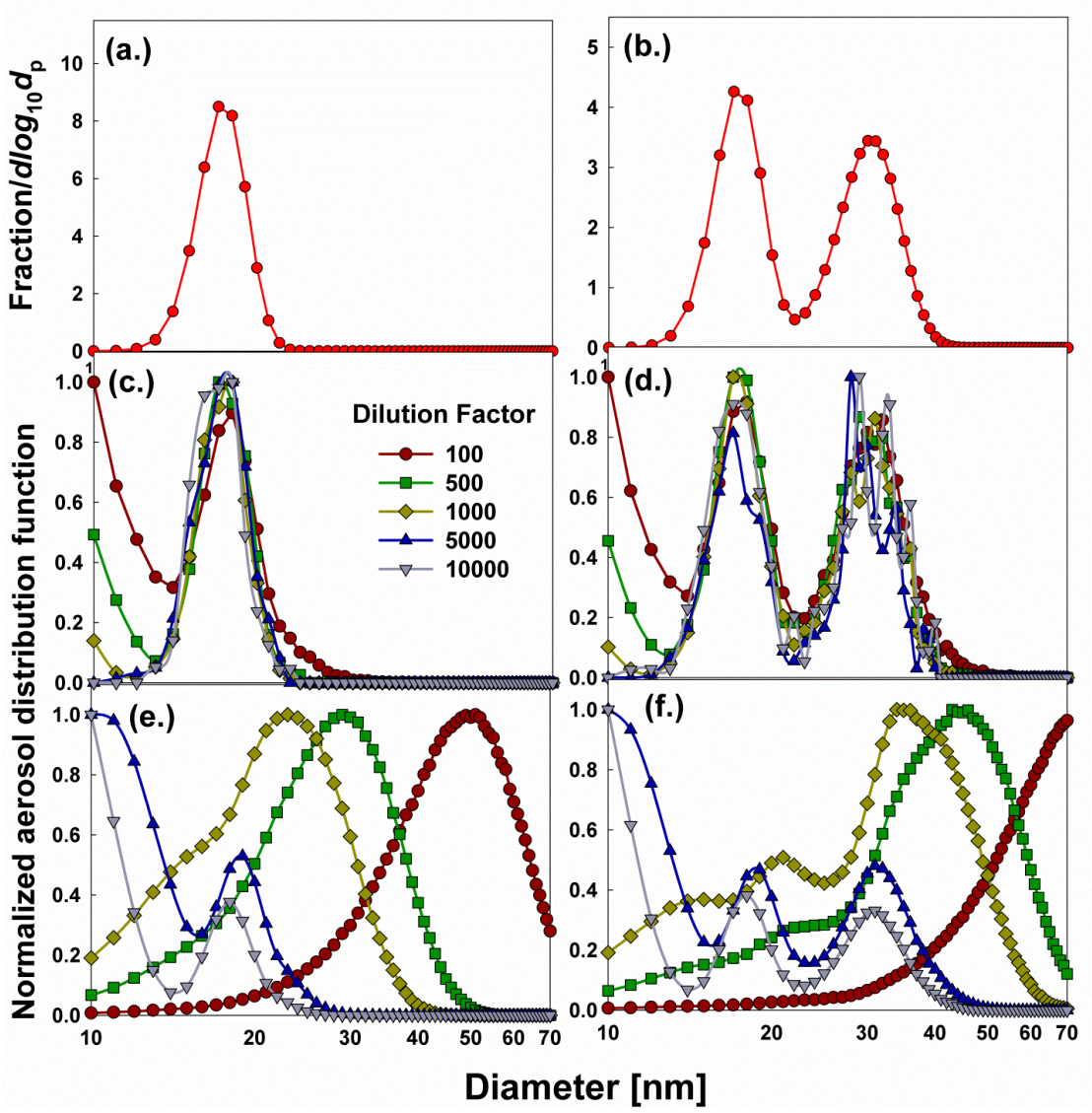

Figure 2.9. The input size distribution function for **(a.)** nominal 15 nm gold nanospheres and **(b.)** a mixture of nominal 15 nm and 30 nm gold nanospheres. The expected LN-IMS size distribution functions (normalized by the maximum value in the 10-70 nm range) corresponding to **(a.)** and **(b.)** are shown in **(c.)** and **(d.)**, respectively. The expected IMS size distributions with Gaussian distributed droplets (mean 2.5 μm, standard deviation 0.7 μm) are shown in **(e.)** and **(f.)**.

With the droplet size distribution function modeled as a Gaussian distribution with a mean of 184 nm and standard deviation 140 nm, the expected LN-IMS size distribution functions (normalized by the maximum value in all cases) are shown for varying dilution factors in Figure 2.9 (c.) and 2.9 (d.), respectively. At low dilution factors, for both cases a small residue peak is present (below 10 nm), and the peaks corresponding to gold nanospheres are distorted by both the formation of dimers and the presence of non-volatile residue. However, increases in the dilution factor shift the residue peak to smaller sizes and further reduces the impact of residue and aggregation on the gold nanosphere peaks; under these conditions we expect LN-IMS measurement to enable accurate inference of the colloid particle size distribution function. For comparison, in Figures 2.9 (e.) and (f.) we plot the expected size distribution functions from a nebulizer producing Gaussian distributed droplets with a mean diameter of 2.5 μm and a standard deviation of 0.7 μm (expected for traditional nebulizers). Under all conditions but DF = 10^4, the expected size distribution function does not have a peak or peaks corresponding to gold nanospheres, and with DF = 10^4, the size distribution function is still distorted by residue. This highlights clearly the need to use a nebulization scheme with small droplets to mimimize the volume of non-volatile residue per droplet.

2.3.5 Comparison to NTA and TEM analysis

To compare LN-IMS results to NTA measurements, we elected to examine three monodisperse samples and one mixture sample. NTA results are summarized in Figure 2.10, with the 15 nm and 30 nm gold nanosphere mixture with the same concentration ratio as the mixture in Figure 2.8. A number of issues arise when using NTA; first, the 10 nm

gold nanospheres are not detected efficiently, and the mode in the distribution function appears at 30 nm. Second, though 15 nm and 30 nm particles have mode diameters near their expected values, the distributions are noticeably polydisperse, in contrast with narrow distributions inferred from LN-IMS measurements.

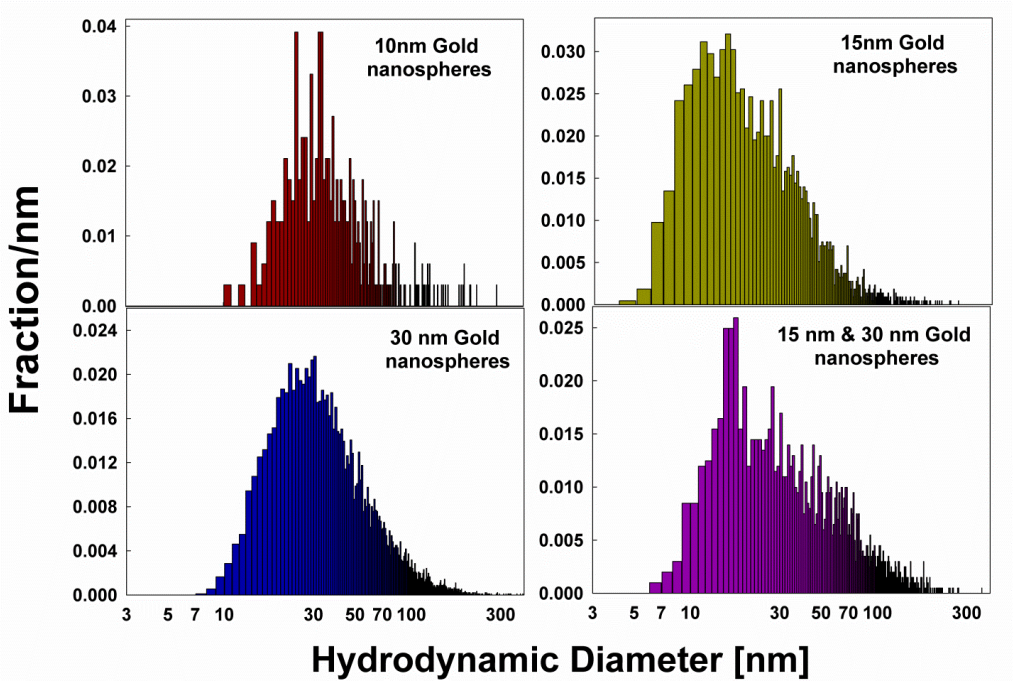

Figure 2.10. A summary of the normalized size distribution functions resulting from NTA of gold nanosphere suspensions.

Confirmation of the accuracy of LN-IMS measurements in determining polydispersity, as compared to NTA, is provided in Figure 2.11, which displays plots of the size distribution functions for gold nanospheres and GNRs based upon TEM analysis. Size distribution functions were reconstructed by binning results and are directly comparable to Figure 2.3. For the GNRs, we used the equations tested by Gopalakrishnan et al [118] to estimate the GNR mobility diameter (as inferred from DMA measurements) from their lengths and diameters. The geometric standard deviations inferred from LN-

IMS are in good agreement with those inferred from TEM measurements; with the exception of the GNRs, the geometric standard deviations differ by 0.06 or less between the two meaurements. Overall, this comparison suggests that size distribution functions inferred from NTA in the sub-30 nm size range are not necessarily accurate, with overestimation of the geometric standard and width of the distribution likely. Corroboration of this result is found in the recent work of Dudkiewicz et al,[82] who examined the size distribution functions of silica nanoparticles below 250 nm by IMS (with electrospray based aerosolization), NTA, electron microscopy, centrifugal liquid sedimentation, and assymetric flow field fractionation, and found that NTA inferred size distributions had both larger means and higher polydispersities than the distributions inferred from other techniques, including IMS.

Mobility diameters, inferred by DMAs, are typically ~0.3 nm larger than the physical diameter of spherical particles, due to influence of gas molecule size on drag in the gas phase [127]. However, there are differences larger than this amount in the geometric mean diameter inferred from LN-IMS and TEM measurements in this work. For gold nanospheres, we find that the TEM geometric mean diameters are always within 0.5 nm of the nominal diameter, while the LN-IMS geometric mean diameters are 3-4 nanometers larger than the nominal diameter. A disparity of ~8 nm in effective diameter is seen for the GNRs between the two measurments. There are two possibilities for this difference which must be considered. First, the mobility diameter is inferred from the mobility based on the assumed validity of the Stokes-Millikan equation. This equation is verified primarily through measurement of organic ions [138, 139] and there is some evidence that minor deviations arise for metal particles in air [140]. However, these deviations would lead to

only an increase in the inferred diameter of several percent, and cannot explain the differences in inferred diameters here. We find a second possibility more plausible; differences in geometric mean diameters arise because of an organic surfactant coating on particles (tannic acid for gold nanospheres and sodium citrate for GNRs, both of which are present on particles in suspension, serving to stabilize them against aggregation). These surfactants are sufficiently volatile to evaporate during TEM measurement (during pump down or in the electron beam) but would persist in the gas phase, increasing particle diameter. Support for this result is found in Hinterwirth et al [74], who found that for gold nanospheres in the 10 – 30 nm size range introduced into the gas phase via electrospray, the mean IMS-inferred diameters were 3-4 nm larger than those inferred from TEM. Additionally, in several prior electrospray based aerosolization studies, it was necessary to apply heating to remove surfactant coating from metal nanoparticles and without heat treatment nanoparticle size distribution functions were shifted to larger sizes by an excess of ten nanometers [91, 118]. We therefore suggest that LN-IMS enables measurement of the diameters of nanoparticles including any coating bound in suspension, hence it provides information in addition to, not in-lieu of TEM measurements. Further characterization of the system will be necessary to examine to what exact surfactant coating can desorb during aerosolization, and to develop methods to promote surfactant desorption.

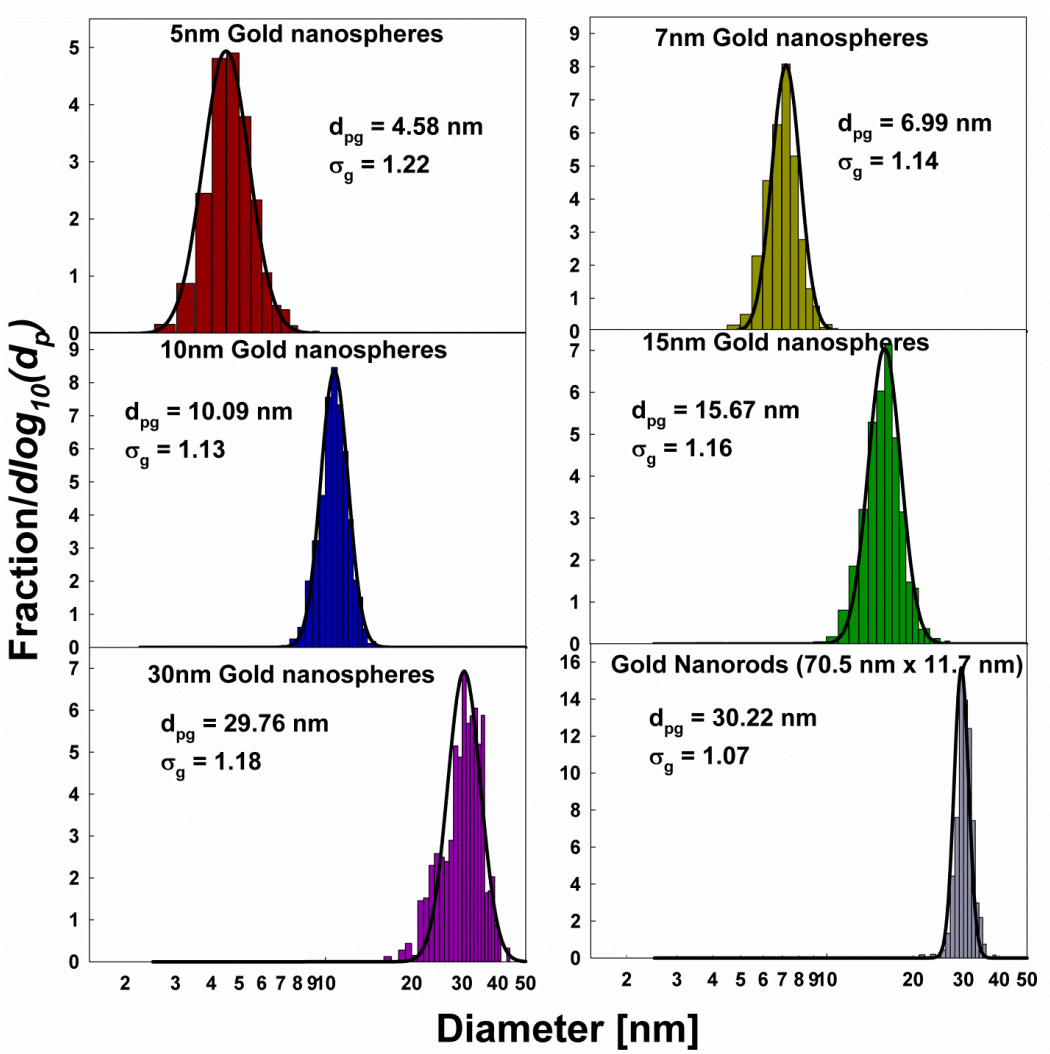

Figure 2.11. TEM inferred size distribution functions for gold nanospheres and GNRs.

2.3.6 Universal calibration curve

As remarked upon in section 2.3.1, total particle number concentrations integrated from size distribution functions should correlate directly with the particle concentration in suspension; independent of particle size, shape or chemical composition. Considering all samples, the equation (2.2) inferred number concentrations are plotted versus suspension concentration in Figures 2.12 (a) and (b). The results are separated in these two figures

because the LN system was disassembled and cleaned near the midpoint of this study (which spanned more than six months). During reassembly, the position of the ball-impactor changed slightly, changing the output particle size distribution function (which ultimately influences the calibration curve linking gas phase concentration to concentration in suspension). In spite of the change caused by reassembly, apparent in both Figure Figures 2.12 (a) and (b) is that the obtained gas phase concentration versus suspension concentration relationship does not depend upon particle size or chemical composition (i.e. proteins and gold nanospheres show similar results). For each set of results, a fit power law is displayed. For both plots the scaling exponent is found to be below unity; such exponents arise because at higher concentrations, there are proportionally more particles enclosed within large droplets, which are removed by the ball impactor. The differences in exponent and pre-exponential factor also arise because of changes in impactor position. Following cleaning, the exponent and pre exponential factor can be calibrated using a colloid sample standard with a known volume concentration.

While we do not observe any size dependency for the gas phase concentration versus liquid phase concentration relationship, there is noticeable scatter in the LN-IMS inferred number concentrations. Therefore, while it appears a universal calibration curve can be developed using a single type of nanoparticle (e.g. nominally 30 nm gold can be used as a standard for all particles and proteins, and can be used for polydisperse samples), suspension number concentration estimates via LN-IMS are only accurate to within +/- 20%. In many instances, this level of accuracy is sufficient; however, applications such as instrument calibration [141] may require greater level of accuracies; further refinement of

size distribution inversion techniques with LN-IMS will be necessary for improved accuracy.

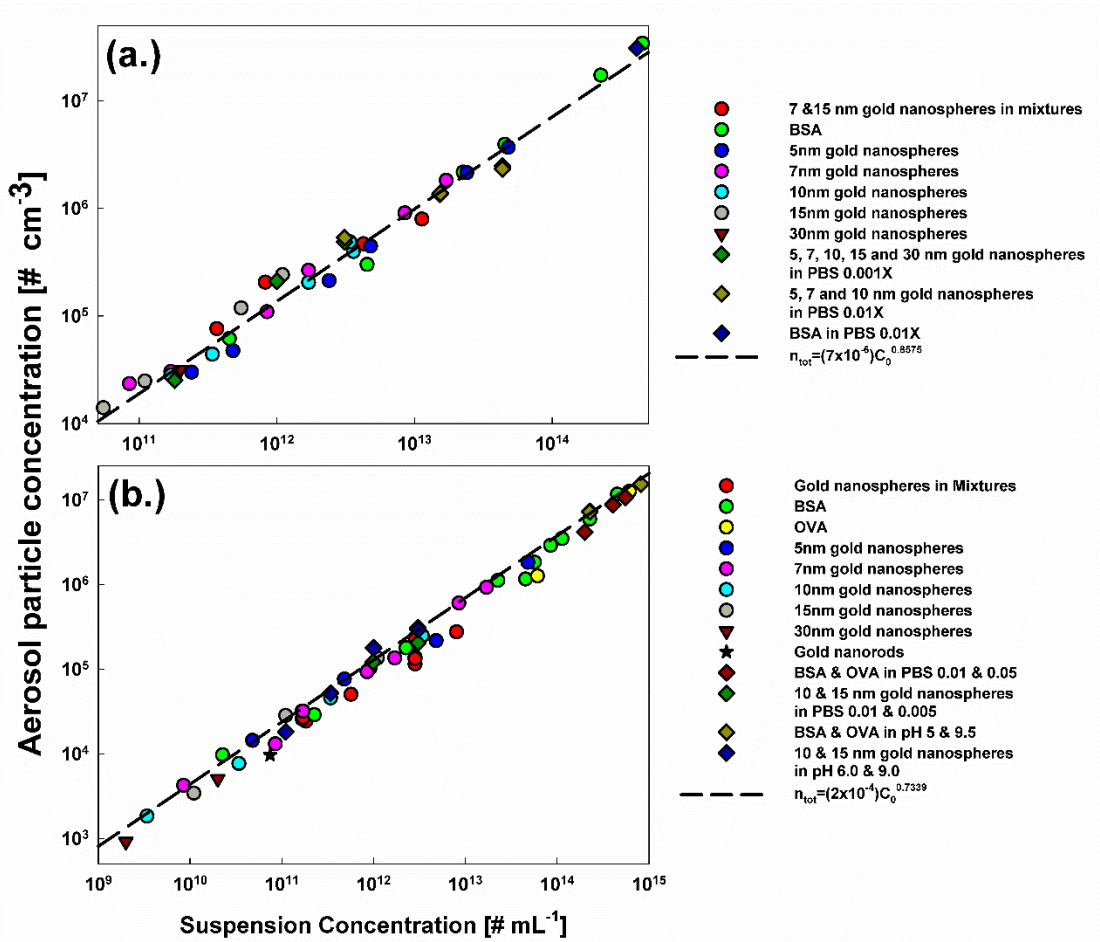

Figure 2.12. Plots of the gas phase particle number concentration as a function of the original suspension concentration: **(a.)** before disassembly and cleaning, **(b.)** after reassembly and impactor repositioning.

2.4 Conclusions

We have applied an LN-IMS measurement system for the measurement of gold nanosphere and nanorod as well as albumin protein size distribution function measurement. Through both experimental measurements and modeling, we show that it is possible to convert hydrosols to aerosols while minimally disturbing the particle size distribution

functions. Through comparison to TEM measurements, we show that LN-IMS measurements enable accurate inference of particle polydispersity, but that the size distribution function is shifted by surfactant coating which is not observed in TEM. Importantly, we demonstrate that the gas phase particle number concentration is a size, shape, and material property independent function of the liquid suspension concentration. In addition to these findings, we note that the ability to aerosolize nanomaterials down to 5 nm in size, preserving their size distribution, would enable a variety of analytical possibilities, including tandem ion mobility spectrometry [142, 143] to examine vapor uptake or the evaporation of particles, IMS-inductively coupled plasma mass spectrometry [103] to infer size resolved chemical composition, and IMS coupled with aerosol particle mass analysis [144]. Though such techniques have been applied to particles in liquid suspensions previously, in nearly all circumstances, aerosolization was accomplished with an electrospray, which as noted, has strict requirements on suspension salt concentration and electrical conductivity, limiting its use. The LN tested is capable of aerosolizing colloidal particles from hydrosols from a much wider range of conditions, and further, as it has higher throughput, leads to better counting statistics in gas phase measurements. We thus anticipate that LN based aerosolization will better facilitate characterization of sub 30 nm nanomaterials than electrospray based aerosolization.

Chapter 3

Liquid Nebulization-Ion Mobility Spectrometry Based Quantification of Nanoparticle-Protein Conjugate Formation

Summary

There is a dearth of routine techniques for nanoparticle-protein conjugate characterization. The most prominent change to a nanoparticle population upon conjugate formation is a shift in the nanoparticle size distribution function. However, commonly employed dynamic light scattering based approaches for size distribution characterization are difficult to apply to non-monodisperse samples, and further they are relatively insensitive to size shifts of only several nanometers, which are common during conjugate formation. Conversely, gas phase ion mobility spectrometry (IMS) techniques can be used to reliably examine polydisperse samples; the challenge with IMS is to convert nanoparticle-protein conjugates to aerosol particles without non-specific aggregation. Except in limited circumstances, electrospray based aerosolization has proven difficult to apply for this purpose. Here we show that via liquid nebulization (LN) with online dilution (with dilution factors up to 10,000) it is possible to aerosolize nanoparticle-protein conjugates, enabling IMS measurements of their conjugate size distribution functions. We specifically employ LN-IMS to examine bovine serum albumin binding to gold nanoparticles. Inferred maximum protein surface coverages (~0.025 nm^{-2}) from measurements are shown to be in excellent agreement with reported values for gold from quartz crystal microbalance measurements. It is also shown that LN-IMS measurements can be used to detect size distribution function shifts on the order of 1 nm, even in circumstances where the size distribution function itself has a standard deviation of ~5 nm. In total, the reported measurements suggest that LN-IMS is a potentially simple and robust technique for nanoparticle-protein conjugate characterization.

3.1 Introduction

There is a need to develop and advance techniques to examine the extent of binding of proteins to nanomaterials/nanoparticles [145-148]. Within the bloodstream or other biological milieu, it is known that a protein corona will form on a nanoparticle's surface, altering its bio-identity and eventual fate [149-153]. At present, even in vitro with prescribed proteins and protein concentrations, binding is difficult to quantify; to date no single technique is universally adopted for nanoparticle-protein conjugate quantification. The most notable change to an ensemble of nanoparticles upon protein binding is a shift of the nanoparticle size distribution function [154], hence it is the size distribution function that is most easily monitored to quantify the extent of protein binding. Size measurements of protein-nanoparticle conjugates have been carried out commonly with dynamic light scattering (DLS) [40, 155, 156]. However, DLS is only applicable to highly monodisperse samples, with results skewed towards larger particles in polydisperse sample measurements. This is problematic for all but the most narrowly distributed particle size distributions (i.e. those with geometric standard deviations below 1.1). Polydisperse sample size distribution measurements can be better made via nanoparticle tracking analysis (NTA) [43, 157, 158]. Unfortunately, NTA has limitations for particles/conjugates smaller than 30 nm in size; this prohibits direct examination of a number of nanoparticles as well as individual protein molecules. Further, both techniques are relatively unreliable in detecting small (less than ~5 nm) size shifts, i.e. the data deconvolution schemes applied can lead to low measurement precision.

Techniques to examine protein nanoparticle-binding can be developed which are more precise than DLS and NTA. However, many of these techniques are limited to specific nanoparticle chemical compositions. For example, techniques relying on

fluorescent labelling [145] or shifts in optical/plasmonic properties [159, 160] of nanoparticles upon protein binding require specific particle optical properties. Liquid phase size measurement techniques, such as asymmetric flow field fractionation [146, 148] and analytical ultracentrifugation [81], enable more rigorous quantification of size distribution functions, yet need to be coupled to appropriate detectors. Universal particle detectors for a variety of particle chemistries are not widely available [80]. Another alternative is gas phase ion mobility spectrometry (IMS) [161] with a differential mobility analyzer (DMA) [83, 88, 89], which is a commonly employed technique for size distribution measurements of aerosol particles. In conjunction with condensation based single particle detectors [53], DMAs facilitate size distribution function analysis in the 2-500 nm diameter range, and unlike DLS and NTA, DMA data deconvolution schemes require minimal assumptions about the shape of the size distribution [84]. IMS is therefore more easily applied to polydisperse and multimodal samples [82], and size shifts of several nanometers can be reliably detected [100]. The challenge in applying IMS to nanoparticle-protein conjugates is naturally that the conjugates must be introduced into the gas phase (aerosolized) without perturbing their size distribution functions. To date, aerosolization of liquid phase samples has been accomplished almost exclusively with charge reduction electrosprays [88, 89, 101]. Notable demonstrations of the potential of IMS in nanoparticle-protein and nanoparticle-small molecule conjugate analysis have been carried out by Zachariah and coworkers [93, 97-100, 137], with such charge reduction electrospray sources. Their measurements have consistently shown that by controlling the droplet size and concentration of analyte [137], aerosolization with preservation of size distribution functions from the liquid phase is possible. In spite of this success, IMS has not been widely

adopted in nanoparticle-protein conjugate size analysis, in large part because electrospray based aerosolization requires solutions/suspensions with electrical conductivities in narrow range, as well as the *a priori* removal of non-volatile solutes. These conditions are often mutually exclusive with the conditions needed to maintain nanoparticle stability in suspensions, i.e. the addition of salts and removal of surfactants leads to aggregation and settling of nanoparticles. As an example, noble metal nanoparticles and nanorods often need to be heat treated post-electrospray to remove non-volatile solute coating [91, 118], and such nanoparticles do aggregate and settle over the course of several days in electrosprayable (1-100 mM ammonium acetate) suspensions [155].

Liquid nebulizers (LNs) have recently been developed with online, ultrahigh purity water dilution (by a factor of up to 10^4). Such nebulizers enable hydrosol to aerosol conversion for nanoparticles as small as 5 nm [62, 162], and LN based aerosolization has proven capable of preserving nanoparticle size distributions for polydisperse and multimodal samples (where peaks differ by less than 5 nm). In contrast with electrosprays, LN based aerosolization requires neither non-volatile solute removal nor control of the suspension electrical conductivity. The purpose of this study is to apply LN-IMS analysis for the first time to quantify bovine serum albumin binding to nominally 20 nm, 30 nm, and 50 nm gold nanoparticles (GNPs), demonstrating that this approach can be a simple and robust method for nanoparticle-protein conjugate analysis.

3.2 Materials and methods

3.2.1 Materials and sample preparation

GNPs with nominal diameters of 20, 30, and 50 nm were purchased from Nanocomposix, Inc (San Diego, USA). Electron microscopy revealed these samples had mean diameters ± standard deviations of 18.6 ± 2.3 nm, 30.8 ± 3.3 nm, and 51.0 ± 5.7 nm, respectively. GNP surfaces were pretreated with tannic acid to stabilize them in aqueous suspension. Bovine serum albumin (BSA) was purchased from Sigma Aldrich (Saint Louis, MO, USA). BSA solutions were prepared by dispersing BSA powders in deionized (DI, obtained with a SpectraPure filtration system) water. GNPs suspensions, with manufacturer provided number concentrations (ranging from 3×10^9 to 8×10^{10} particles mL^{-1}) were mixed with known concentration BSA samples in a suspension volume of 1 mL in polypropylene centrifuge tubes. 5-7 GNP:BSA number concentration ratios (ranging from 1:3 to 1:12,000) were examined for each GNP size. Prior to measurements, samples were placed in an incubator (Alkali Scientific, FL, USA) at 38.0^o C for 16 hours. Additionally, for 50 nm GNPs, incubation was also performed at 4^o C. No other sample preparation was required prior to LN-IMS measurement and nanoparticles were observed to remain stable in suspension during incubation; this is distinct from most studies utilizing charge reduction electrospray based aerosolization where electrical conductivity modulation and analyte preconcentration are needed prior to analysis.

3.2.2 LN-IMS measurements

The size distribution functions of bare GNPs and GNP-BSA conjugates were measured via a liquid nebulizer-ion mobility spectrometry (LN-IMS) system. Chapter 2

provides details of the operation and schematics of this system. Briefly, in the LN employed (LiquiTrak® Model 7788, Kanomax Fluid Measurement Technologies, Inc., St Paul, MN, USA), the GNP-BSA suspension in 0.01 – 1 mL min^{-1} is mixed with 100 mL min^{-1} of ultrahigh purity water (which contains total organic carbon and non-volatile residues below 1ppbv, was treated with 165nm UV light, and was passed through 10 nm and 20 nm particle filtration systems as well as a mixed bed ion exchange resin prior to system introduction). The LN produces droplets with a geometric mean diameter of 99.8 nm and a geometric standard deviation of 2.32. Upon drying, aerosolized GNP:BSA conjugates were passed out of the LN using a flow of ultrahigh purity air, with neither fragmentation nor specific aggregation caused by the aerosolization process. For IMS, the aerosolized conjugates were sent into a DMA (both models 3081 and 3085, TSI Inc., Shoreview MN, were applied in measurements)[52] followed by a butanol based condensation particle counter (CPC, model 3075, TSI Inc). The DMA-CPC combination was operated as scanning mobility particle spectrometer (SMPS) [125], with 120 second scans applied and at least eight measured spectra per sample. Raw data consisted of CPC measured concentration as a function of mean voltage across the DMA electrodes. Using manufacturer provided software (Aerosol Instrument Manager), data were inverted to reveal the size distribution function, $dn/dlog_{10}(d_p)$, i.e. the aerosol particle number concentration per unit log_{10} diameter (with diameter in nanometers) as a function of diameter. Diameter was inferred using the Stokes-Millikan equation, found to be valid for nearly spherical particles in a variety of studies where air was applied in IMS measurement [127, 139].

The sample flow:dilution flow was adjusted from 1:100 to 1:10,000 during measurements. Higher sample flows (less dilution) were applied to examine the size distribution functions of gold nanoparticle conjugates, while lower sample flows were applied to directly detect free BSA molecules in the suspension. As described in Chapter 2, using a LN-IMS specific calibration curve (relating the measured aerosol concentrations to liquid suspension concentrations) the size distribution function of the free BSA was used to infer the unbound BSA suspension concentration, and the shift in size distribution functions for GNP-BSA conjugates was examined as a function of unbound BSA concentration. We remark that the unbound BSA concentration was consistently found to be a factor of ~2 lower than the nominal BSA number concentration based on what was added to GNP:BSA suspensions. This is attributable to protein binding to the wall of the polypropylene vial used in incubation, an influence not considered in prior studies of GNP-BSA conjugation.

3.3 Results & discussion

3.3.1 Size distribution functions

After data inversion, which corrects for the transmission through the DMA [163], the fraction of multiply charged particles examined [164], and the depositional losses of particles in system tubing [129], LN-IMS measurements lead to inference of the gas phase size distribution function, which is specifically represented as the parameter $dn/d\log_{10}(d_p)$, i.e. the gas phase number concentration per unit $\log_{10}$ particle diameter (in nanometers). Integration of $dn/d\log_{10}(d_p)$ across the entire diameter range yields the gas phase number concentration of particles aerosolized by the LN-IMS. Size distribution functions

(averaged over more than five spectra) of 20, 30, and 50 nm GNPs are displayed in Figure 3.1 for selected BSA:GNP number concentration ratios. Size distributions were corrected for the dilution factor employed in the LN, hence the displayed values are proportional to the size distribution function in the original suspensions [162].

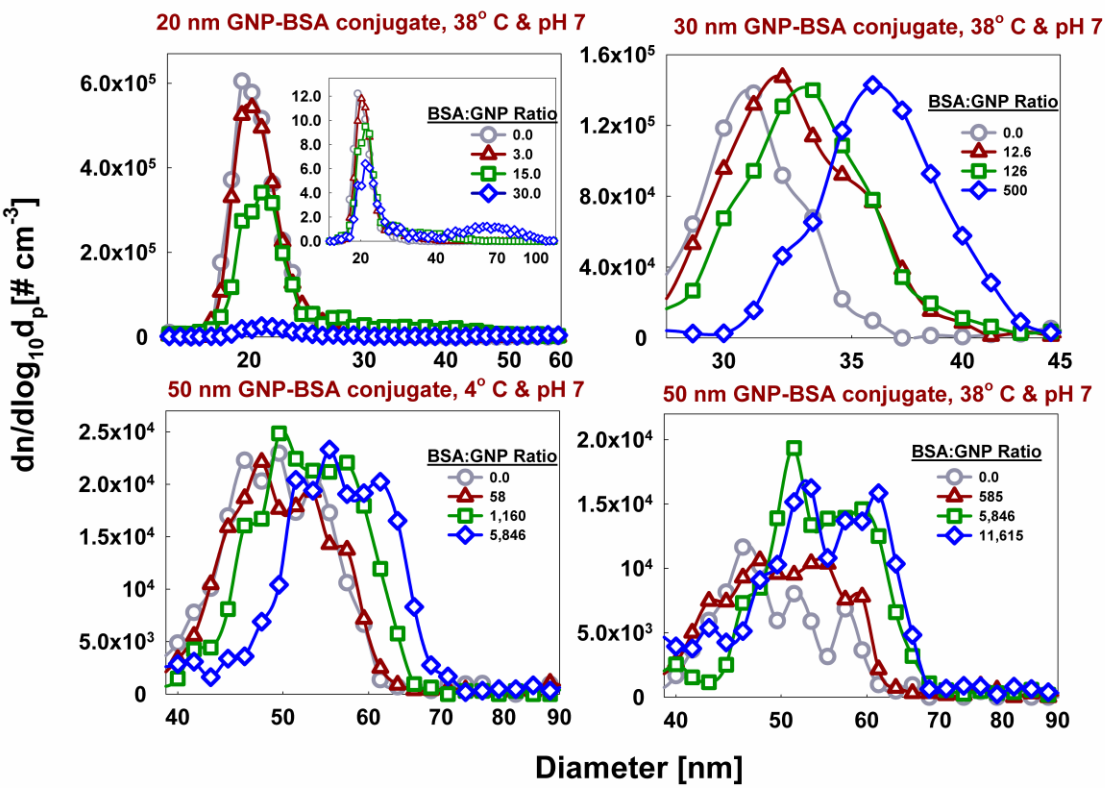

Figure 3.1. LN-IMS inferred size distribution functions (expressed as gas phase number concentrations per unit $\log_{10}$ diameter, $dn/d\log_{10}d_p$) for GNP-BSA conjugates with varying BSA:GNP number concentration ratios in aqueous suspension. The upper left inset displays results for nominally 20 nm GNPs but with size distribution functions normalized by the total number concentration for each measurement.

Clearly evident for all samples except the nominally 20 nm diameter GNPs is that with increasing BSA:GNP number concentration ratio, the peaks in size distributions corresponding to GNPs shift to the right. This is indicative of conjugate formation as well as an increased number of proteins bound at higher BSA concentration in suspension. However, distributions are noticeably broad relative to the extent of shift, making difficult

quantification of the extent of shift simply by comparing mode values in distributions (as has been common practice in prior studies[97]). Moreover, shifts are less evident for nominally 20 nm GNPs; instead we observed a decreasing number concentration near 20 nm and an increasing number concentration about 60 nm in LN-IMS measurements, with increasing BSA:GNP ratios.

A more appropriate method to quantify the extent of shift in size distribution is through the determination of a mean diameter ($d_{p,ave}$), a dilution factor corrected conjugate volume concentration (V_{tot}), and a geometric standard deviation (σ_g), via the equations:

$$d_{p,ave} = \frac{\int_{-\infty}^{\infty} \frac{dn}{dlog_{10}d_p} d_p dlog_{10}d_p}{\int_{-\infty}^{\infty} \frac{dn}{dlog_{10}d_p} dlog_{10}d_p} \tag{3.1}$$

$$V_{tot} = \frac{\pi}{6} \int_{-\infty}^{\infty} \frac{dn}{dlog_{10}d_p} {d_p}^3 dlog_{10}d_p \tag{3.2}$$

$$\sigma_g = exp\left(\sqrt{\frac{\int_{-\infty}^{\infty} \frac{dn}{dlog_{10}d_p} ln^2\left(\frac{d_p}{d_{p,g}}\right) dlog_{10}d_p}{\int_{-\infty}^{\infty} \frac{dn}{dlog_{10}d_p} dlog_{10}d_p}} \right) \tag{3.3}$$

$$d_{p,g} = \exp\left(\frac{\int_{-\infty}^{\infty} \frac{dn}{dlog_{10}d_p} ln(d_p) dlog_{10}d_p}{\int_{-\infty}^{\infty} \frac{dn}{dlog_{10}d_p} dlog_{10}d_p} \right) \tag{3.4}$$

These parameters provide information on (1) the growth of conjugates, either by BSA binding or conjugate-conjugate binding (aggregation), (2) whether growth is due to BSA binding only (increasing V_{tot}) or conjugate-conjugate binding (which would leave V_{tot} constant), and (3) the mechanism of binding, as different binding models will predict differential changes in the geometric standard deviation, respectively. Excluding the portion of the size distribution function attributed to isolated BSA, equation (3.1-3) calculated parameters are plotted in Figure 3.2 as a function of unbound BSA concentration

in suspensions. Error bars represent the standard deviation of each data point, evaluated by performing calculations for each measured size distribution function separately.

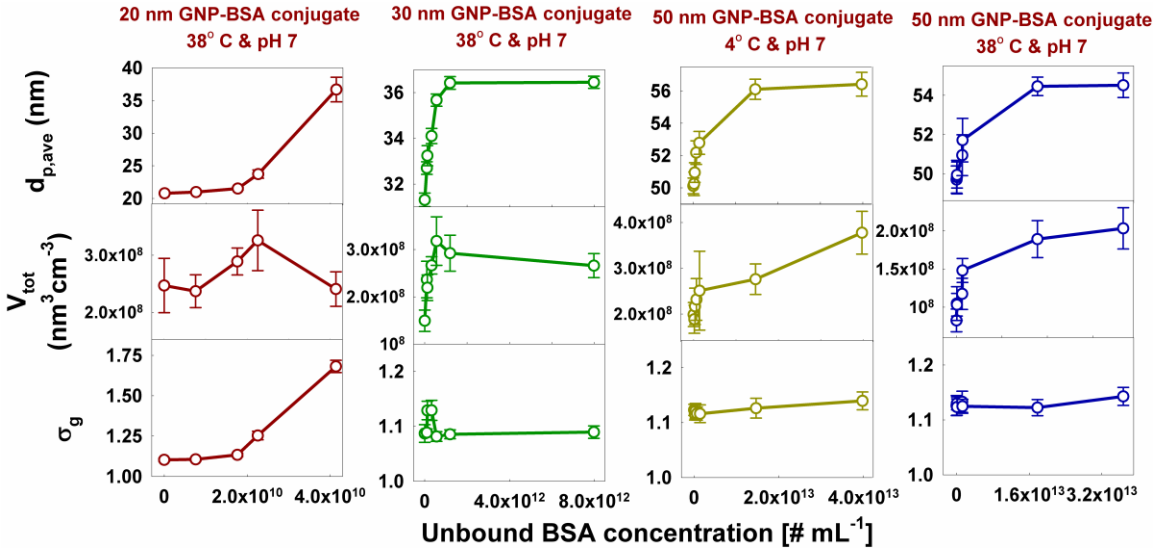

Figure 3.2. A summary of the mean diameter ($d_{p,ave}$), gas phase volumetric concentration (V_{tot}), and geometric standard deviation (σ_g) as a function of the unbound BSA concentration in aqueous suspension.

Focusing first on the nominally 30 nm and 50 nm GNPs, we find for both samples that $d_{p,ave}$ increases rapidly at low BSA concentrations but appears to reach a maximum value as BSA concentration is further increased. Unlike alternative techniques, size shifts on the order of 1-2 nm are clearly detectable and larger than the measurement to measurement variability, despite the conjugate size distribution functions themselves having standard deviations larger than 1-2 nm. This demonstrates directly that LN-IMS can be used to probe the earliest stages of conjugate formation, even for nanoparticles whose size distribution does not shift appreciably due to protein binding. Volume concentrations for these samples show similar behavior, and geometric standard deviations remain constant near 1.1 (indicating the samples are not perfectly monodisperse but remain narrowly distributed during measurements). For the nominally 50 nm GNPs, a larger

extent of binding is observed at lower temperature. Qualitatively, these measurements suggest that BSA binding to GNPs is reversible (i.e. samples are equilibrated) which is in line with the conclusions of prior studies of GNP-protein conjugation [40, 155, 165]. We examine the mechanism of binding further in the subsequent section. For 20 nm GNPs, unique behavior is observed; the $d_{p,ave}$ versus BSA concentration curve is concave upward, and the volume concentration stays relatively constant, and geometric standard deviation increases drastically (this was expected as samples became bimodal at increasing BSA concentration). In total, inverted size distribution functions and quantification of size distributions via equations (3.1-3) reveal that LN-IMS is a viable approach to detect ~1-2 nm shifts in nanoparticle size brought by conjugation with proteins, even in instances where the size distribution function varies by more than this amount.

3.3.2 Comparison with binding & aggregation models

Poor size shift precision for nanoparticle-protein conjugates can limit the amount of information gained via measurements. For this reason, in studies utilizing DLS,[40] or in prior IMS studies in which only the mode diameter was examined,[93, 97] only a maximum surface coverage of nanoparticles (expressed as the number of protein binding sites per unit nanoparticle surface area) has been inferred. For BSA binding onto gold, reported surface coverages near body temperature reported previously vary from study to study. Using a quartz crystal microbalance (QCM) Brewer et al[165] reported a value of 0.037 nm^{-2} and Kaufman et al[166] reported values ranging from 0.020 to 0.033 nm^{-2} for flat surfaces. Using IMS coupled with mass analysis, Guha et al[93] determined a value of 0.027 nm^{-2} for nominally 30 nm, but in a previous study with IMS Tsai et al[97] reported

values of 0.023 nm^{-2}, 0.017 nm^{-2}, and 0.014 nm^{-2} for nominally 10 nm, 30 nm, and 60 nm GNPs, respectively. By examining precisely calculated mean diameters in inverted size distributions, here we show that not only can LN-IMS be used to infer surface coverages in line with QCM measurements and two dimensional IMS-mass analyses, but also using a Langmuir-like binding model (i.e. an equilibrium, site-dependent binding model) the effective protein concentration above a GNP surface (n_{eff}) can be determined. This model links the nanoparticle-conjugate mean diameter to the *[X]* (the assumed size-independent site surface density or maximum surface coverage) and n_{eff} via the equations:

$$d_{p,ave} = \frac{\int_{-\infty}^{\infty} \frac{dn}{dlog_{10}d_{p,0}}\Big|_0 (\sum_{i=0}^{\infty} d_{p,i}P_i) dlog_{10}d_{p,0}}{\int_{-\infty}^{\infty} \frac{dn}{dlog_{10}d_{p,0}}\Big|_0 dlog_{10}d_{p,0}} \quad (3.5)$$

where $\frac{dn}{dlog_{10}d_{p,0}}\Big|_0$ is the nanoparticle size distribution function in the absence of protein, $d_{p,i}$ is the nanoparticle's effective mobility diameter with *i* protein molecules bound ($d_{p,0}$ is the bare nanoparticle diameter), and P_i is the probability that a nanoparticle with a diameter $d_{p,0}$ has i protein molecules bound to its surface at equilibrium. Following prior work on linking binding to analyte size shifts observed by IMS,[167-169], first, we note that P_i can be expressed as:

$$P_i = \frac{n_i}{\sum_{k=0}^{k=\infty} n_k} = \frac{\frac{n_i}{n_0}}{1.0+\sum_{k=1}^{k=\infty} \frac{n_k}{n_0}} \quad (3.6)$$

where n_i is the number concentration of nanoparticles with i proteins adsorbed onto their surfaces, and n_o is the number concentration of bare nanoparticles. At equilibrium, the ratio $\frac{n_i}{n_0}$ (or $\frac{n_k}{n_0}$) in equation (3.6) can be linked to the dimensionless equilibrium binding coefficients $\left[K_{eq}\right]_{j-1\rightarrow j}$ for the reaction: $n_{j-1} + n_a \rightleftharpoons n_j$ via the equation:

$$\frac{n_i}{n_0} = \frac{n_1}{n_0}\frac{n_2}{n_1} \ldots \frac{n_{i-1}}{n_{i-2}}\frac{n_i}{n_{i-1}} = \prod_{j=1}^{i}\left[K_{eq}\right]_{j-1\rightarrow j} \tag{3.7}$$

Assuming that each nanoparticle has $[X]\pi d_{p,0}^2$ specific sites where proteins can bind that the effective protein concentration above a site is n_{eff}, and that the protein adsorption and desorption rate coefficients are exactly equal in magnitude (i.e. they are diffusion limited reactions), $\left[K_{eq}\right]_{i-1\rightarrow i}$ can be expressed as:

$$\left[K_{eq}\right]_{j-1\rightarrow j} = \frac{n_a[X]\pi d_{p,0}^2 - j + 1}{j n_{eff}} \tag{3.8}$$

Substitution of equations (3.7-8) into equation (3.6) leads to:

$$P_0 = \frac{1.0}{1.0 + \sum_{k=1}^{k=[X]\pi d_{p,0}^2}\left(\left(\frac{n_a}{n_{eff}}\right)^k \prod_{j=1}^{j=k}\left(\frac{\left[[X]\pi d_{p,0}^2 - j + 1\right]}{j}\right)\right)} \tag{3.9}$$

$$P_i = \frac{\left(\frac{n_a}{n_{eff}}\right)^i \prod_{j=1}^{i}\left(\frac{\left[[X]\pi d_{p,0}^2 - j + 1\right]}{j}\right)}{1.0 + \sum_{k=1}^{k=[X]\pi d_{p,0}^2}\left(\left(\frac{n_a}{n_{eff}}\right)^k \prod_{j=1}^{j=k}\left(\frac{\left[[X]\pi d_{p,0}^2 - j + 1\right]}{j}\right)\right)} \qquad i \geq 1 \tag{3.10}$$

The distinct point of our Langmuir-like model differs, which differs slightly for the traditional Langmuir model, is that our model applied for discrete numbers of proteins. Figure 3.3 displays P_i values a at different n_a/n_{eff} ratios with $d_{p,0}$ = 30.0 nm and [X] = 0.060 # nm^{-2}, showing the as n_a/n_{eff} increases the mode P_i value increases.

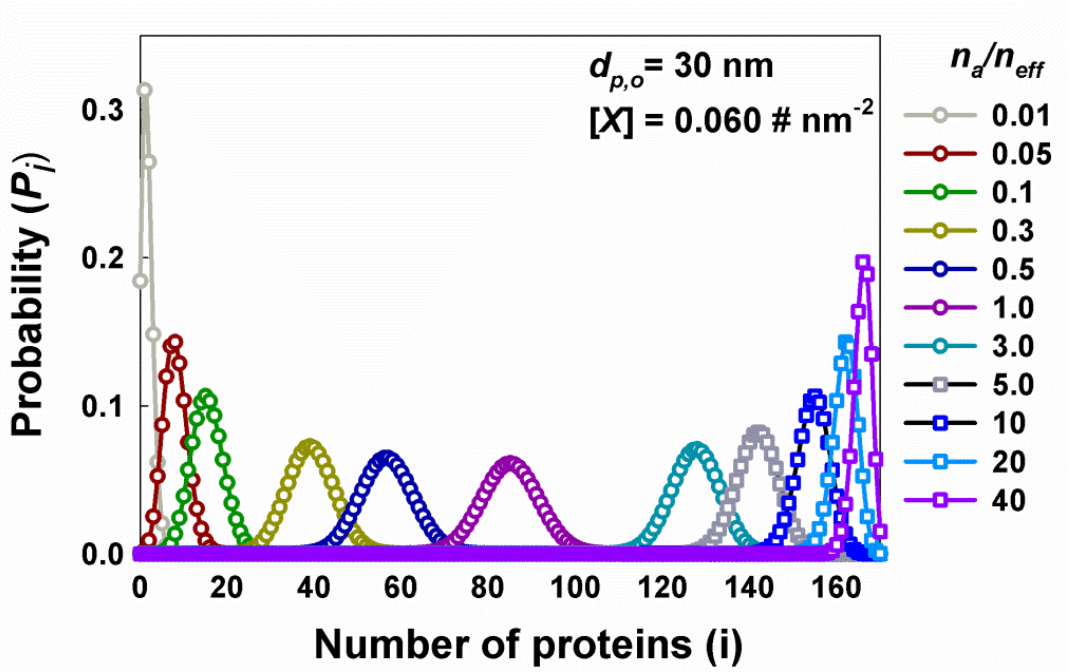

Figure 3.3. The probability P_i that a nanoparticle has i proteins bound (at equilibrium) predicted by the Langmuir-like model at various n_a/n_{eff} ratios ($d_{p,o}$ = 30.0 nm and [X] = 0.060 # nm^{-2}).

Various models can be developed for $d_{p,i}$, the effective mobility diameter of a nanoparticle-protein conjugate [97, 99]. However, based on prior theoretical calculations[128] and mobility measurements of non-spherical aerosol particles [118], we find that unless extremely non-spherical particles are expected to result from binding (for which there is no evidence), it is reasonable to approximate GNP:BSA conjugates as spherical, with mobility diameters equal to their volume equivalent diameters. Mobility diameters, $d_{p,i}$, are hence calculated as:

$$d_{p,i} = \left(d_{p,0}^3 + i d_{pro}^3\right)^{1/3} \tag{3.11}$$

where d_{pro} is the mobility diameter of a BSA monomer, measured to be 6.31 nm via IMS and in agreement with prior IMS[131, 133] and ultracentrifugation measurements [80]. Using best fit values for *[X]* and n_{eff}, equation (3.5) predicted $d_{p,ave}$ values (taking measured distributions $\left.\frac{dn}{dlog_{10}d_{p,0}}\right|_0$ and concentrations n_a as inputs) are plotted in comparison to experimentally inferred values in Figure 3.4.

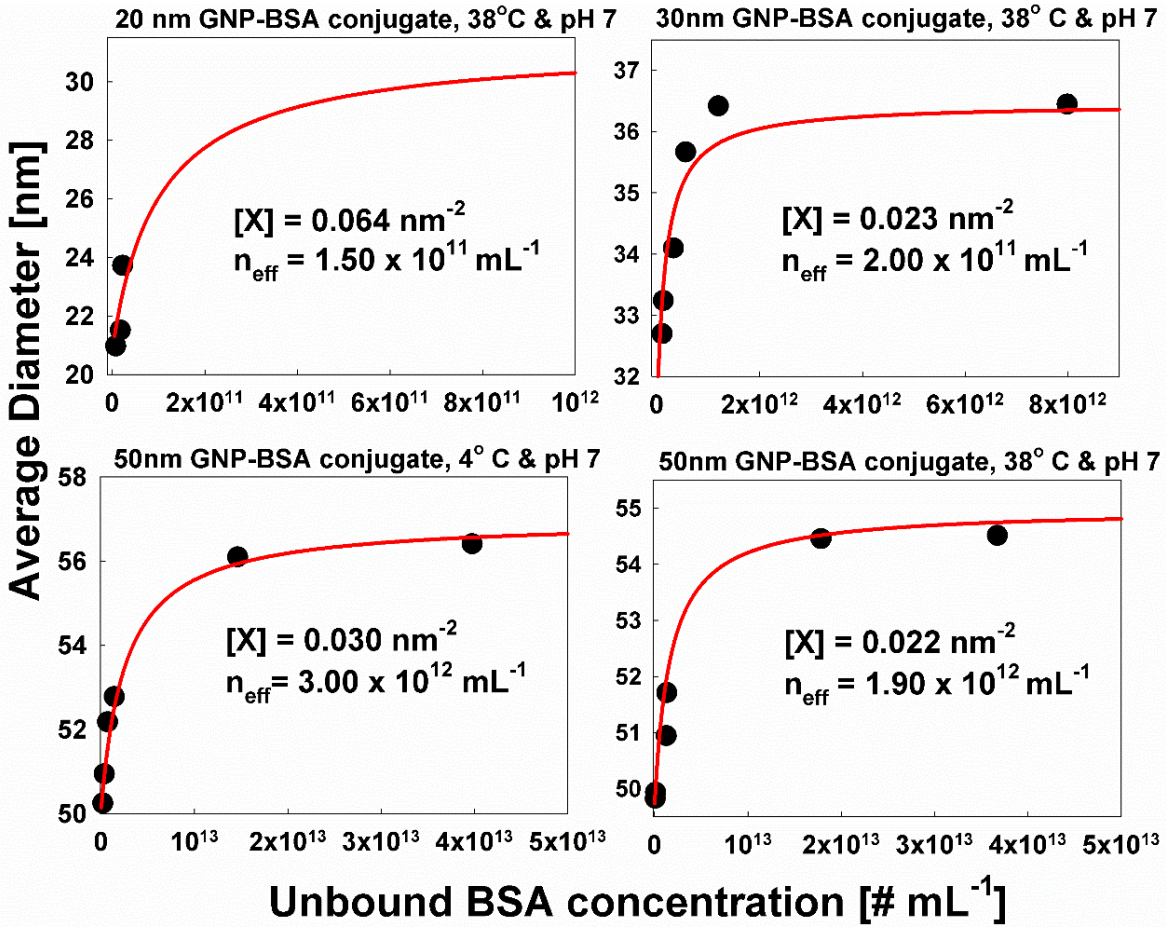

Figure 3.4. The measured (black circles) and calculated (red curves) average diameters of GNP-BSA conjugates as functions of the unbound BSA concentration. [X] refers to the site surface coverage parameter employed in the Langmuir-like sorption model, and correspondingly n_{eff} is the inferred protein concentration above a surface site.

For nominally 20 nm gold nanospheres, only three data points were used, as the appearance of a second mode near 60 nm cannot be explained via the Langmuir-like equilibrium binding model alone. Binding model parameters inferred for these nanoparticles are thus only shown for completeness and are not utilized in comparison to prior results. For the 30 nm and 50 nm GNPs (at both 4^o C and 37^o C), the two parameter model can be fit extremely well to measurements, and the resulting surface coverage values, ranging from 0.022-0.030 nm^{-2} are in excellent agreement with the previous QCM measurements and the IMS-mass measurements of Guha et al [93]. This further confirms the applicability of LN-IMS analysis to examine nanoparticle-protein conjugates, and suggests that in electrospray based aerosolization studies [97], mode mobility diameter measurements of nanoparticles may be skewed by the presence of non-volatile residue, which would directly influence inferred surface coverage values. Interestingly, the effective surface concentrations of proteins (which are linked directly to the dissociation constant of proteins from conjugates) are found to decrease by almost an order of magnitude as GNP nominal diameter decreases from 50 nm to 30 nm. This suggests that with increasing surface curvature, BSA is adsorbed with increasing affinity to GNPs; this is also supported by the appearance of a larger mode in nominally 20 nm distributions, which is presumably brought about by conjugate-conjugate aggregation. Though nanoparticle size dependencies on conjugate formation have been examined previously [170, 171], this specific finding appears to be new, and size dependencies in the strength of nanoparticle-protein bounds will need to be examined in future work.

Though the comparison presented in Figure 3.4 suggests that at an equilibrium, Langmuir-like binding model (equation 3.5) satisfactorily describes LN-IMS

measurements, it is important to compare results to alternative models. One possibility is the irreversible condensation of proteins on nanoparticles, forming continuously growing conjugates at a rate limited by the diffusion limited aggregation rate of proteins onto nanoparticles/conjugates [172]. To compare such a condensation model to measurements, we perform constant number Monte Carlo simulations[173] to predict the evolution of the size distribution functions of protein-nanoparticle conjugates formed via irreversible, diffusion limited protein condensation.

The constant number Monte Carlo simulation approach, developed by Smith and Matsoukas [173], is a relatively simple and accurate method for monitoring the evolution of particle size distribution functions. Here, we adapt it to make predictions about the size distribution functions of originally lognormally distribution particles as noted in the main text. For the Langmuir-like sorption model, evolution of the distribution in time need not be considered. Instead, 10^5 nanoparticle diameters are sampled from the lognormal distribution. For each sampled nanoparticle, using the noted equations for P_i and with prescribed values of $[X]$ and n_a/n_{eff}, an integer number of proteins bound (i) is also sampled. The bare nanoparticle diameter, number of proteins bound, and protein diameter (assumed) are then used to calculate the conjugate diameters. Binning of conjugate diameters enables construction of a size distribution function.

The size distribution functions of nanoparticles upon *irreversible* protein binding events (termed condensation here) were also simulated by applying constant number Monte Carlo simulation. The key differences with the Langmuir-like binding model are that (1) binding can occur indefinitely, i.e. there is no maximum surface coverage, and (2) protein dissociation from the conjugate is not considered. For this procedure we again selected

10^5 nanoparticle diameters from prescribed size distribution functions. Subsequently, at each timestep 100 of these nanoparticles are sampled to undergo protein binding/condensation with the probability of selection proportional to the diffusion limited binding rate between protein and nanoparticle/nanoparticle-protein conjugate. The rate coefficient, k_i, for this reaction, is expressed as:

$$k_i = 2\pi(d_{p,i} + d_{pro})(D_{p,i} + D_{pro}) \tag{3.12}$$

where D denotes the diffusion coefficient for conjugates and isolated proteins (equivalent to $\frac{kT}{3\pi\mu d}$, where k is Boltzmann's constant, T is temperature, μ is the solvent's dynamic viscosity, and d is the diameter of the entity in question). The probability of condensation $P_{c,i}$ is calculated as:

$$P_{c,i} = \frac{k_i}{\sum_{j=1}^{j=N} k_j} \tag{3.13}$$

where N is the total number of sampled nanoparticles. After condensation, nanoparticle diameters are increased, and the procedure is repeated. The size distribution function hence evolves over time, with the true rate proportional to the number concentrations in suspension. Figures 3.5-7 display simulation results the Langmuir-like sorption model and the irreversible condensation sorption model. Specifically, for lognormally distributed nanoparticles with a geometric mean diameter of 30 nm and geometric standard deviations near 1.1, 1.3, and 1.5 (near monodisperse to highly polydisperse), the normalized size distributions functions (fraction of particles per nm), mean nanoparticle-conjugate

diameter, and geometric standard deviation are plotted as functions of the suspension protein concentration (n_a) to effective protein concentration (n_{eff}) ratio for the Langmuir-like model, and the product of suspension protein concentration and simulation time step for the condensation model. As the abscissas on all plots are directly proportional to protein concentration in suspension, results are qualitatively comparable to measurements results reported in Figures 3.1 and 3.2.

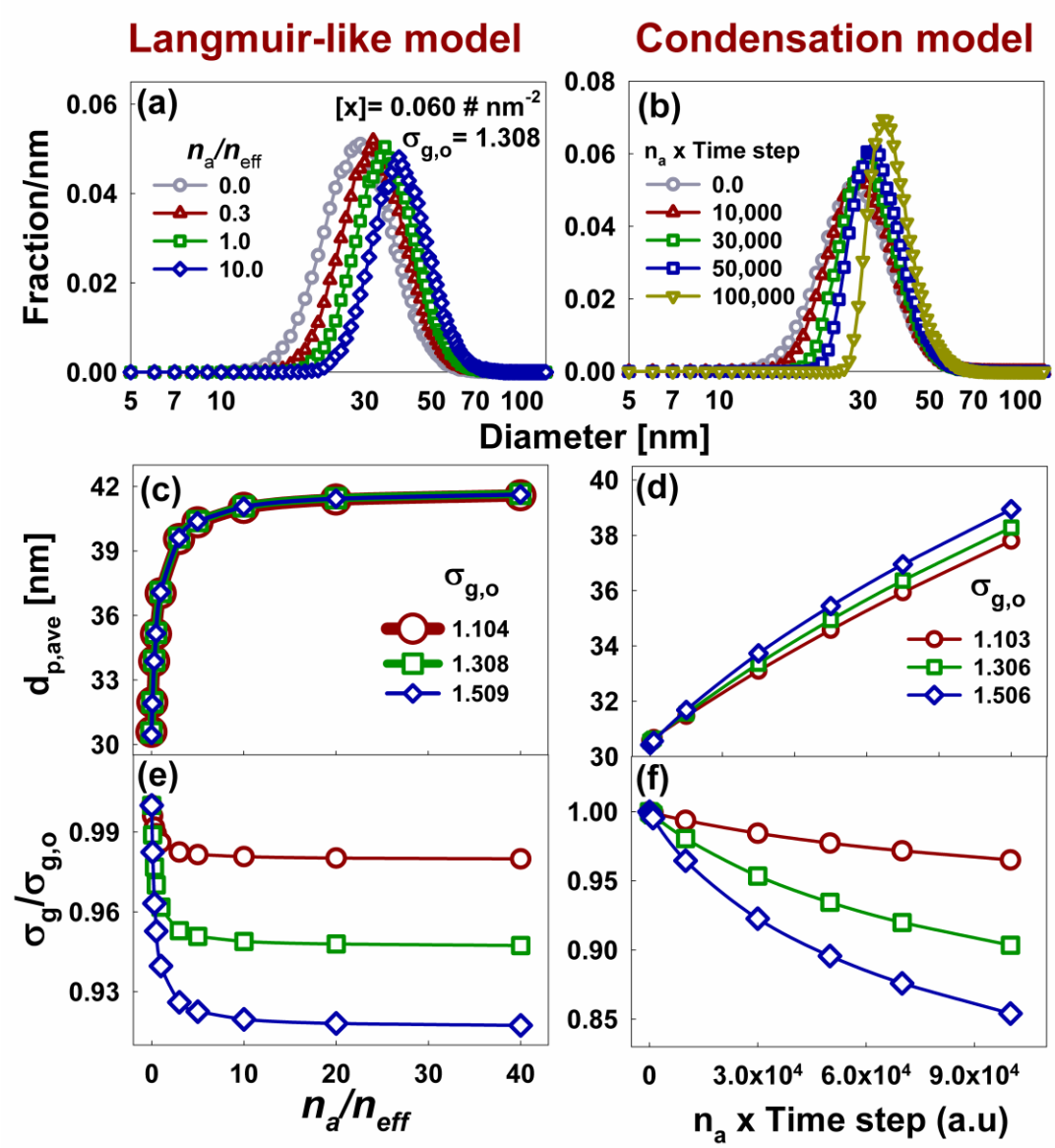

Figure 3.5. The normalized size distribution functions (**a & b**), mean diameters (**c & d**), and normalized geometric standard deviations (by the baseline value, **e & f**) of nanoparticle-protein conjugates as predicted by the Langmuir-like model (equation 3.5) and an irreversible protein condensation model for lognormally distributed nanoparticles. Plots **c-f** are shown for variable initial geometric standard deviations.

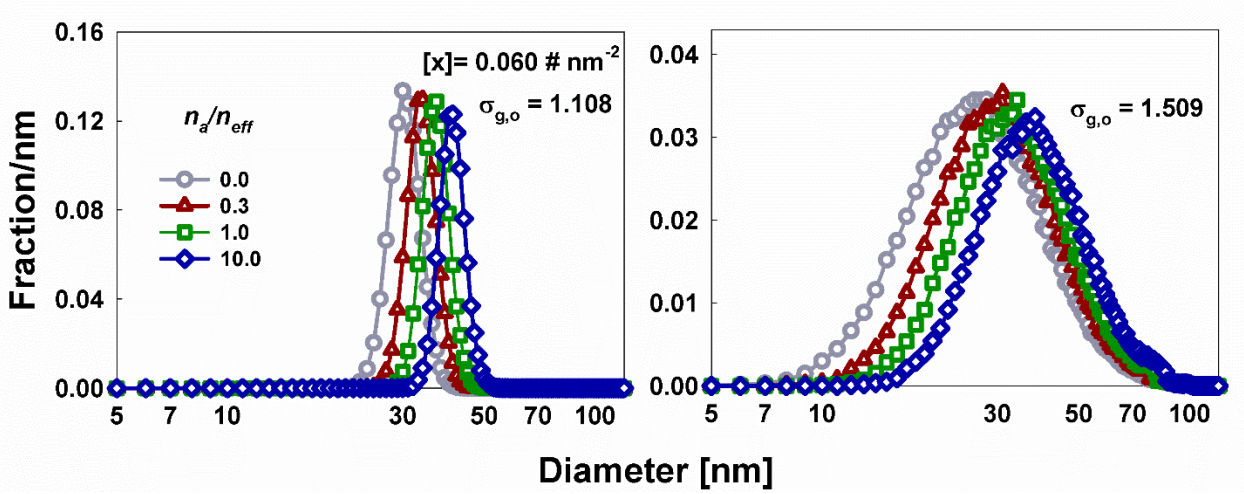

Figure 3.6. Simulated size distribution functions with the constant number Monte Carlo algorithm considering the Langmuir-like binding model with $\sigma_{g,o}$=1.1 (left) and 1.5 (right). The bare nanoparticle geometric mean diameter was 31.1 nm.

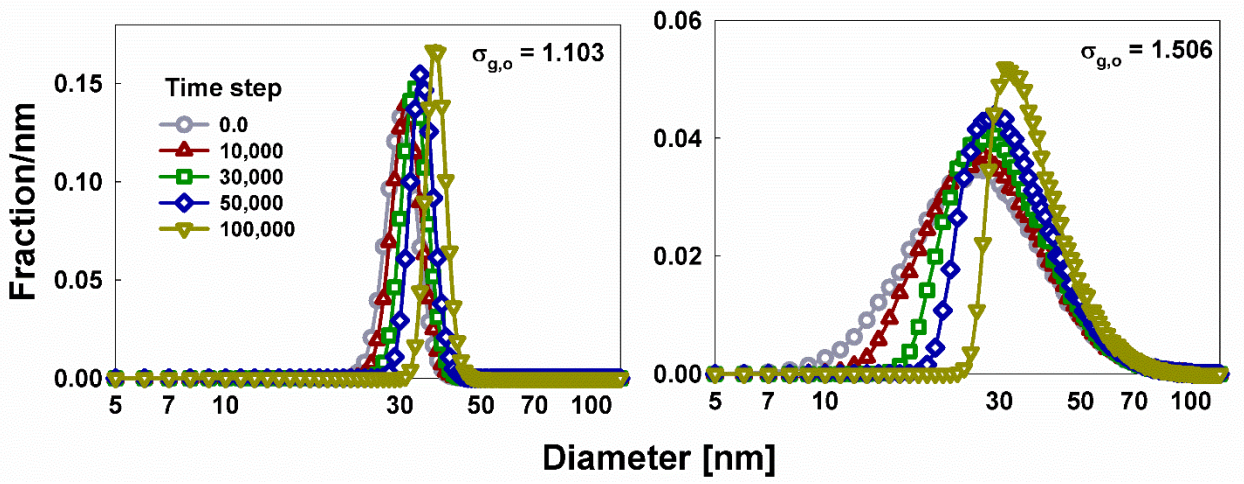

Figure 3.7. Simulated size distribution functions with the constant number Monte Carlo algorithm considering irreversible condensation with $\sigma_{g,o}$=1.1 (left) and 1.5 (right). The bare nanoparticle geometric mean diameter was 31.1 nm.

Apparent is that the condensation model predicts a steady increase in the mean nanoparticle-protein conjugate diameter as well as a steady-decrease in the geometric

standard deviation for all samples; neither is observed in measurements, further suggesting that nanoparticle-protein binding is a reversible process best described by a Langmuir-like binding model. Additionally, the condensation-like model is not qualitative agreement with the changes size distribution function observed for nominally 20 nm GNPs, suggesting that a more detailed aggregation model, considering conjugate-conjugate binding, is needed for this sample.

3.4 Conclusions

Electrospray ionization and electrospray based aerosolization techniques have arguably been the most important development in biomolecular and macromolecular analysis in the past several decades, enabling mass spectrometery, and more recently, ion mobility spectrometry of biomolecular complexes.[174] However, despite initial success in analyzing nanoparticle-protein complexes through electrospray based aerosolization [93, 94, 97], the intrinsic requirements of electrospray solutions, including proper electrical conductivity and low non-volatile solute content are simply incompatible with the suspension requirements for many nanoparticle-protein conjugate analyses (i.e. non-volatile solutes required for nanoparticle stability and/or high salt content to mimic biological conditions). Here, we have demonstrated that liquid nebulization with online ultra-high purity water dilution can be used in lieu of electrosprays to aerosolize nanoparticle-protein complexes, facilitating their examination via ion mobility spectrometry. We further show that via integrating across complete size distribution functions inferred in IMS measurement, relatively polydisperse samples can be examined, as shift in mobility equivalent size of the order 1-2 nm can be examined. Surface coverage

parameters inferred from LN-IMS measurements are further shown to be in excellent agreement with parameters inferred from quartz crystal microbalance measurements. Moving forward, we suggest that LN-IMS measurements are a viable alternative to dynamic light scattering, and as prior work has shown that LN-IMS measurements can be made in higher salt concentration suspensions [162], LN-IMS analysis will find utility as a method to study nanoparticle-protein conjugate formation. Future coupling of LN-IMS with aerosol particle mass analysis [93] and/or inductively coupled plasma mass spectrometry [103] should also enable more detailed characterization of nanoparticle-protein conjugates.

Chapter 4

Quantification of Surface Coating Dependent Binding of Serum Albumin to Superparamagnetic Iron Oxide Nanoparticles

Summary

Ultimately the transport and behavior of nanoparticles within a biological system are governed by nanoparticle interactions with biomolecules, most notably proteins. Protein binding and protein induced nanoparticle aggregation are known to occur for a variety of nanomaterials, with the extent of binding and extent of aggregation highly on nanoparticle surface properties. However, often lacking are techniques which enable quantification of the extent of protein binding and aggregation, particularly for nanoparticles below 30 nm in diameter and with polydisperse size distribution function. In this study we adapt ion mobility spectrometry (IMS) to examine the binding of bovine serum albumin to commercially available, anionic surfactant coated superparagnetic iron oxide nanoparticles (SPIONs) which are initially ~21 nm in mean diameter and with a polydisperse size distribution function (geometric standard deviation near 1.4). IMS, carried out with a hydrosol-to-aerosol converting nebulizer coupled with a differential mobility analyzer and condensation particle counter, enables inference of SPION size distribution functions for varying BSA:SPION number concentration ratio. IMS measurements suggests that initially (BSA concentrations below 50 nM), BSA bind reversibly to SPION surfaces, with a binding site density in the 0.04-0.08 nm^{-2} range, similar to that observed previously for 20 nm gold nanoparticles. However, at higher BSA concentrations, BSA induces SPION-SPION aggregation, evidenced by larger shifts in SPION size distribution functions (mean diameters beyond 40 nm for BSA concentrations near 100 nM) and geometric standard deviations (near 1.3) consistent with self-preserving aggregation theories. The onset of BSA induced aggregation is correlated with a modest, but statistically significant decrease in the specific absorption rate (SAR) of SPIONs placed within an alternating magnetic field. Conversely, coating of SPIONs with mesoporous silica (MS-SPIONs) as well as PEGylation (MS-SPIONs-PEG) is found to completely hinder BSA binding and BSA

induced aggregation; IMS inferred size distribution functions are found insensitive to BSA concentration for MS-SPIONs and MS-SPIONs-PEG. The SARs of MS-SPIONs and MS-SPIONs are additionally found insensitive to BSA concentration, confirming the SAR decrease is linked to BSA induced aggregation. Our measurements suggest that IMS has potential as a general technique to quantify protein binding and protein induced aggregation of nanomaterials.

4.1 Introduction

Superparamagnetic iron oxide nanoparticles (SPIONs), which become magnetized in the presence of an external magnetic field,[175-177] have utility in a number of potential *in vitro* and *in vivo* applications. Most notably, SPIONs can be used as MRI contrast agents, [178-184] in drug delivery,[179, 185, 186] cell labeling[187, 188] and sorting,[189] in thermal therapies,[190-193] and for reheating cryopreserved tissues.[194] The latter two applications hinge upon the ability of SPIONs to generate heat when placed within an external alternating magnetic field. The amount of heat generated is quantified as the specific absorption rate (SAR, in W/g Fe), i.e. the heat generation rate per unit mass of iron (for a prescribed magnetic field strength and frequency).[195, 196] SAR values in excess of 200 W/g Fe have been reported under clinically achievable conditions with commercially available SPIONs; with proper loading of SPIONs into biological systems this level of heating would enable SPION-based thermal therapies and reheating applications in many instances.[197]

However, as with other engineered nanomaterials, the loading of SPIONs into biological systems and their eventual fate hinges heavily on the particle surface chemistry and interactions with surrounding molecules.[149, 150, 152-154, 198, 199] Cellular uptake

and transport of nanoparticles is governed largely by the formation of protein corona on nanoparticle surfaces; the particular proteins associated with this corona depend upon the nanoparticle size and surface properties.[200, 201] In addition, the binding of proteins to nanoparticle surfaces can promote nanoparticle aggregation under conditions where nanoparticles would otherwise remain stable in suspension.[202-205] For SPIONs, understanding and control of aggregation has been found to be critically important.[198] A number of studies reveal that protein induced (as well as salt-induced) aggregation leads to a reduction with SAR,[193, 206-209] with recent work suggesting that the formation of superaggregates (composed of more than 10^3 primary SPIONs) reducing SAR values to below 50 W/g Fe (for the same magnetic field conditions where 200 W/g Fe was achieved).[210]

It is therefore necessary to examine protein corona formation on SPIONs as well as the onset of protein-induced SPION aggregation.[211] Doing so requires measurement of the SPION size distribution function and shifts in the size distribution function brought about by protein conjugation and particle-particle aggregation. Regrettably, commonly employed techniques to measure nanoparticle size distribution functions, i.e. dynamic light scattering[40] and nanoparticle tracking analysis,[43, 157] lack both the precision and accuracy necessary to quantify protein conjugation to superparamagnetic particles (with cores smaller than 20 nm in diameter) and to measure polydisperse particles size distribution functions (i.e. distribution functions with geometric standard deviations in excess of 1.3). Aggregation is also difficult to quantify with these techniques, as aggregates have complex and temporally evolving morphologies under most conditions.[212, 213] Difficulties in measurement led to a largely trial-and-error approach to developing surface

coatings for SPIONs to prevent protein induced aggregation, with coatings chosen from a limited number of materials (e.g. silica, polyethylene glycol, dextran). Though several successful surface coating and functionalization strategies have been developed in this manner,[209, 214-218] future efforts would be aided by standardization of protein binding and aggregation characterization methods.

In this study, we make use of recent developments in ion mobility spectrometry (IMS) to quantify the extent of binding of bovine serum albumin (BSA) to commercially available SPIONs as well as the extent of BSA induced aggregation. This is compared and contrasted with measurements of protein binding to the same SPIONs coated with mesoporous silica[202, 219-221] (MS-SPIONs) and coated with mesoporous silica and functionalized with silane and polyethylene glycol (MS-SPIONs-PEG).[209] In engaging in these measurements, our purpose is two-fold. First, we demonstrate a relatively new analysis approach for nanoparticle characterization in biological systems; we show that IMS, which has been predominantly applied to study multiprotein complex structures[174, 222] as well as clusters/nanoparticles formed in atmospheric nucleation,[223, 224] can be used to quantify protein binding and protein induced aggregation for polydisperse nanoparticles in the sub-30 nm size range. We compare IMS measurements to results of nanoparticle tracking analysis, for which characterization of sub-30 nm particles is difficult. Second, we show quantitatively what has been suspected in prior studies,[209] that the onset of both protein binding to SPIONs and SPION aggregation is prevented by mesoporous silica coating, and remains hindered following PEGylation. The sections that follow describe the preparation of materials and measurement methods applied, as well as quantitative analysis of protein binding and aggregation. We note that although the

presented analysis applies to for a specific protein bound to a specific type of nanoparticle, the developed methods are sufficiently general for application to other nanoparticle surface chemistry, as well as complex ligand mixtures (e.g. blood plasma).

4.2 Materials and methods

4.2.1 Sample preparation

EMG 308 suspensions of superparamagnetic magnetite (Fe_3O_4) nanoparticles (SPIONs) were purchased from Ferrotec (USA) Corporation (Bedford, NH). The core particles have a manufacturer reported average diameter ± standard deviation 10 ± 2.5 nm; however, SPIONs are stabilized in suspension by the manufacturer via an anionic surfactant, with the resulting particles physically larger than the core size. It is this anionic surfactant which larger governs the interaction between bare SPIONs and their surroundings. Bovine serum albumin (BSA) was purchased from Sigma Aldrich (Saint Louis, MO, USA), and BSA solutions were prepared by dispersing BSA powder in deionized water (obtained with a SpectraPure filtration system). Diluted EMG 308 suspensions (with nominal number concentrations of 1.5×10^{12} particles ml^{-1}) were mixed with BSA suspensions in 1 mL in polypropylene centrifuge tubes. Seven SPION-BSA mixture samples were prepared with different BSA: SPION number concentration ratios ranging from 3.0 to 80.0. For each sample, SPION-BSA mixture samples were allowed to interact for more than 16 hours in an incubator (Alkali Scientific, FL, USA) at 38.0° C.

Mesoporous silica coated SPIONs (MS-SPIONs) with and without polyethylene glycol (PEG) - Chlorotrimethylsilane (TMS) were also synthesized (as described in the supplemental information and based on the methods provided by Hurley et al[209]).

Suspensions of MS-SPIONs with BSA were made with BSA:SPION ratios up to 260. Mixtures of MS-SPIONs and BSAs were also incubated at 38.0^{o} C for more than 16 hours before the measurements.

4.2.2 Synthesis of mesoporous silica coated iron oxide nanoparticles

For synthesis, the following chemicals were utilized: tetraethylorthosilicate (TEOS, 98%), hexadecyltrimethylammonium bromide (CTAB, 99%), polyvinylpyrrolidone (PVP-10, average molecular weight 10,000) were purchased from Sigma Aldrich. Ethanol (99%) was purchased from Decon Labs, Inc. Ammonium hydroxide (NH_4OH, 28%) was obtained from Macron Fine Chemicals. Milipore water generated by Milli-Q water purification system was used in all the experiments. 2 - [methoxy (polyethyleneoxy) - propyl] 9 - 12-trimethoxysilane (PEG-silane, molecular weight 596-725 g/mol, 9-12 EO) was obtained from Gelest, Inc. (Morrisville, PA). Chlorotrimethylsilane (TMS, >99%) was purchased from Fluka. Ammonium nitrate (NH_4NO_3) was purchased from Mallinckrodt Chemicals (Phillipsburg, NJ).

The synthesis of MS-SPIONs was modified from the procedure which was reported by Hurley et al.[209] First PVP-10 was coated onto SPIONs by sonication (probe sonicator, Cole Parmer Ultrasonic Processor). CTAB was added to the suspension while sonicating to form a layer of surfactant micelles on the surface of the nanoparticles. The suspension was then placed in an oil bath at 50 ℃. After temperature equilibration, 28% NH_4OH was added to the mixture to raise the pH above 7. Ethanolic TEOS (0.88 M) was added dropwise to form the mesoporous silica shell. The bare MS-SPIONs were synthesized by continuous stirring for 2 hours. The co-modified MS-SPION-PEG particles were prepared by adding

PEG-silane to the reaction after stirring with TEOS for 1 hour. After an additional 30 min of stirring, TMS was added. The suspension was mixed for additional 30 min after TMS addition, then transferred to a beaker and allowed to age at 50℃ for 20 h. This aging period permitted silica condensation and water evaporation for easier suspension workup. All samples underwent deoxygenated hydrothermal treatment and were purified via a series of centrifugation steps as described in previous work.[209] A FEI Tecnai T12 microscope (FEI, Inc., Hillsboro, OR) operating at 120 kV and room temperature (24^{o}C) was used to image MS-SPIONs and MS-SPIONs-PEG, with selected images displayed in Figure 4.1.

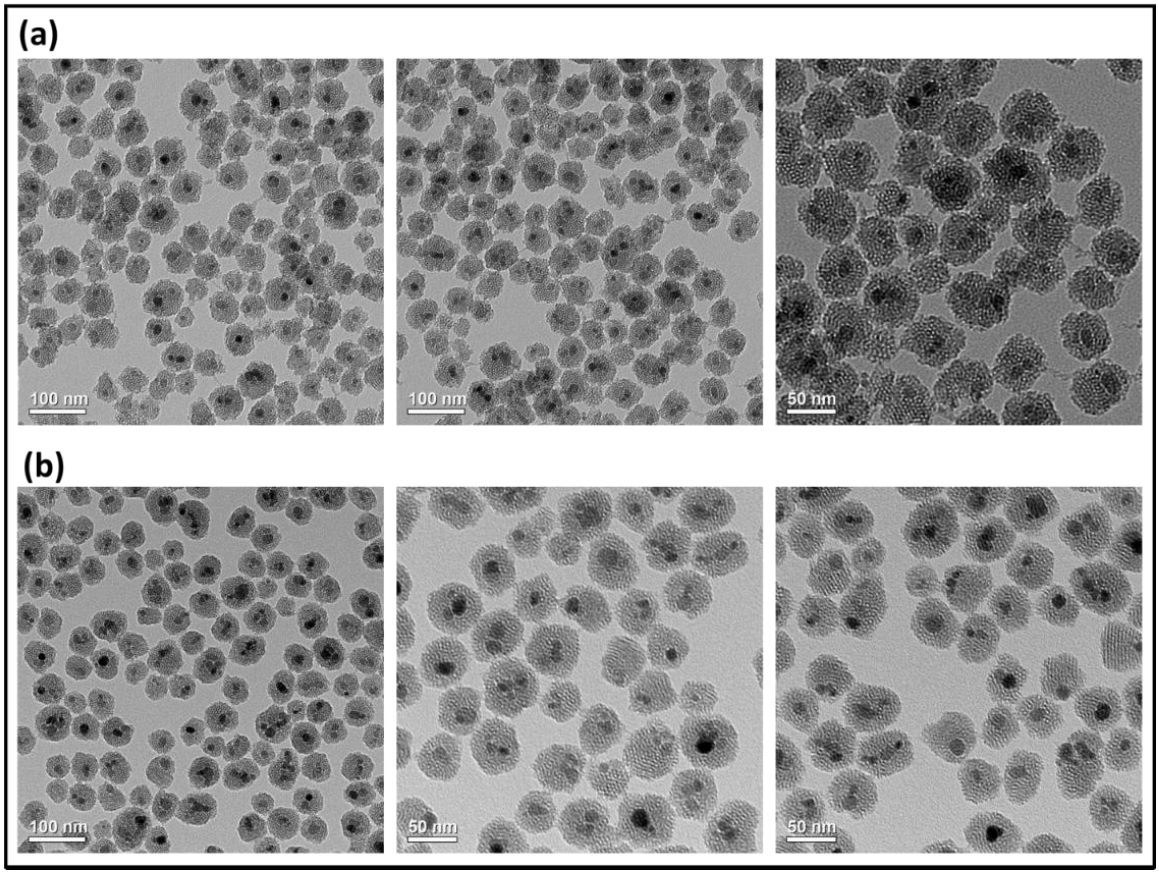

Figure 4.1. Transmission electron micrographs of **(a)** MS-SPIONs and **(b)** MS-SPIONs-PEG.

4.2.3 Liquid Nebulization-Ion Mobility Spectrometry

While prior applications of IMS to nanoparticle analysis have largely utilized electrospray ionization to convert liquid colloids to aerosols,[93, 97, 99, 100] we find that the solution requirements for electrosprays (electrical conductivity in a narrowly defined range, lack of non-volatile surfactant molecules)[89, 91] are not compatible with the suspension conditions needed to analyze protein binding and protein induced aggregation for most nanoparticle types,[225] including SPIONs. Instead, we employed a recently developed, small droplet generating nebulizer with online, high flowrate dilution for aerosolization[162]. This nebulizer ((LiquiTrak® Model 7788, Kanomax Fluid Measurement Technologies, Inc., St Paul, MN, USA) has been shown previously to preserve the size distribution function of nanoparticles, nanoparticle aggregates, and protein-nanoparticle conjugates during the hydrosol to aerosol transition.[225] A schematic and detailed description of its operation can be found in the supplemental information in Chapter 2. As previously described, the main features of the nebulizer, which make it uniquely well suited for nanoparticle analysis, are that (1) it continuously generates submicrometer diameter droplets (lognormally distributed, with a geometric mean diameter of ~100 nm and a geometric standard deviation of 2.3) and (2) it enables online (and relatively rapid) high flowrate dilution (by factors up to $5x10^3$) with ultra-high purity water (UPW, which contains total organic carbon and non-volatile residues below 1ppbv after treating with 165nm UV light, 10 nm and 20 nm particle filtration systems as well as a mixed bed ion exchange resin). By tuning the dilution factor applied and noting that the number of nanoparticles per droplet is Poisson distributed,[135, 137] nebulization conditions can be tuned such that most generated droplets are devoid of particles and non-

volatile residue, and droplets containing nanoparticles do not contain multiple particles (unless the particles aggregated prior to nebulization). Therefore, upon drying droplets, the remaining aerosol particle size distribution function reflects the particle size distribution function in liquid suspension.[162, 225]

For aerosolization, UPW water dilution factors (UPW flowrate/ sample flow rate) from 800 to 3500 were applied to prevent non-specific aggregation during the aerosolization process. Hydrosol to aerosol converted particles were analyzed via ion mobility spectrometry using a differential mobility analyzer (both models 3081 and 3085, TSI Inc., Shoreview MN, were applied in measurements) coupled to butanol based condensation particle counter (model 3775, TSI Inc). These instruments were operated in scanning mode,[125] in which the mobility diameter based size distribution function ($dn/dlog_{10}(d_p)$ the gas phase number concentration of particles per unit log_{10} diameter change) were inverted in the diameter range of 4.0 nm to 151 nm. Details on this data inversion approach are described previously.[162] Free BSA molecules in each suspension were also examined via IMS to infer unbound BSA concentrations. Unbound BSA concentration values were determined using a calibration curve relating the measured aerosol concentrations to liquid suspension concentrations; this was established using the method provided Jeon et al.[162] Size shifts of SPION-BSA conjugates with increasing BSA:SPION ratios were examined as a function of unbound BSA concentrations. Measurements were completed in triplicate (in three separate instances, with more than 10 IMS scans per sample) because of the known sensitivity of aggregate formation to time.

4.2.4 Nanoparticle Tracking Analysis & Specific Absorption Rate Measurements

Size distribution functions of three SPION-BSA samples (BSA:SPION ratios of 3.9, 38.7 and 77.4), incubated for 16 hours at 38 ^{o}C, were examined with Nanoparticle tracking analysis (NTA).[43] These measurements were carried out with a Nanosight^{TM} LM14 (Malvern Instruments LTD, Malvern, Worcestershire, UK). The hydrodynamic diameter based size distribution functions in the 10 nm to 1 μm range for all samples were inferred using the procedure described in Jeon et al. Measurements were performed at least 10 times for each sample, and with extracted hydrodynamic sizes of all tracked individual aggregates of each measurement, an average hydrodynamic distribution function was established by the procedure described in Jeon et al.[226]

The specific absorption rates (SARs) of suspensions of BSA with SPIONs and with MS-SPIONs were also examined. The SAR measurement procedure is described previously.[206] Briefly, a 1kW Hotspot inductive heating system (Ambrell Corporation, Scottsville, NY) was used to generate an alternating magnetic field at 20.0 kA/m field strength and 190 ± 10 % kHz fixed frequency. The temperature change of a 1.0 mL sample in a 1.5 mL centrifuge tube was monitored with a Luxtron 3100 fluoroptic thermometry system (Luxtron Inc., Santa Clara, CA) for 180 seconds. The maximum slope of the temperature versus time curve for 15 ~ 20 seconds within the initial minute of heating was calculated; the SAR was estimated from this slope. At least four SAR measurements were performed for each BSA:SPION ratio.

4.3 Result and discussion

4.3.1 Bare SPION –BSA Conjugation

IMS inferred size distribution functions, which depend on the gas phase mobility equivalent diameter, are displayed in Figure 4.2 for SPIONs (without silica and PEG coating) for variable BSA:SPION number concentration ratios. In classical models of particle aggregation (i.e. diffusion limited cluster aggregation and reaction limited cluster aggregation),[213] aggregation is an irreversible process in which the particle size distribution function evolves continuously over time,[227] with the rate of evolution increasing as aggregates grow if particles are attracted to one another.[228] For this reason, aggregation experiments can exhibit large trial-to-trial variation in measured size distributions.[212] We hence elect to plot results from three distinct experimental sets separately, but note that each displayed is the result of more than ten consecutively measured ion mobility spectra. In spite of the noted issues with temporal evolution in aggregating systems, we find good qualitative agreement between the triplicate measurements. Although BSA-SPION suspensions were incubated for similar times, the observed agreement suggests that in contrast with irreversible aggregation models, SPION-BSA conjugates and aggregates of conjugates exist in equilibrium, such that size distribution functions achieve a time-independent form (for a given BSA:SPION ratio). In addition to the similar shapes of distribution functions between trials, apparent in figure is that the bare SPION size distribution function has a mode diameter near ~21 nm, which is larger than TEM-inferred primary SPION diameter (~15 nm), suggesting that many SPION initially are incorporated into small but stable aggregates (with fewer than 10 primary particles per aggregate). The peak on the left of each distribution function is attributable

to free BSA, and is peaked at 6.3 nm (and is larger in magnitude than the SPION peak, as BSA was present in suspensions in larger number concentrations).

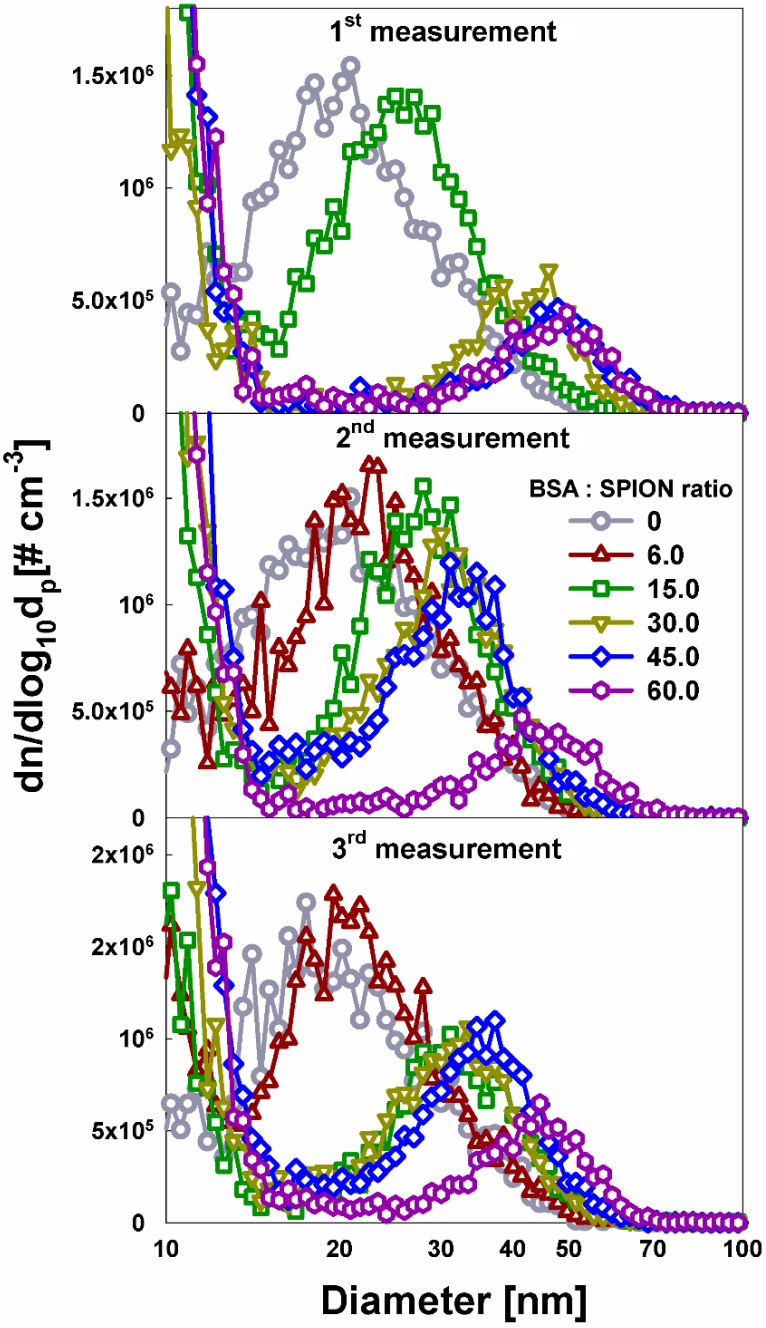

Figure 4.2. IMS inferred size distribution function ($dn/d\log_{10}(d_p)$, in units of cm^{-3}) for SPIONs in aqueous suspension with variable added BSA:SPION ratios. Measurements were repeated in triplicate (three separate samples per condition with more than ten IMS spectra averaged for each curve).

Increasing BSA:SPION number concentration is found to continuously shift size distribution functions to larger sizes while decreasing the magnitude of mode. The size shifts observed, which are in excess of 10 nm, are significantly larger than those observed in recent experiments wherein IMS was used to examine BSA binding to 30 nm and 50 nm gold nanoparticles in Chapter 3. Gold nanoparticles were found to remain unaggregated during such experiments, and the difference in size shift observed here may be attributable to BSA-facilitated aggregation of SPIONs.

More rigorously, the influence of BSA on SPION size distribution functions can be examined via calculation of the mean diameter ($d_{p,ave}$), volumetric concentration (V_{tot}), and geometric standard deviation for each size distribution (σ_g), which quantify the average SPION aggregate size, total particulate amount in suspension, and the suspension polydispersity, respectively. These parameters are calculated via the equations (as noted in Chapter 3):

$$d_{p,ave} = \frac{\int_{-\infty}^{\infty} \frac{dn}{dlog_{10}d_p} d_p dlog_{10}d_p}{\int_{-\infty}^{\infty} \frac{dn}{dlog_{10}d_p} dlog_{10}d_p} \tag{4.1a}$$

$$V_{tot} = \frac{\pi}{6} \int_{-\infty}^{\infty} \frac{dn}{dlog_{10}d_p} {d_p}^3 dlog_{10}d_p \tag{4.1b}$$

$$\sigma_g = exp\left(\sqrt{\frac{\int_{-\infty}^{\infty} \frac{dn}{dlog_{10}d_p} ln^2\left(\frac{d_p}{d_{p,g}}\right) dlog_{10}d_p}{\int_{-\infty}^{\infty} \frac{dn}{dlog_{10}d_p} dlog_{10}d_p}} \right) \tag{4.1c}$$

$$d_{p,g} = \exp\left(\frac{\int_{-\infty}^{\infty} \frac{dn}{dlog_{10}d_p} ln(d_p) dlog_{10}d_p}{\int_{-\infty}^{\infty} \frac{dn}{dlog_{10}d_p} dlog_{10}d_p} \right) \tag{4.1d}$$

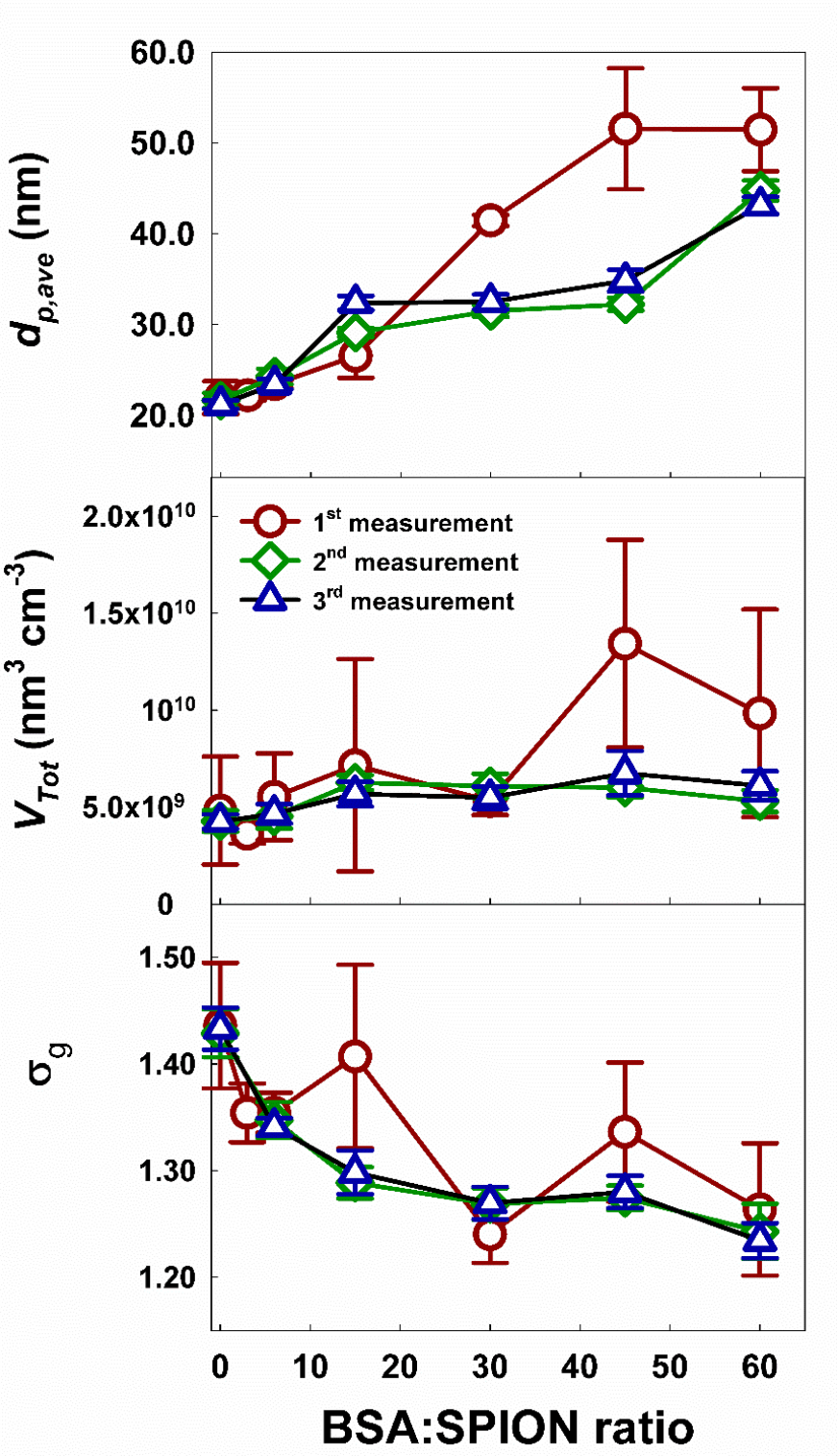

Figure 4.3. A summary of the average mobility diameter, cumulative volume concentration, and geometric standard deviation of the size distribution functions of BSA-SPION conjugates as a function of the BSA:SPION ratio.

By examining the evolution of $d_{p,ave}$, V_{tot}, and σ_g with increasing BSA:SPION number concentration ratio, the mechanisms driving SPION size distribution function shifts can be inferred. For example, if size distribution function evolution occurs only because of BSA reversible binding at specific sites on SPION surfaces (i.e. Langmuir-like adsorption), $d_{p,ave}$ will first increase, but asymptote once complete surface coverage is achieved, V_{tot} will increase modestly as proteins are incorporated into particles, and σ_g of originally polydisperse particles (such as the examined SPIONs) will modestly but monotonically decrease (until maximum surface coverage). Conversely, if size distribution evolution occurs solely by aggregation, $d_{p,ave}$ will increase continuously, V_{tot} will remain constant, and σ_g will evolve to a near-constant value in the 1.3-1.4 range.[229] Plots of these three parameters are provided in Figure 4.3, with errors bars representing the standard deviation between individual IMS spectra. Consistent with the size distribution functions themselves, little variation is observed between measurements under the same conditions, with the exception of a single trial with BSA:SPION = 45, for which the average diameter and volumetric concentration are both anomalously large. Disregarding this measurement, there appear to be two regimes for size distribution function evolution. For BSA:SPION ≤ 30, $d_{p,ave}$ increases are modest (< 10 nm), V_{tot} remains nearly constant, and σ_g decreases sharply (from above 1.4 to close to 1.3). Beyond BSA:SPION = 30, $d_{p,ave}$ increases are more pronounced (> 20 nm increase from the bare SPION value), and both V_{tot} and σ_g remain close to constant. Combined, these suggest that first, reversible BSA conjugation to SPION surfaces occurs, and BSA-SPION complexes are then able to aggregate with one another, i.e. BSA can act to binds SPIONs to one another once they are present on SPION surface. As isoelectric point of BSA is ~4.7 and SPIONs are coated with an anionic

surfactant, it does not appear that BSA binding to SPIONs is governed by electrostatics; conjugation is more plausibly driven by the interaction of hydrophobic regions of BSA with SPION surfaces. However, further investigation is required to more clearly identify the mechanism by which BSA attaches to SPION, at the amino acid level.

Determination of the unbound BSA concentration via IMS reveals that the reversible BSA conjugation regime applies for BSA concentration range below 3 x 10^{13} mL^{-1} (below ~50 nM); the onset of SPION aggregation occurs above this concentration. As in prior IMS investigations in Chapter 3 and Tsai et al[97, 225] of BSA binding to nanomaterials, results for reversible conjugation can be compared to a Langmuir-like, equilibrium adsorption model, which is a two-parameter fit to the $d_{p,ave}$ versus unbound BSA concentration curve. This model, based upon models of subsaturated vapor uptake by gas phase ions,[167, 169] is described in detail in Chapter 3 and is expressed with the equations again here:

$$d_{p,ave} = \frac{\int_{-\infty}^{\infty} \frac{dn}{dlog_{10}d_{p,0}}\Big|_0 (\sum_{i=0}^{\infty} d_{p,i}P_i) dlog_{10}d_{p,0}}{\int_{-\infty}^{\infty} \frac{dn}{dlog_{10}d_{p,0}}\Big|_0 dlog_{10}d_{p,0}} \quad (4.2a)$$

where $\frac{dn}{dlog_{10}d_{p,0}}\Big|_0$ is the bare SPION size distribution function in the absence of BSA (taken directly from experiments) and $d_{p,i}$ is the volume equivalent diameter of a SPION ($d_{p,0}$) with i BSAs (d_{pro} = 6.31 nm; $d_{p,i} = \left(d_{p,0}^3 + i d_{pro}^3\right)^{1/3}$). P_i is the probability that a SPION has i BSAs attached on its surface:

$$P_0 = \frac{1.0}{1.0 + \sum_{k=1}^{k=[X]\pi d_{p,0}^2} \left(\left(\frac{n_a}{n_{eff}}\right)^k \prod_{j=1}^{j=k} \left(\frac{\left[[X]\pi d_{p,0}^2 - j + 1\right]}{j} \right) \right)} \quad (4.2b)$$

$$P_i = \frac{\left(\frac{n_a}{n_{eff}}\right)^i \prod_{j=1}^{i}\left(\frac{\left\lfloor [X]\pi d_{p,0}^2 - j + 1 \right\rfloor}{j}\right)}{1.0 + \sum_{k=1}^{k=[X]\pi d_{p,0}^2}\left(\left(\frac{n_a}{n_{eff}}\right)^k \prod_{j=1}^{j=k}\left(\frac{\left\lfloor [X]\pi d_{p,0}^2 - j + 1 \right\rfloor}{j}\right)\right)} \qquad i \geq 1 \qquad (4.2c)$$

where n_a is the unbound BSA concentration in aqueous suspension, *[X]* is the surface binding site density (modeling all bare SPIONs as spheres with diameter independent *[X]*), and n_{eff} is the effective BSA concentration above a binding site. The latter two parameters are fit to IMS measurements, with results shown in Figure 4.4. Though only 3-4 data points are applied for each fit, comparison of measurements to equation (2a-c) allow us to estimate both the BSA binding site density on SPIONs as well as the effective BSA concentration above a site to within an order or magnitude. All measurements are consistent with *[X]* = 0.04 – 0.08 nm^{-2} and n_{eff} of order 10^{11} –10^{12} mL^{-1}. We can also compare estimates of *[X]* and n_{eff} to those made for gold nanoparticle-BSA reversibly bound conjugates in Chapter 3; n_{eff} is found to be similar in magnitude to values obtained for nominally 20 nm, 30 nm, and 50 nm gold particles. Conversely, the estimate of *[X]* for SPIONs is appreciably larger than those inferred for 30 nm and 50 nm gold particles (binding site densities of 0.02-0.03 nm^{-2}), but similar to that observed for 20 nm gold particles (with a binding site density of 0.06 nm^{-2}). Noteworthy about this comparison is that like SPIONs, 20 nm gold particles were observed to aggregate in the presence of BSA (though at lower BSA concentrations), while aggregation of larger gold nanoparticles was not observed. This suggests that protein conjugation onto nanoparticles has a greater influence on the size distribution functions and morphologies of small (sub 30 nm diameter) particles irrespective of particle chemical composition, and is consistent with observations made in prior work.[170, 171]

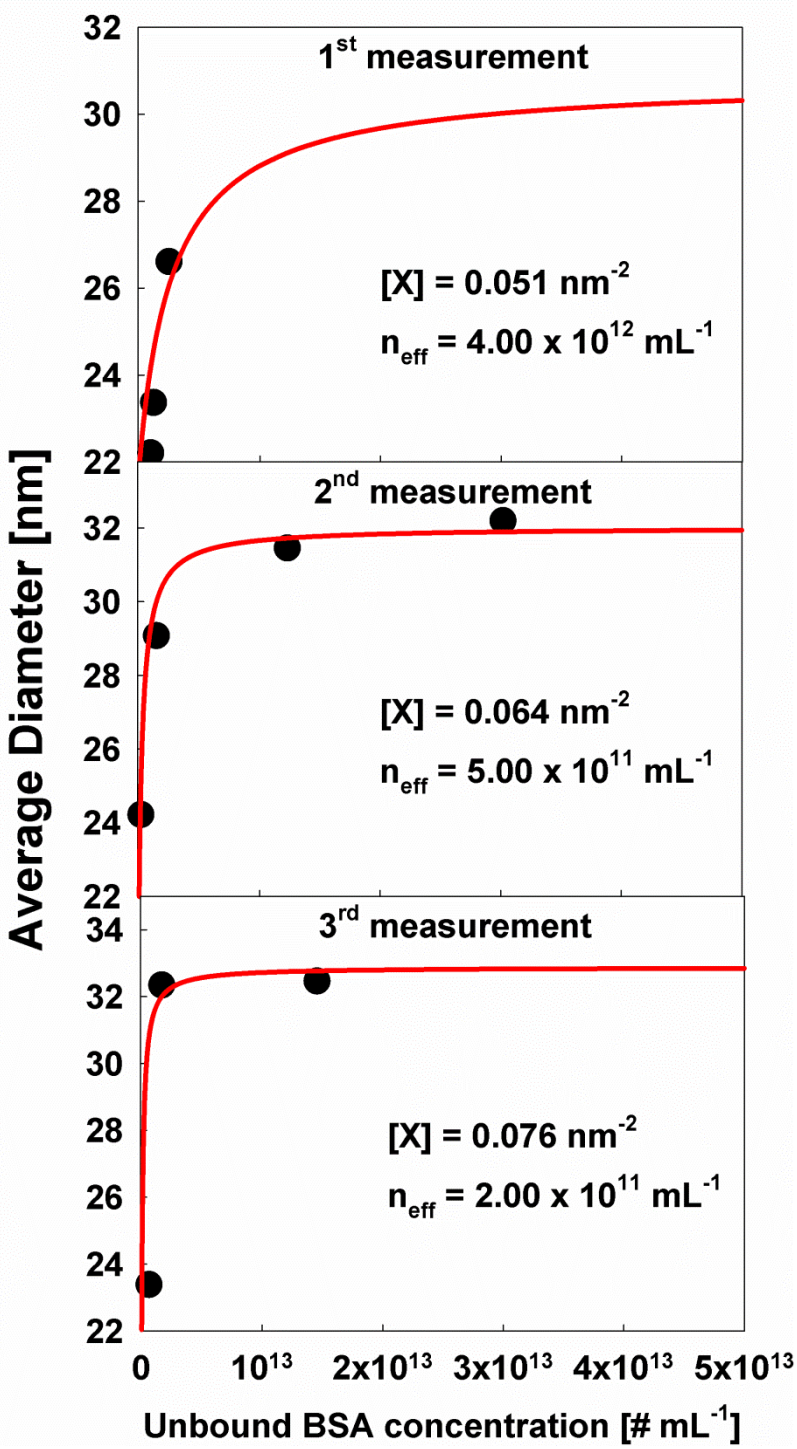

Figure 4.4. A comparison of measured average diameter for BSA-SPION conjugates as functions of IMS measured unbound BSA concentrations to predictions based upon an equilibrium protein conjugation model (i.e. a Langmuir-like adsorption model) where the base SPION size distribution function, effective binding site surface concentration *[X]* and effective BSA concentration above a binding site (n_{eff}) are used as input values. For the displayed curves, *[X]* and n_{eff} are fit to measurements, while the input size distribution functions are used directly from IMS measurements in the absence of BSA.

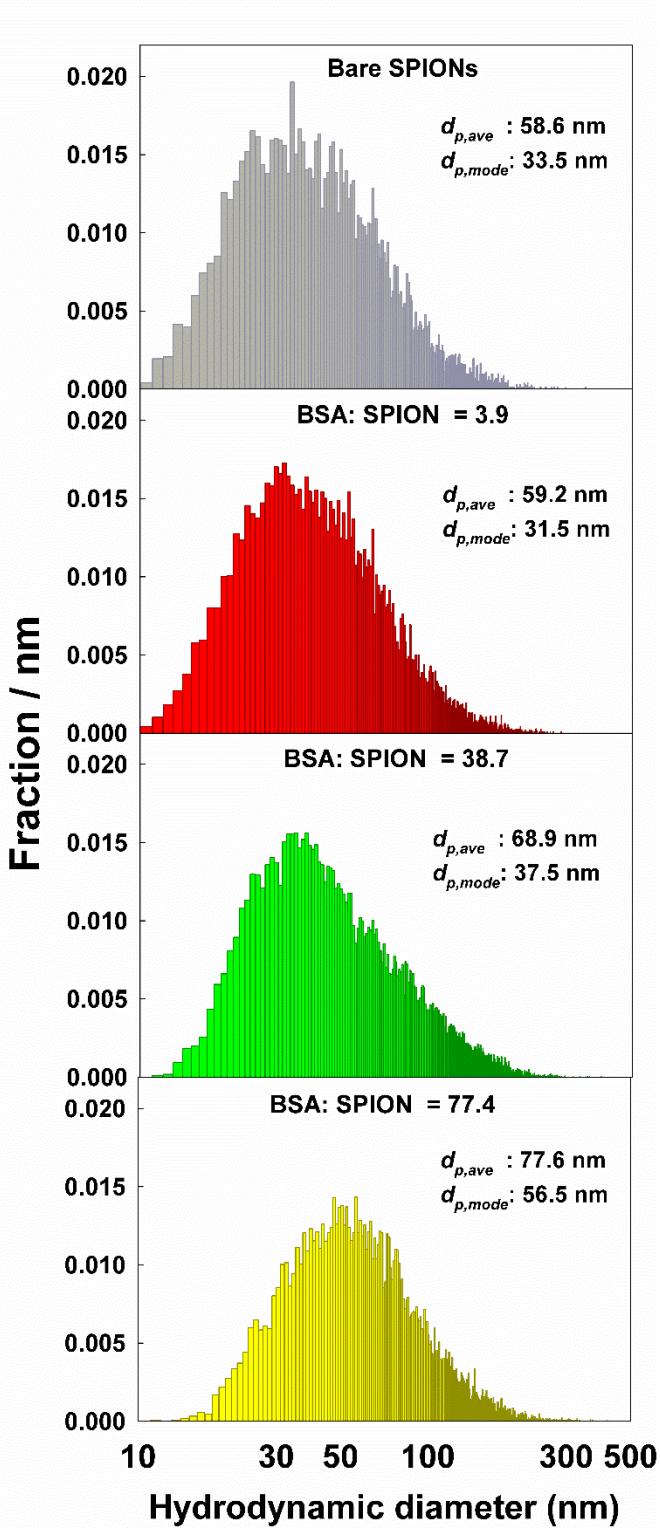

Figure 4.5. Normalized size distribution functions (fraction of particles per nm change in diameter) for BSA:SPION conjugates as inferred via Nanoparticle tracking analysis (NTA). NTA based distribution functions are expressed in terms of the hydrodynamic diameter, which is not equivalent to the IMS inferred mobility diameter in all circumstances.

The observation of initial SPION growth via reversible BSA binding, followed by subsequent BSA facilitated aggregation was made possible by the precision and accuracy of IMS measurements in the sub 30 nm size range. For comparison, Figure 4.5 displays hydrodynamic diameter based size distribution functions for SPIONs with varying BSA:SPION ratio, which were measured by nanoparticle tracking analysis. Evidenced in the plots, both the mean ($d_{p,ave}$) and mode diameter in size distribution functions observed by nanoparticle tracking analysis are larger than that determined with IMS, with mean diameter values significantly larger for similar measurements. Hydrodynamic diameter distribution functions are additionally found to be broader than IMS distributions and have geometric standard deviations in excess of 1.5. While some of these differences are attributable to differences between the gas phase mobility diameter and the hydrodynamic diameter for aggregates,[128] this alone cannot explain the clear differences in distribution function mean diameters and polydispersities. Instead, though nanoparticle tracking analysis can be used to quantify polydisperse aggregate size distribution functions,[77, 210] particles present below 30 nm are difficult to detect via light scattering when larger particles are present as discussed in Chapter 2. This leads to inaccuracies for SPIONs, as many SPION aggregates have effective diameters below 30 nm, but the distribution functions are sufficiently polydisperse for larger particles to be present.

Noted in the introduction, prior studies have shown consistently that salt induced aggregation and protein induced aggregation of SPIONs directly leads to a reduction in SAR.[206, 207, 210, 230] However, protein induced aggregation experiments were performed using fetal bovine serum, in which the BSA concentrations are of the order 10^2 μM; SARs at lower BSA concentrations have not been examined previously. Figure 4.6

plots the SAR (in terms of W per gram of Fe) as a function of BSA:SPION ratio in suspension. Measurements span a free BSA concentration up to 150 nM. Displayed results are the mean values ±standard deviation for 4-6 measurements per sample. A decreasing SAR with increasing BSA concentration is evident, even for such dilute BSA concentrations. Via a Student's t-test, the observed decrease is found to be statistically significant; the SAR for BSA:SPION = 0 differs from the SAR for BSA:SPION = 60 ($p = 0.004$), and SARs for BSA:SPION = 0-15 differ from the SAR for BSA:SPION = 30-60 ($p = 0.017$). This further supports the findings of IMS measurements, that aggregation is preceded initial by BSA conjugation to SPIONs.

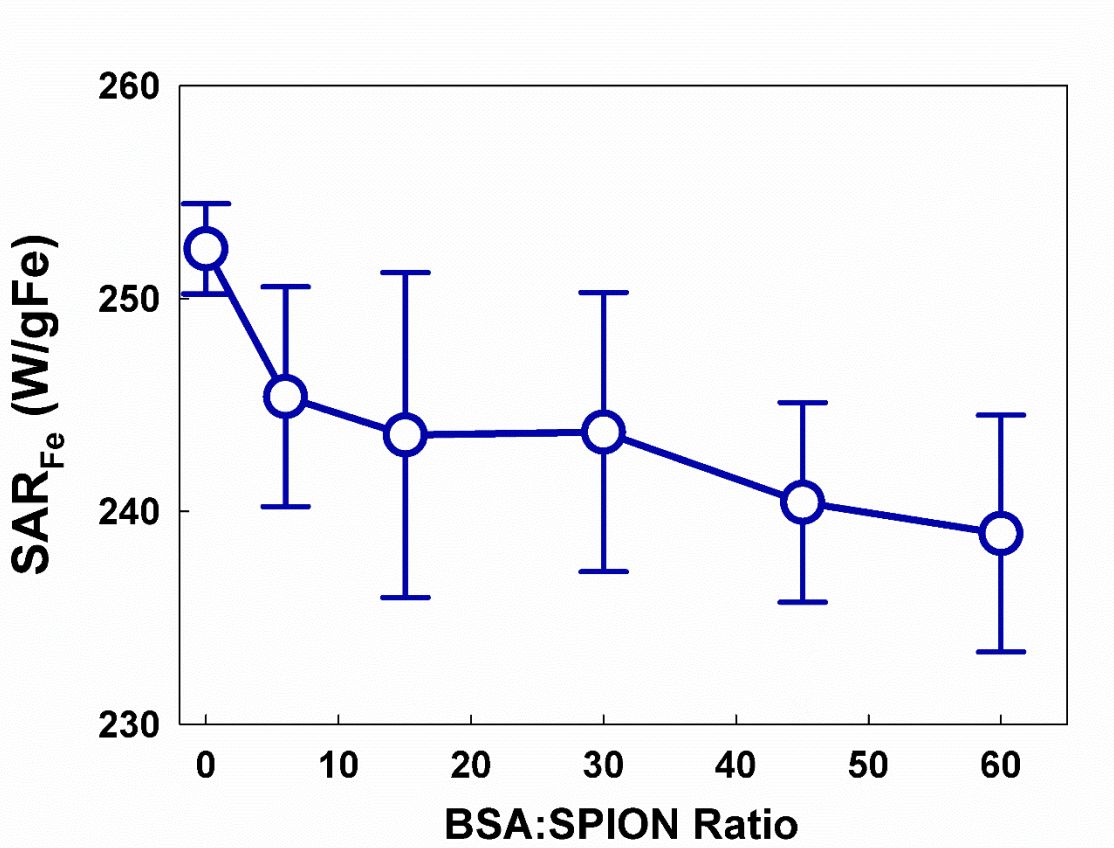

Figure 4.6. The specific absorption rate of BSA:SPION conjugates as function of BSA:SPION number concentration ratio.

4.3.2 MS-SPION &MS-SPION-PEG analysis

The coating of SPIONs with mesoporous silica leads to an appreciable increase in diameter for all SPIONs. Both MS-SPIONs and MS-SPIONs-PEG have feret diameters near 65 nm, and in many instances, multiple SPIONs are incorporated into a single MS-SPION or MS-SPION-PEG (confirming small aggregates exist even in protein free SPION suspensions). Directly comparable to Figure 4.2, IMS inferred size distribution functions at variabla BSA:SPION ratios are provided in Figure 4.7 for both MS-SPIONs and MS-SPIONs-PEG. IMS measurements confirm that MS-SPIONs have effective diameters near 65 nm, and also show that PEGylation brings about a ~1 nm increase in diameter. Further, size distributions functions of both particle types are remarkably consistent in both mean diameter and geometric standard deviation for all examined BSA:SPION ratios. Although the binding of individual BSA molecules cannot be easily detected via IMS on particles larger than 50 nm, and there remains that possibility that BSA may be incorporated into silica pores (which would not shift the diameter), the consistency of the MS-SPION and MS-SPION-PEG size distribution functions most likely arises because BSA does not bind to MS-SPIONs and MS-SPIONs-PEG, which in turn prevents BSA induced aggregation. Combining the results of this study and previous studies of SPION aggregates,[206, 209, 210] it appears that for biologically relevant albumin concentrations, SPIONs without surface treatment would persist as aggregates which are in the submicrometer size range and significantly larger than unaggregated MS-SPIONs.

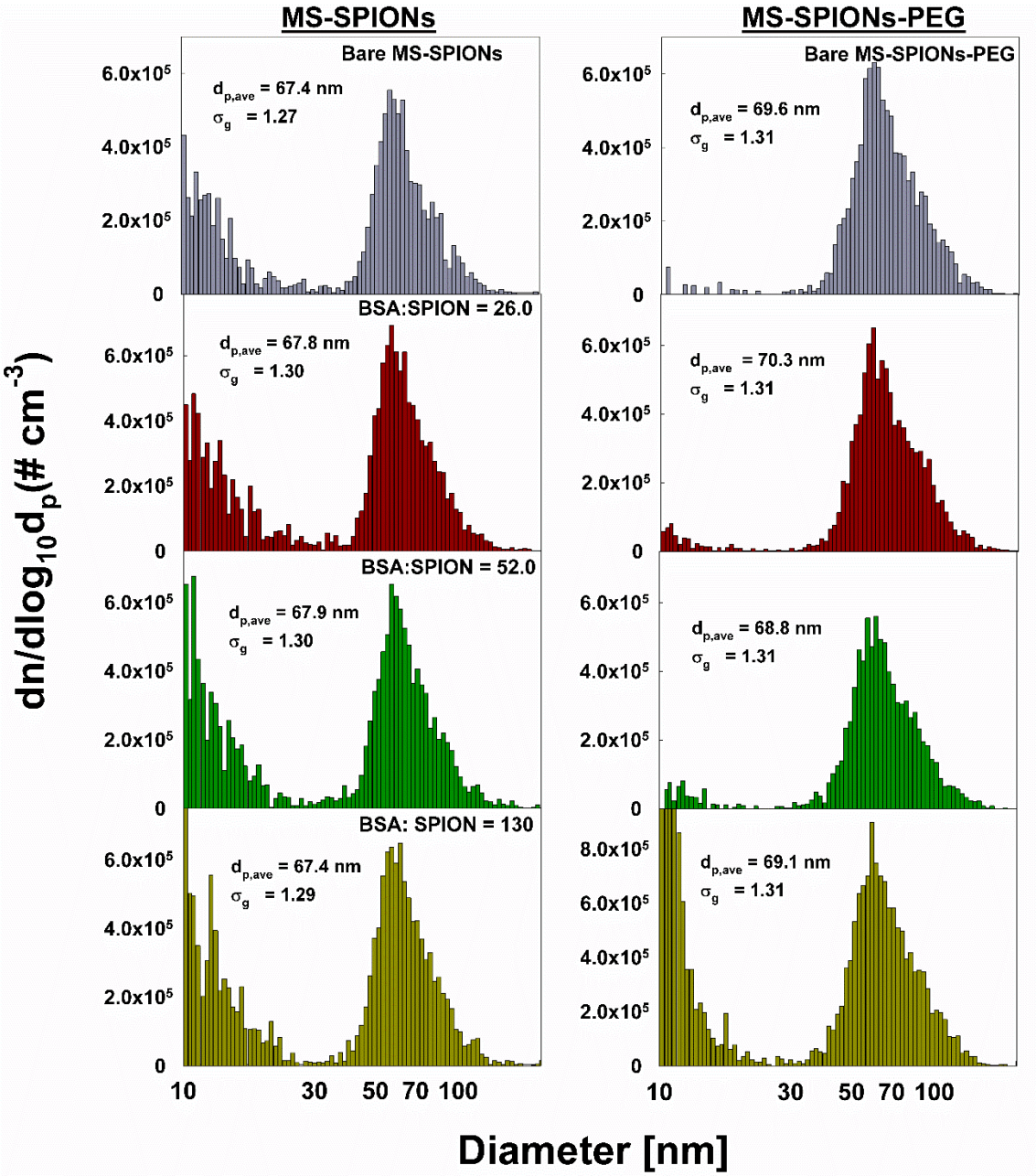

Figure 4.7. IMS inferred size distribution functions ($dn/dlog_{10}d_p$) for MS-SPIONs and MS-SPIONs-PEG at varying BSA:SPION number concentration ratios. Each displayed distribution function is the average of more than 10 ion mobility spectra. Partial peaks in distributions near 10 nm are part of the free BSA size distribution function, which has a mode at 6.3 nm and is much larger in magnitude than the SPION mode value. The geometric mean diameter (d_{pg}) and geometric standard deviation (σ_g) consider the MS-SPION and MS-SPION-PEG portion of each distribution function are noted.

The lack of MS-SPION and MS-SPION-PEG aggregation is also evident in examination of MS-SPION-PEG SARs, which are provided in Figure 4.8. SAR is visually observed to be insensitive to BSA:SPION ratio for MS-SPIONs-PEG, and no statistical differences in measurements or group of measurements are obtained.

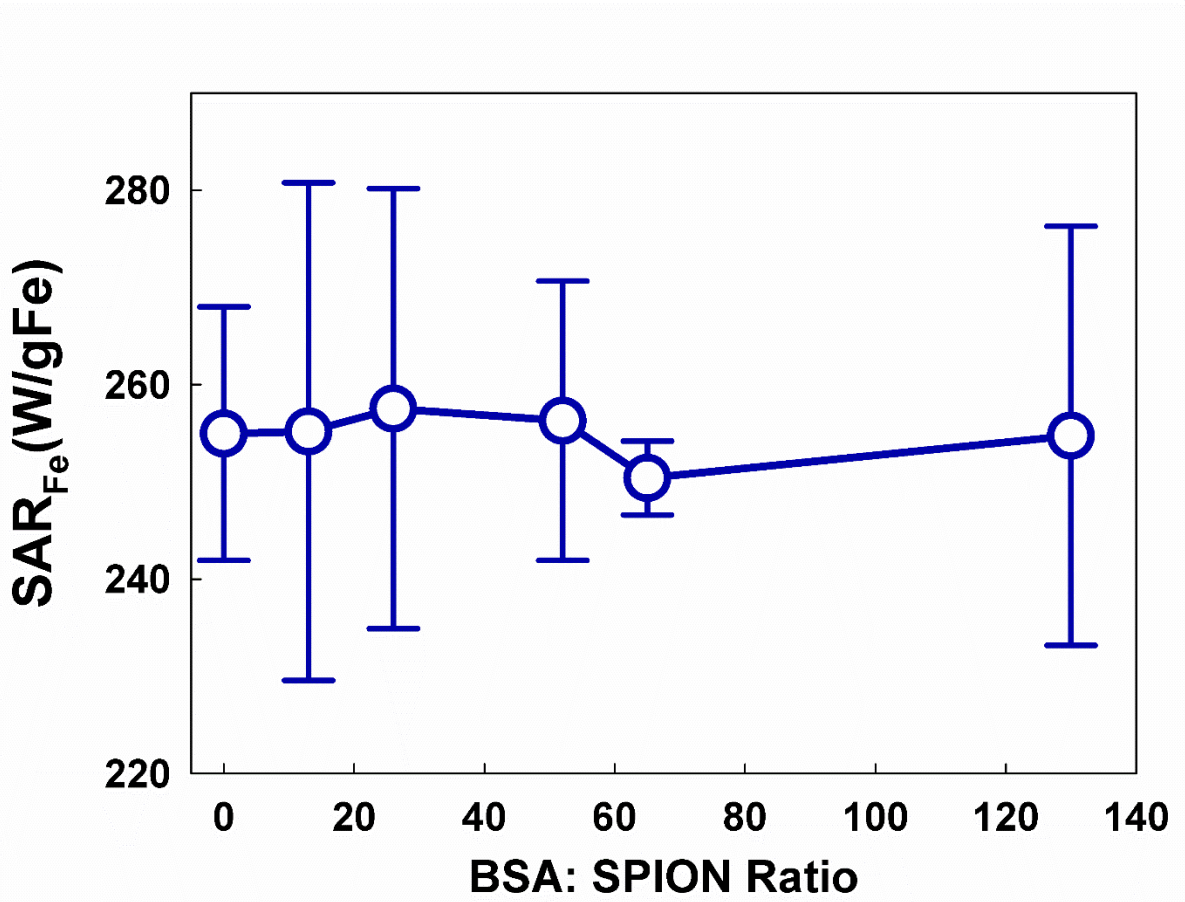

Figure 4.8. The SAR of MS-SPIONs-PEG as a function of BSA:SPION number concentration ration.

4.4 Conclusions

We applied ion mobility spectrometry with a hydrosol-to-aerosol conversion nebulizer[162] to examine the evolutions of the size distribution functions of SPIONs due to both BSA binding and BSA induced SPION aggregation. Measurements were consistent with BSA first binding reversibly to SPION surfaces, and BSA induced aggregation occurring in instances where full surface coverage by BSA was assured. We also showed quantitatively that both BSA binding and BSA aggregation were mitigated by coating SPIONs with mesoporous silica. To our knowledge, this study is also the first to utilize ion mobility spectrometry to examine protein aggregation onto metal oxide nanoparticles; previous studies were limited to proof-of-concept measurements of noble metal nanoparticles and silica. However, because the IMS technique is relatively insensitive to nanoparticle chemical composition and absolute size and does not require analyte specific standards for calibration[162], we propose that it should find application as a screening technique to examine protein binding and protein induced aggregation for a wide variety of nanomaterials. Further IMS measurements along these lines would enable simple comparison between different nanomaterials, suspension conditions (pH and ionic strength), and proteins.

Chapter 5

Quantifying Intra- and Extracellular Aggregation of Iron Oxide Nanoparticles and its Influence on Specific Absorption Rate

Summary

A promising route to cancer treatment is hyperthermia, facilitated by superparamagnetic iron oxide nanoparticles (SPIONs). After exposure to an alternating external magnetic field, SPIONs generate heat, quantified by their specific absorption rate (SAR, in W/g Fe). However, without surface functionalization, commercially available, high SAR SPIONs (EMG 308, Ferrotec, USA) aggregate in aqueous suspensions, leading to reduction in SAR. Further reduction in SAR has been observed for SPIONs in suspensions containing cells, but the origin of this further reduction has not been made clear. Here, we use image analysis methods to quantify the structures of SPION aggregates in the extra- and intracellular milieu of LNCaP cell suspensions. We couple analysis with nanoparticle tracking analysis and SAR measurements of SPION aggregates in cell-free suspensions, to better quantify the influence of cellular uptake has on SPION aggregates and ultimately its influence on SAR. We find that in both the intra- and extracellular milieu, SPION aggregates are well-described by a quasifractal model, with most aggregates having fractal dimensions in the 1.6-2.2 range. Intracellular aggregates are found to be significantly larger than extracellular aggregates and are commonly composed of more than 10^3 primary SPION particles (hence they are "superaggregates"). By using high salt concentrations to generate such superaggregates and measuring the SAR of suspensions, we confirm that it is the formation of superaggregates in the intracellular milieu that negatively impacts SAR, reducing it from above 200 W/g Fe for aggregates composed of fewer than 50 primary particles to below 50 W/g for superaggregates.

5.1 Introduction

Superparamagnetic iron oxide nanoparticles (SPIONs) show promise in a variety of biomedical applications, most notably as contrast agents in magnetic resonance imaging [178-183] and in hyperthermia-based cancer therapy.[175, 196, 231-234] In the latter, tissues loaded with SPIONs are subjected to an external alternating magnetic field,[194, 235, 236] then relaxation of the magnetic moments of the SPIONs after magnetic field exposure (either by the Brownian or Neelian mechanisms)[175-177] leads to the production of thermal energy (heat), thereby increasing the temperature of the SPION-loaded region and promoting necrosis.[191, 192] The extent of heating under prescribed magnetic field conditions is quantified by the specific absorption rate (SAR),[175, 195, 197, 237] the thermal energy production rate per unit mass of iron. Though encouraging results in the level of SAR attainable have been obtained in laboratory-scale studies (SAR above 200 W/g Fe) and reduction in tumor size has been observed via SPION-based hyperthermia,[190, 192, 194, 238-240] a well-documented issue with application of SPIONs is that without additional surface functionalization, commercially available, high SAR SPIONs (EMG 308, Ferrotec, USA) aggregate under biologically relevant suspension conditions, and aggregation leads to a reduction in SAR.[206, 207, 230, 241] Aggregation of such nanomaterials in biologically relevant systems, which are of relatively high ionic strength[31, 242, 243] and contain a wide variety of small molecule solutes and proteins,[204, 206, 212, 244] is by no means unexpected. Increased ionic strength reduces the influence of electrostatic repulsion between particles, and the adsorption of proteins onto nanoparticle surfaces can further induce aggregation. More surprising, however, is that additional reduction in SAR has been found in the presence of living cells, i.e.

suspensions of near identical composition have differences in SAR close to 50%, depending upon whether they contain metabolically active cells.[193, 208] This finding remains unexplained to date.

Though methods have been developed to mitigate SPION aggregation and its influence on SAR,[209, 214-218] it remains necessary to better quantify the extent of SPION aggregation in extra- and intracellular media, the structures of SPION aggregates, and the influence that aggregation has on SAR. Such information would inform future SPION design for biomedical applications. Unfortunately, other than a qualitative description of aggregate formation, little work has been performed to quantitatively characterize SPION aggregation in the cellular milieu. The purpose of this study is hence to develop and apply analysis methods to (1) quantify the structures of SPION aggregates observed in extra- and intracellular environments in suspensions of human prostate cancer cells (lymph node cancer of the prostate, LNCaP-Pro5), (2) develop a functional relationship between SAR and the number of SPIONs per aggregate, and (3) use information from (1) and (2) to predict the SAR of SPIONs contained in the extra- and intracellular milieu. For (1), we apply an image processing method[206, 245] with transmission electron micrographs of LNCaP cells loaded with SPIONs. Aggregates are assumed to be quasifractal[63, 246] in nature; this enables inference of their morphological descriptors via comparison to computationally modeled aggregate structures. For (2) we use a combination of the results of image processing analysis, aggregate population analysis via nanoparticle tracking analysis (NTA)[43, 157, 226], and direct SAR measurements. Finally, for (3) we apply the results of (1) and (2), and compare predictions to observed SAR values in cell suspensions. In total, this study confirms that it is in fact

the aggregation of SPIONs that reduce SAR, and specifically in intracellular environments, the formation of superaggregates (containing more than 10^3 SPIONs) which leads to greatest reduction in SAR for non-functionalized SPIONs.

5.2. Experimental methods

5.2.1 In vitro sample preparation

Aqueous stock solution (EMG 308) of anionic surfactant-coated superparamagnetic magnetite (Fe_3O_4) nanoparticles (SPIONs) was purchased from Ferrotec Corporation (Bedford, NH, USA). This SPION stock has a density of 1.06×10^3 kg/m^3 with a pH of 8-9. The manufacturer reported an average diameter ± standard deviation of SPIONs of 10 ± 2.5 nm, and iron (Fe) mass concentration of SPIONs in the stock solution was 44.1 mg Fe/ml.

Human prostate cancer cells (lymph node cancer of the prostate, LNCaP-Pro5), which have been commonly used in other cancer studies[178, 247], were selected as the SPION target. LNCaP cells were placed in monolayers in 75 cm^2 T-flasks at 37 ℃ and 5% CO_2; they were grown in Dulbecco's Modified Eagle Medium (DMEM F12) with the addition of 10% fetal bovine serum (FBS), 1% penicillin-streptomycin, and 10^{-9} M dihydrotestosterone. When LNCaP cells reached 60-80% confluency, 0.5 mg Fe/ml EMG 308 solution was introduced in the cell culture media, and LNCaP cells were incubated with IONPs for 24 hours. Subsequently, the cells were washed by phenol-red free Hank's balanced salt solution (HBSS) five times to remove excess SPIONs. The cells were then detached from the monolayers by using 2.0 mL of 0.05% trypsin with 0.53 mM EDTA for 6–9 minutes (trypsinization process), and they were pelleted via centrifugation at a relative

centrifugal force (RCF) of 400 for 10 minutes. Finally, the cells were resuspended in fresh media.

5.2.2 Transmission electron microscopy & image analysis

A FEI Tecnai T12 microscope (FEI, Inc., Hillsboro, OR) was used to image SPIONs in intra- and extra- cellular matrices of LNCaP cells. For TEM sample preparation, first, LNCaP cells were washed twice with 0.1 M cacodylate buffer, and subsequently they were exposed to 2.5 M gluteraldehyde in buffer for fixation. After two buffer washes, the cell pellet was stained with 1% osmium tetroxide for 1 hour. The pellet underwent two more buffer washes, after which it was dehydrated in sequentially varied ethanol concentrations (50%, 70%, 80%, 95%, and 100%). Any ethanol remaining in the pellet was rinsed three times with propylene oxide. Next, a 2:1 mixture of propylene oxide:EPON epoxy mix was infiltrated into the pellet for 2 hours (without covering the sample), and then the pellet was infiltrated with a 1:1 mixture of propylene oxide:EPON epoxy mix twice without covering the sample (1 hour each time). Finally, a pure epoxy mix was allowed to infiltrate into the pellet overnight. The next day, the sample was placed in a curing oven at 40 ℃ for 24 hours, then 60 ℃ for 48 hours. The polymerized block was detached from the casing (1 ml centrifuge tube), and it was cured for another 8 hours at 60 ℃ to ensure complete polymerization. The final hardened polymer block was then sectioned into ~ 60 nm slices with a Leica EM UC6 Ultramicrotome (Leica Microsystems Inc., Buffalo Grove, IL), and the slices were deposited on a TEM copper grid (200 mesh, Ted Pella Inc., Redding, CA). TEM imaging was performed at 120kV and room temperature. After taking multiple images in different cellular areas, images were matched

to one another to display nearly complete cells. IONPs in and around five cells were imaged for morphological analysis.

Morphological properties of SPION aggregates were inferred using methods developed and verified by Thajudeen et al[245] and Etheridge et al.[206] First, we calculated four geometric parameters for each aggregate observable in TEM images; (1) the perimeter (P), (2) the maximum extent of the aggregate (L_{max}), (3) the 2D radius of gyration ($R_{g,2D}$) and (4) the 2D projected area (PA). For calculations, TEM images were cropped to isolate individual aggregates (when possible). Aggregate images were loaded into 'ImageJ' (National Institute Health) and converted into bit matrices, wherein the greyscale intensity was given a value from 0 (black) to 255 (white). Aggregates were visually evident as they were found to be significantly darker than all other image features. They could hence be identified by setting greyscale threshold of 250; each matrix value was reassigned a value of "1" if original value was less than 250 and "0" if the original value was 250 or higher. After undergoing this procedure, each image bit matrix only contained non-zero values where aggregates were located, and could then be used to calculate the four aforementioned 2-D properties. Additionally, for each aggregate, primary particle radii were measured directly in 'ImageJ,' and for each aggregate a projected area weighted mean primary particle radius (a_p) was obtained.

Once a TEM image of an SPION aggregate was converted to a bit matrix (aggregate pixel=1.0 and background pixel=0.0), four geometry parameters (P, L_{max}, $R_{g,2D}$ and PA) were calculable. To determine the perimeter (P), the number of unit pixel edges at the boundary of an aggregate image was multiplied by the unit pixel length (L_p), and the maximum extent of the aggregate (L_{max}) was obtained by finding the longest scalar distance

between two pixels within an aggregate image. The 2D radius of gyration ($R_{g,2D}$) and the 2D projected area (PA) were calculated with following equations:

$$R_{g,2D} = \sqrt{\frac{1}{N}\sum_{i=1}^{i=N_{(x,y,\alpha=1)}}(x_i - x_{cm})^2 + (y_i - y_{cm})^2} \quad (5.1)$$

$$PA = N_{(x,y,)} \times L_p^2 \quad (5.2)$$

where $N_{(x,y,)}$ is the number of aggregate pixels, (x_i, y_i) is a spatial coordinate of an aggregate pixel i, and (x_{cm}, y_{cm}) is a spatial coordinate of aggregate image's the center of mass:

$$x_{cm} = \frac{\sum_{i=1}^{N_{(x,y,\alpha=1)}} x_i}{N_{(x,y,\alpha=1)}} \quad (5.3)$$

$$y_{cm} = \frac{\sum_{i=1}^{N_{(x,y,\alpha=1)}} y_i}{N_{(x,y,\alpha=1)}} \quad (5.4)$$

Calculated P, L_{max}, $R_{g,2D}$, and PA were non-dimensionalized with an aggregate's projected area weighted mean primary particle radius (a_p) (i.e. P/a_p, L_{max}/a_p, $R_{g,2D}/a_p$, and $PA/\pi a_p^2$).

To then estimate aggregate morphological descriptors and infer probable aggregate structures, a series of aggregates (more than 20,000) which were quasifractal in structure were generated computationally using the cluster-cluster algorithm (CCA) described by Filippov et al.[63] Quasifractal aggregates approximately obey the relationship:

$$N_p = k_f \left(\frac{R_g}{a_p}\right)^{D_f} \quad (5.5)$$

where N_p is the number of primary particles in an aggregate, k_f is the pre-exponential factor, R_g is the (three-dimensional) radius of gyration, a_p is the primary particle radius, and D_f is the fractal dimension. D_f ranges from between 1.0 and 3.0; higher fractal dimensions denote more dense aggregates, while aggregates with lower fractal dimensions are more chain-like. k_f values typically range from 1.0 to 2.0, and reflect the aggregate packing density.[248] The CCA enables determination of the locations of primary particles satisfying equation (1) with prescribed N_p, D_f, k_f, and a_p. CCA aggregates were generated with N_p = 10-3000, k_f = 1.0-2.0 and D_f = 1.3-2.9, with 10 aggregates for each (N_p, k_f, D_f) set generated. For each CCA aggregate, 3 orthogonal projections were examined (i.e. what would be viewed on a TEM image) and for each orientation, P/a_p, L_{max}/a_p, $R_{g,2D}/a_p$, and $PA/\pi a_p^2$ were determined. To obtain the four geometric parameters of a CCA generated quasifractal aggregate, a projection of the generated aggregate was obtained, and the two-dimensional spatial center coordinates of all primary particles of the aggregate were placed on an imaginary image domain. To determine whether an image domain pixel was a part of the aggregate projection, the distances between the pixel and the centers of primary particles were calculated. If the distance between the pixel and any primary particle of the aggregate was less than 1.0 (the dimensionless primary particle radius), 1.0 was assigned to the pixel's bit matrix location, otherwise the pixel was considered background and its bit matrix location was assigned a zero value. This pixel identification process was performed for all image domain pixels, enabling the calculations of P/a_p, L_{max}/a_p, $R_{g,2D}/a_p$, and $PA//\pi a_p^2$. CCA calculations thus led to a computational dataset with more than 60,000 entries listing N_p, D_f, and k_f, as well as P/a_p, L_{max}/a_p, $R_{g,2D}/a_p$, and $PA/\pi a_p^2$. For all

experimentally imaged aggregates, a comparison was made to the CCA dataset via calculation of a square error (E_j):

$$E_j = \left(1 - \frac{P_j/a_p}{P_{TEM}/a_p}\right)^2 + \left(1 - \frac{L_{max,j}/a_p}{L_{max,TEM}/a_p}\right)^2 + \left(1 - \frac{R_{g,2D,j}/a_p}{R_{g,2D,TEM}/a_p}\right)^2 + \left(1 - \frac{PA_j/(\pi a_p^2)}{PA_{TEM}/(\pi a_p^2)}\right)^2 \quad (5.6)$$

where the subscript "j" denotes the "j^{th}" dataset entry and the subscript TEM denotes the measured quantity. Subsequently for each experimentally observed aggregate, the most probable quasifractal descriptors were calculated as:

$$D_{f,TEM} = \frac{\sum_{j=1}^{j=j_{max}} D_{f,j} \times \exp(-bE_j)}{\sum_{j=1}^{j=j_{max}} \exp(-bE_j)} \quad (5.7a)$$

$$k_{f,TEM} = \frac{\sum_{j=1}^{j=j_{max}} k_{f,i} \exp(-bE_j)}{\sum_{j=1}^{j=j_{max}} \exp(-bE_j)} \quad (5.7b)$$

$$N_{P,TEM} = \frac{\sum_{j=1}^{j=j_{max}} N_{p,j} \exp(-bE_j)}{\sum_{j=1}^{j=j_{max}} \exp(-bE_j)} \quad (5.7c)$$

where b is a "bias factor", equal to 300 for our calculations. For each TEM observed aggregate, the CCA algorithm could then be used to predict a possible structure with equations (3a-c) results as inputs. While we employ this method in image analysis and note that prior studies have verified that the properties (i.e. diffusion coefficients and hydrodynamic radii) of aggregates analyzed via this approach agree well with experimental measurements,[245] at the same time we remark that it is not possible to extrapolate three-dimensional aggregate structures from two-dimensional projections with certainty. There is therefore some ambiguity in the structures inferred for aggregates; while it is likely that

the estimations of the numbers of primary particles per aggregate and fractal dimensions are reasonably accurate (as are parameters which scale with quasifractal descriptors), more detailed features of aggregate structures are not captured in analysis.

5.2.3 Nanoparticle tracking analysis & specific absorption rate measurements

To better understand the influence aggregation has on SAR, we additionally made measurements of the hydrodynamic radius distribution (R_H, linked to the distribution of number of primary particles per aggregates in the *Results & Discussion* section) of SPION aggregates and their specific absorption rates in variable concentrations (0.0, 0.25, 0.5, 1.0, 1.5, 2.0, 3.0, 4.0 and 5.0X) of phosphate buffered saline. Hydrodynamic radii distribution functions were inferred via nanoparticle tracking analysis (NTA)[43] with a Nanosight™ LM14 (Malvern Instruments LTD, Malvern, Worcestershire, UK). For NTA, each sample was diluted such that it contained 6.0 mg Fe/ml. SPIONs were allowed to aggregate for 4 hours prior to NTA. Measurements were performed more than 10 times for each PBS concentration, and hydrodynamic radii of all tracked individual aggregates were extracted as output data. The hydrodynamic radius distribution function of each sample was constructed by the procedure delineated in Jeon et al.[226]

Under identical suspensions conditions (PBS concentration), SAR measurements were made as described by Etheridge et al[206] and Hurley et al.[209] Briefly, a 1.0 mL sample in a centrifuge tube was placed within the inductive copper coil (2.75-turn) of a 1 kW Hotspot inductive heating system (Ambrell Corporation, Scottsville, NY). An alternating magnetic field at a frequency of 190 ± 10% kHz was applied to each sample for 180 seconds with a field strength of 20.0 kA/m. The temperature increase of each sample

during heating was recorded with a Luxtron 3100 fluoroptic thermometry system (Luxtron Inc., Santa Clara, CA). The maximum linear fit of time rate of temperature change for 15 ~ 20 seconds within the initial minute of heating was calculated, from which SAR was estimated. At least 3 SAR measurements were performed for each suspension; most measurements exhibit low measurement-to-measurement variation.

5.3 Results and discussion

5.3.1 Aggregate morphology quantification in vitro

Representative TEM images of SPIONs in the intra- and extra-cellular milieu of two LNCaP cells are displayed in Figures 5.1 and 5.2. Enlarged images of selected cell regions are also provided. Evident in all images is that the SPIONs do in fact persist as aggregates in both intracellular regions and extracellular regions. Qualitatively we also find that intracellular SPION aggregates are highly localized, i.e. they are confined within specific vesicles, indicative of uptake via endocytosis. This is in agreement with prior studies of SPION cellular distributions.[193, 206, 208] Uptake of SPION aggregates is visually evident in image (c) of Cell 2, where it appears that multiple SPION aggregates are being actively taken up into the cell. The extracellular SPION aggregates are found to be more evenly distributed in the volume elements between cells.

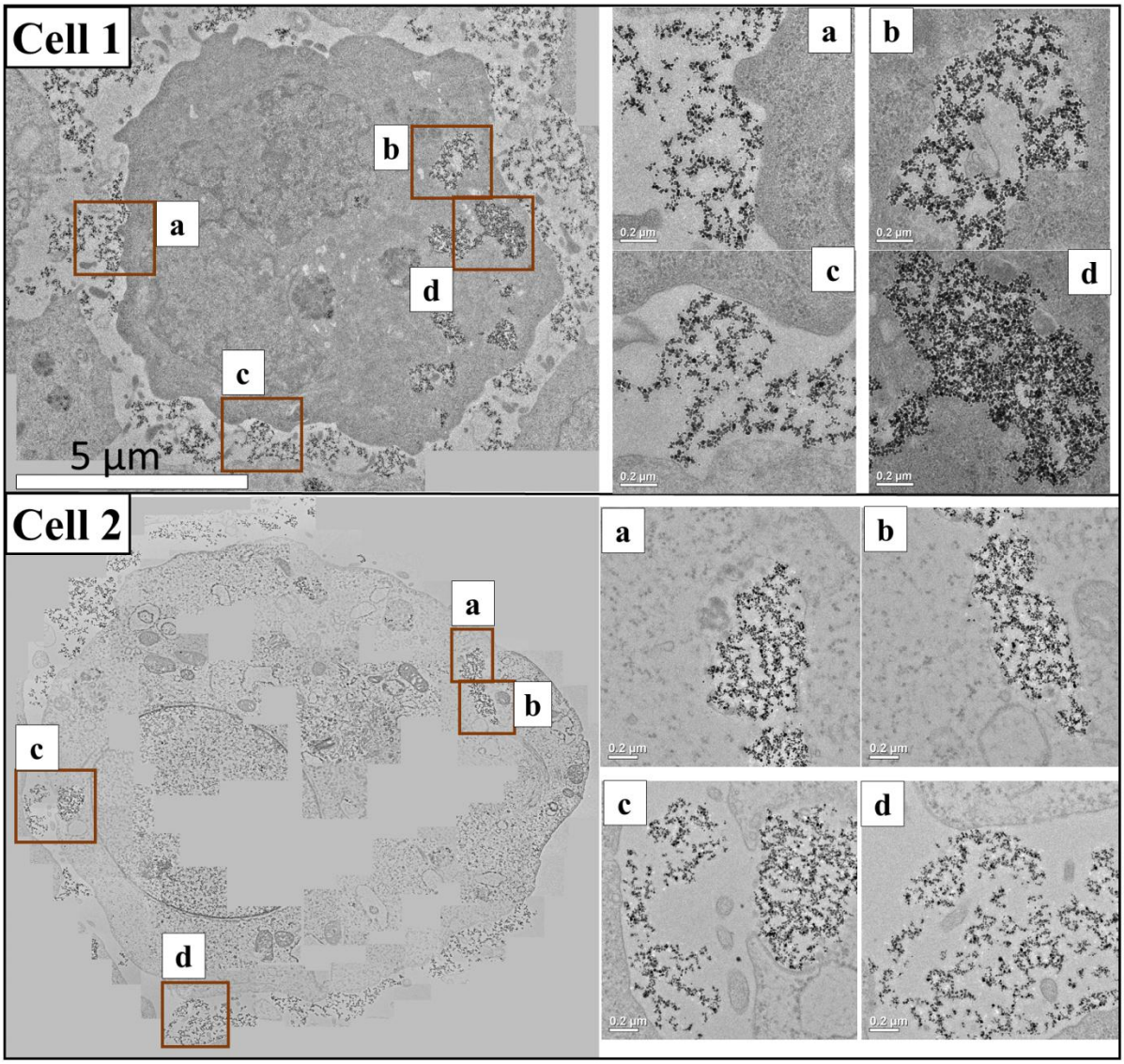

Figure 5.1. Transmission electron micrographs of SPION aggregates in the extra- and intracellular regions of Cell1 and Cell2. (a-d) denote zoomed in images of selected regions.

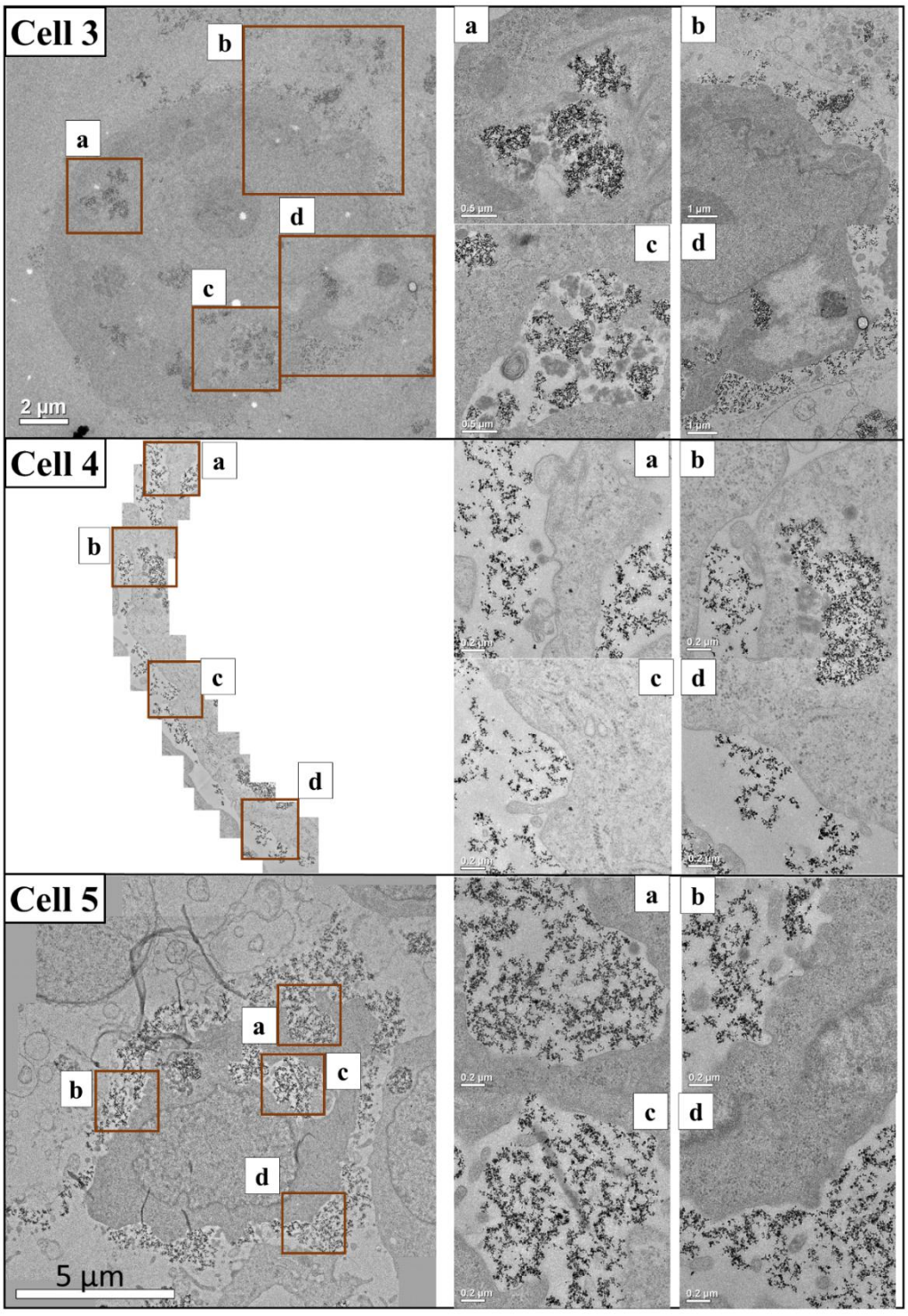

Figure 5.2. Transmission electron microscopy images of cells 3, 4 and 5. TEM images of Cell 1, 3 and 5 are also presented in Etheridge et al [206]and Hurley et al [209].

As described in the *Experimental Methods* section, isolated SPION aggregate images from both the intracellular and extracellular milieu were used to construct a bit matrix for two-dimensional property calculation, and a similar procedure was applied to a large number of computationally generated projections for comparison. An example of this procedure is provided in Figure 5.3 (a-c), where (a) shows the TEM image of an extracellular SPION aggregate, (b) shows the aggregate isolated from its surroundings with primary particles identified, and (c) shows a replotting of the aggregate projection based upon its bit matrix, with its four two dimensional size descriptors depicted. Analogously, Figure 5.3 (d) displays a computationally generated aggregate (D_f 1.7, k_f 1.7 and N_p 100), (e) displays the computationally generated aggregate projection, and (f) shows a replotting of the computationally generated aggregate projection based upon its bit matrix. For all computationally generated aggregates and for all imaged SPION aggregates, the parameters depicted in Figures 5.3 (c) and (f) were compared with equation (5.6), and fractal descriptors of imaged SPION aggregates were calculated with equations (5.7a-c). Results from selected aggregates are provided in Figure 5.4 for (a) extracelluar SPION aggregates and (b) intracellular SPION aggregates. In both subfigures, the determined quasifractal descriptors and a CCA generated aggregate with such size descriptors are displayed. In total, we repeated this procedure for 285 extracellular aggregates and 139 intracellular aggregates. While we can remark that the reconstructed CCA aggregates share many similar structural features with the observed projections, what is more important is to examine the distribution of properties (quasifractal descriptors) for the inferred aggregates.

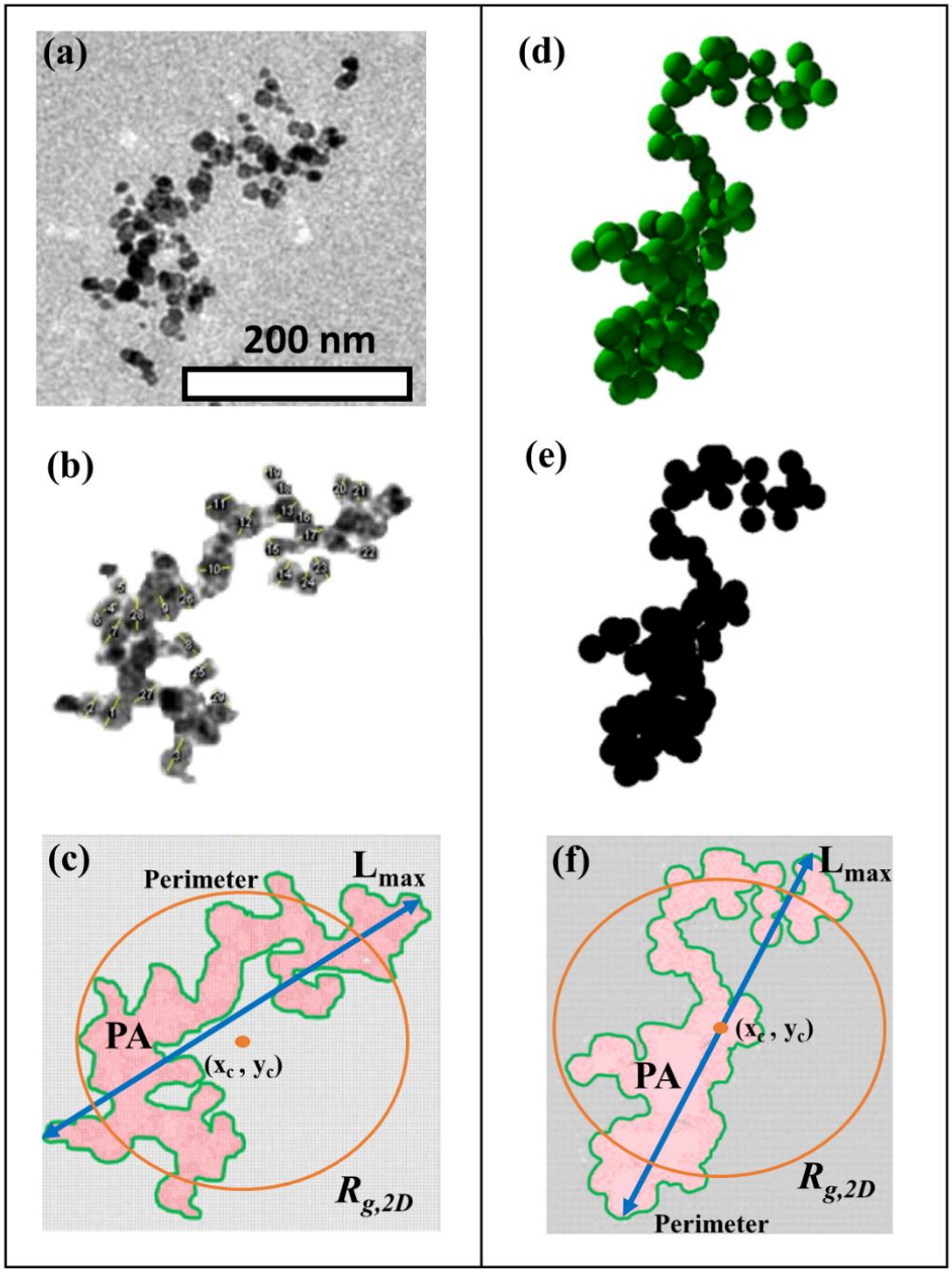

Figure 5.3. (a) An image of an isolated SPION aggregate. **(b)** The SPION aggregate with the background removed. **(c)** Depictions of the two-dimensional size descriptors for the aggregate based upon its bit-matrix. **(d)** Depiction of a CCA generated quasifractal aggregate with $N_p = 100$, $k_f = 1.7$, $D_f = 1.7$. **(e)** A computationally generated two-dimensional projection of the CCA generated aggregate. **(f)** Depictions of the two-dimensional size descriptors for the CCA aggregate based upon its bit matrix.

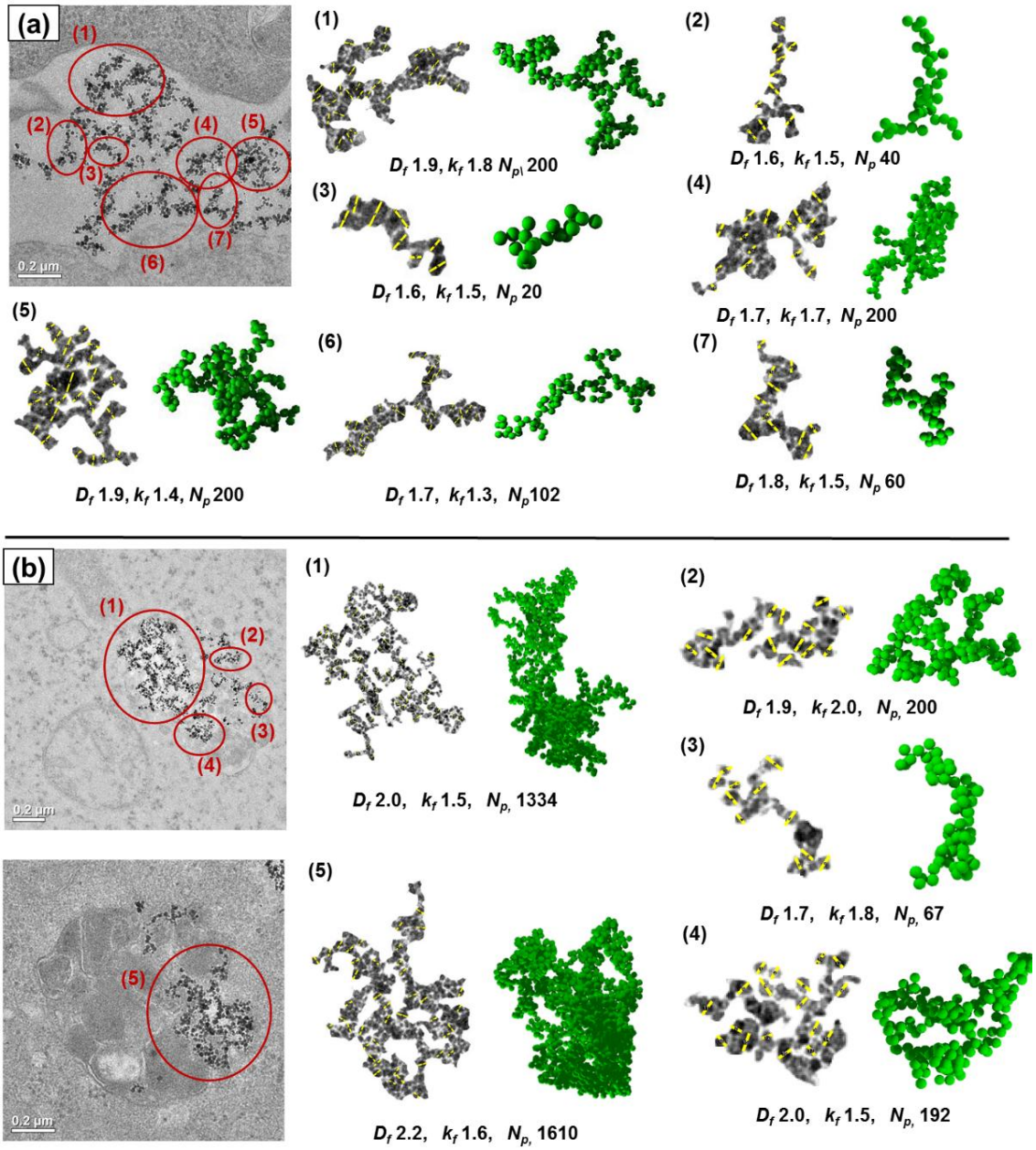

Figure 5.4. Depictions of selected aggregate projections and probable aggregate structures resulting from two-dimensional size descriptor analysis for extracellular aggregates **(a)** and intracellular aggregates **(b).**

Considering all imaged and analyzed aggregates, the normalized distribution function of number of primary particles per aggregate (i.e. the fraction of aggregates with primary particles in a given N_p range normalized by the $\log_{10}$ width of the range, as a

function of N_p) is displayed in Figure 5.5 (a). An overwhelming fraction of intracellular aggregates are composed of more than 10^3 primary particles; meanwhile no such "superaggregates" are observed in the extracellular milieu. For this reason, the average number of primary particles that aggregate in intracellular milieu is more than five times higher than in extracellular milieu (652 to 125). This finding correlates the reduction in SAR for SPIONs in the presence of cells to the formation of such superaggregates (i.e. those with more than 10^3 primary particles), which likely result from the endocytosis of multiple smaller aggregates. Confirmation that superaggregates are causally linked to SAR reduction is provided in the subsequent sections.

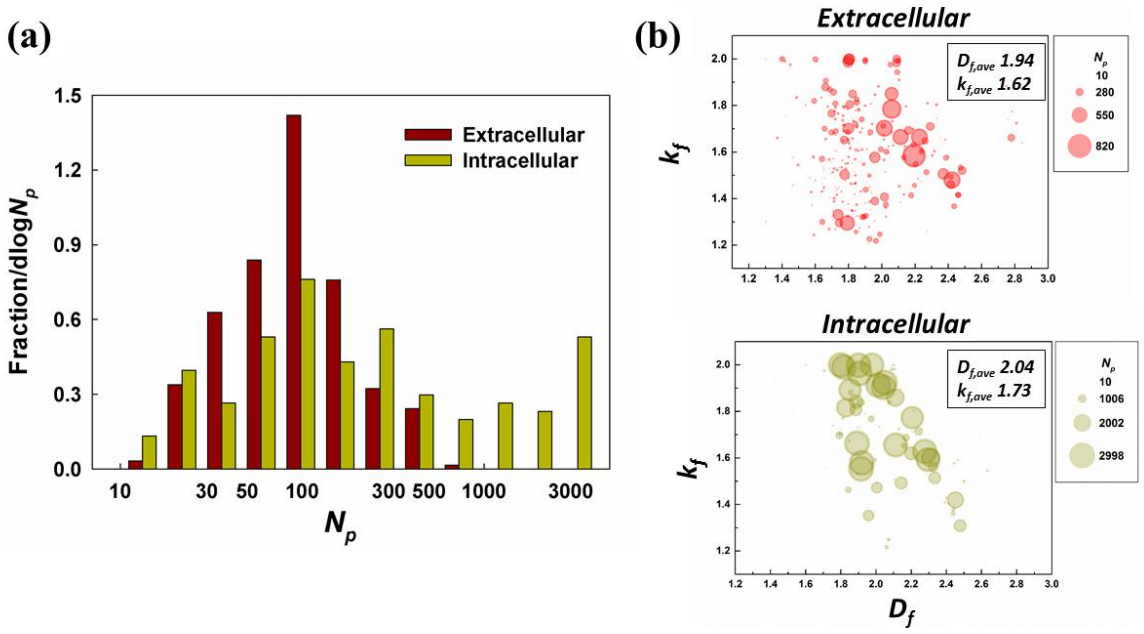

Figure 5.5. (a) The normalized N_p distribution function for aggregates based upon image analysis and **(b)** Plots of the k_f and D_f values inferred for all aggregates. Data point size is proportional to the number of primary particles in each aggregate.

Though intracellular SPION aggregates are significantly larger, their other quasifractal descriptors do not differ significantly from extracellular aggregates. Figure 5.5(b) contains plots of the k_f and D_f coordinates for all examined aggregates, with the size of each data point proportional to the number of primary particles per aggregate. Nearly all SPION aggregates, independent of whether they were found in extracellular or intracellular matrices, have k_f in the 1.2 – 2.0 range and D_f in the 1.6-2.2 range. The number of primary particles per aggregate weighted fractal dimension ($D_{f,ave}$) was similar in both the extra- and intracellular milieu, as was the average pre-exponential factor $k_{f,ave}$. Average fractal dimension values in the 1.8-2.1 range indicate that the mechanism by which SPION aggregates form is simply traditional diffusion-limited cluster aggregation or reaction-limited cluster aggregation; these two mechanisms, examined in numerous prior studies,[213, 249-253] lead to aggregates with fractal dimensions in the noted range, hence the results obtained for quasifractal descriptors are not surprising for an unstable colloidal system. Nonetheless, the agreement between the quasifractal descriptors inferred here and those expected based on prior experimental and theoretical studies of aggregation (in significantly more controlled environments) gives further credence to the application of image analysis for quasifractal aggregate description.

5.3.2 Aggregate hydrodynamic sizes and specific absorption rates

To test the hypothesis that the formation of superaggregates drives observed reductions in SAR, we performed SAR measurements on populations of well-characterized SPION aggregates. For such characterization, we first note that quasifractal descriptors, in conjunction with the CCA algorithm to reconstruct candidate aggregate structures, can be

used to predict other aggregate properties which link to their structure (e.g. light absorbance and scattering properties[254]). Along these lines an easily observable parameter is the hydrodynamic radius, which is solely a function of size and morphology. In both extracellular and intracellular media, the SPION aggregate D_f values and k_f values are close to 1.9 and 1.7, respectively, for most aggregates. We employed the CCA algorithm to reconstruct aggregates with variable N_p and with this D_f and k_f combination, and then employed the methods of Hubbard, Douglas, and coworkers [255-257] to infer the hydrodynamic radius for each aggregate (specifically using the algorithm provided in the Supplemental Information of Gopalakrishnan et al[258]). Power law regression to these results yields the relationship: $\frac{R_H}{a_p} = 0.903 N_p^{0.49}$ ($R^2 > 0.999$); this equation can be applied to infer the number of primary particles per aggregate from hydrodynamic radius measurements. The regression equation was applied to NTA measurements of hydrodynamic radii distribution functions, with results shown in Figure 5.6(a) (the distribution functions themselves) and (b) (values of the mean size, as well as 50% and 90% sizes based upon cumulative distribution functions). In determining distribution functions in terms of N_p, we used a_p = 6.9 nm, which was the average based upon direct analysis of more than 700 SPION primary particles. Additionally, the distribution functions are weighted by N_p, i.e. they are effectively mass-weighted distribution functions. Results reveal that increasing PBS concentration leads to increased aggregate growth (as anticipated) with the formation of superaggregates observed in 2.0X PBS as well as higher ionic strength suspensions

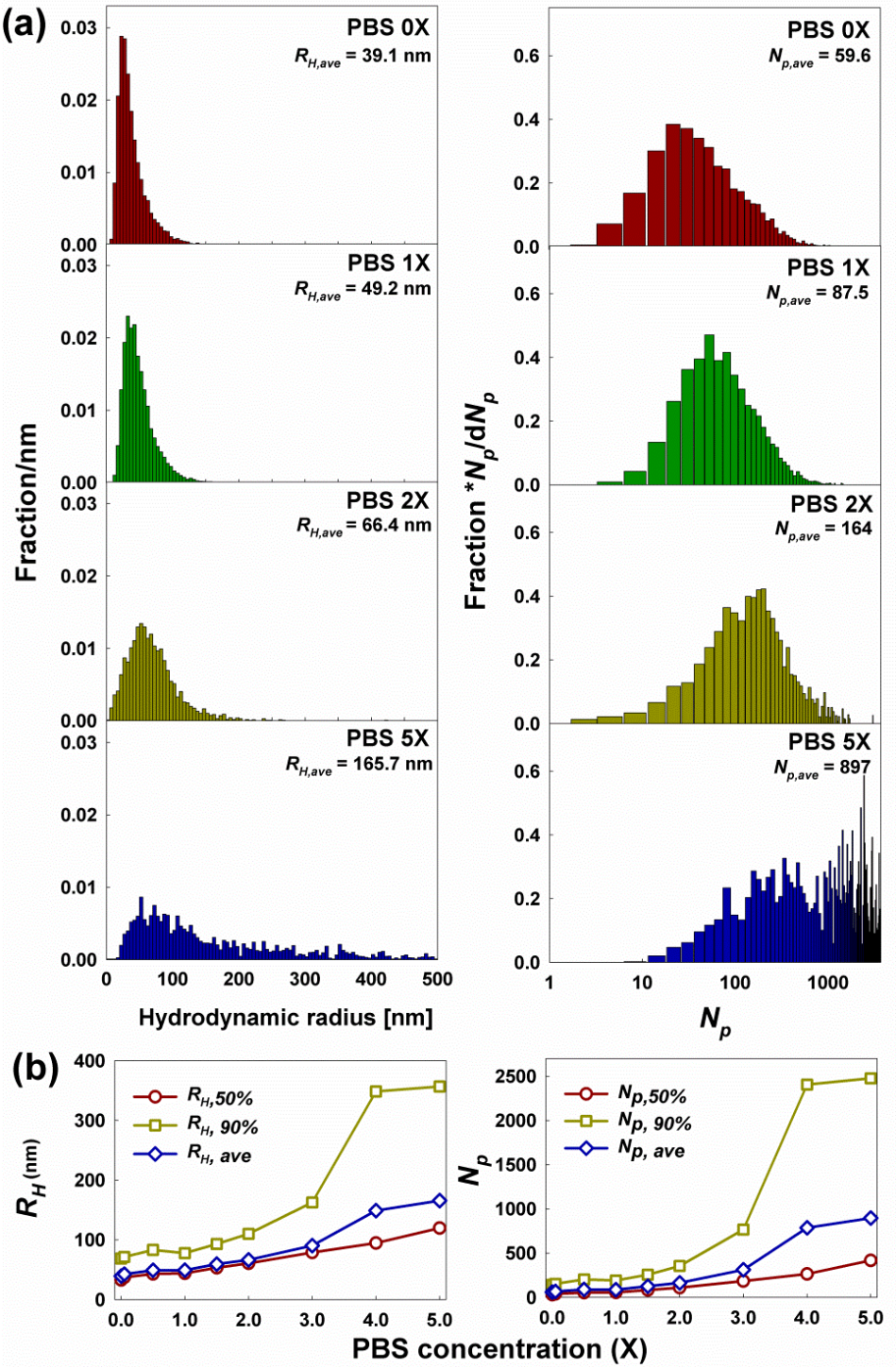

Figure 5.6. (a) Hydrodynamic radius and N_p based size distribution functions for SPION aggregates in variable PBS concentration suspensions, as measured by NTA. **(b)** Plots of the mean hydrodynamic radius and N_p values for NTA-inferred size distribution functions, as well as the 50% and 90% values for cumulative distribution functions.

Corresponding SAR measurements for the nine examined suspensions are displayed in Figure 5.7. Error bars represent the standard deviation of measurements (3-5 replicates). In line with prior studies,[196, 206, 207] increasing PBS concentration, which leads to the formation of larger and larger aggregates, correlates with a reduction in SAR.

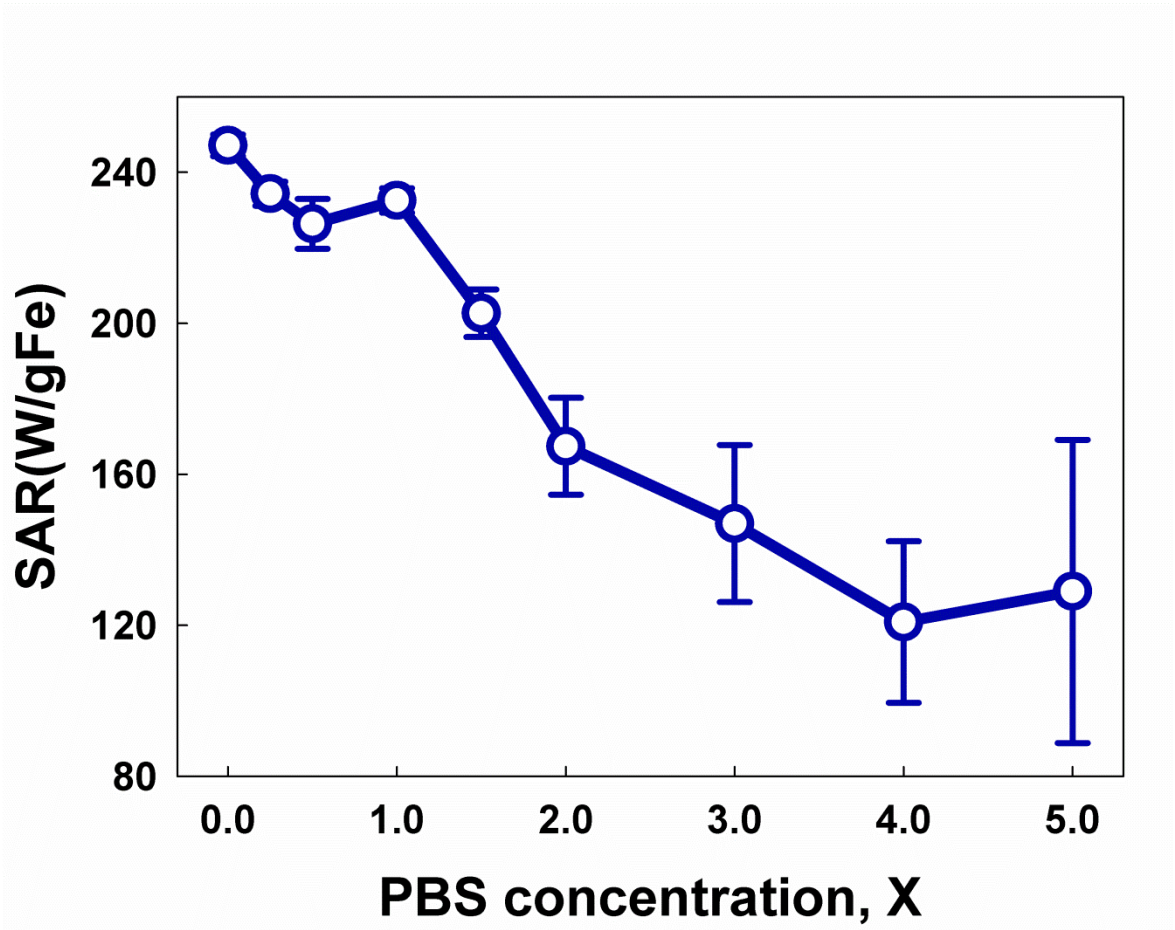

Figure 5.7. Measured SAR for SPIONs in variable PBS concentration suspensions. Error bars represent the standard deviation for 3-5 measurements.

However, preferable to such qualitative correlation is estimation of a functional dependency between SAR and N_p, the number of primary particles per aggregate. We attempt to invert such a function (SAR(N_p)) from the results reported in Figures 5 and 6 by applying a modified Metropolis inversion algorithm.[259, 260] Briefly, this approach involves initially guessing a relationship between SAR and N_p, with the assumption that

for a given SPION primary particle size and morphology (quasifractal descriptors), it is only N_p which influences SAR. Though the resulting function SAR(N_p) should be relatively insensitive to the initial guess, the time required to attain a suitable function is dependent on it. Here, we initially use SAR(N_p) = 250 W g^{-1} for all N_p. We describe SAR(N_p) at 8 specific points, with cubic spline interpolation used for intermediate values and those beyond the examined range. The modified Metropolis algorithm is used to modify the SAR(N_p) function by making random changes to the function at one specific point only. After this modification, SAR values for all suspensions examined (i.e. each PBS concentration) are calculated via the equation:

$$\text{SAR}\rfloor_g = \frac{\int_0^\infty \text{SAR}(N_p) N_p \frac{dn}{dN_p} N_p}{\int_0^\infty N_p \frac{dn}{dN_p} N_p} \tag{5.8}$$

where $N_p \frac{dn}{dN_p}$ is distribution function displayed in Figure 5 (derived from NTA measurements). Predictions of SAR are compared to measured results (Figure 6) via calculation of the value P_S:

$$P_S = exp\left(-\sum_{i=1}^{N_S} \left| 1 - \left(\frac{\text{SAR}\rfloor_{g,i}}{\text{SAR}\rfloor_{m,i}}\right)^2 \right| \right) \tag{5.9a}$$

where N_S is the number of suspensions examined (9 in this study), $\text{SAR}\rfloor_{g,i}$ is the guessed SAR value for sample i, and $\text{SAR}\rfloor_{m,i}$ is the measured value for sample i. We remark that the definition of P_S used here differs slightly from the traditional P definition in Metropolis

inversion routines.[259] Although it is not rigorously derived, it leads to stricter requirements on the comparison between predicted and measured values. If the new guess function SAR(N_p) leads to an increased P_S value over the previous value, then the guess function is accepted, and in turn modified to create a new guess function (for which P_S values are calculated and the process repeats). However, if the new P_S value is less than the previous value, then the new SAR(N_p) is accepted with a probability P_A:

$$P_A = exp\left(-\left(\frac{P_{S,old}}{P_{S,new}}\right)^2\right) \tag{5.9b}$$

where the subscripts "new" and "old" denote the values for the newly guessed and previous SAR(N_p). Like equation (5.9a), equation (5.9b) differs from the traditional Metropolis algorithm acceptance criteria, and is stricter (i.e. it leads to low P_A values). If the new function is not accepted, the old function is modified by a different random perturbation, and the P_S-P_A calculation procedure is repeated. After ~150 iterations of the modified Metropolis algorithm, oscillatory behavior in P_S is observed, indicating that the algorithm does not further improve the SAR(N_p) function. The algorithm is therefore ceased and SAR(N_p) at this point is accepted to accurately resemble the true SAR(N_p) function (note we assume a global minimum is obtained via this approach).

With the initial guess function, $P_S = 3.97\times10^{-5}$, the final SAR(N_p) function leads to $P_S = 0.433$ (which is considered extremely close to unity). The initial and final SAR(N_p) functions are plotted in figure 5.8 (a), while the measured SAR values and final predicted SAR values are shown in figure 5.8 (b). On average, measured and predicted SAR values are within 9% (+/- 4%) of one another for all measured suspensions. The final SAR(N_p)

function, somewhat surprisingly, shows a modest increase as N_p increases from 3 to 10, but then rapidly decreases at larger N_p. Extreme decreases (below 100 W g^{-1}) are obtained for superaggregates with $N_p > 1000$. While the increase in SAR at small N_p may be an artifact of the data analysis approach applied, the decrease in SAR with superaggregate formation is extremely clear; thus data inversion confirms that it is in fact the formation of superaggregates in intracellular milieu which leads to reductions in SAR for SPIONs in cell-containing suspensions.

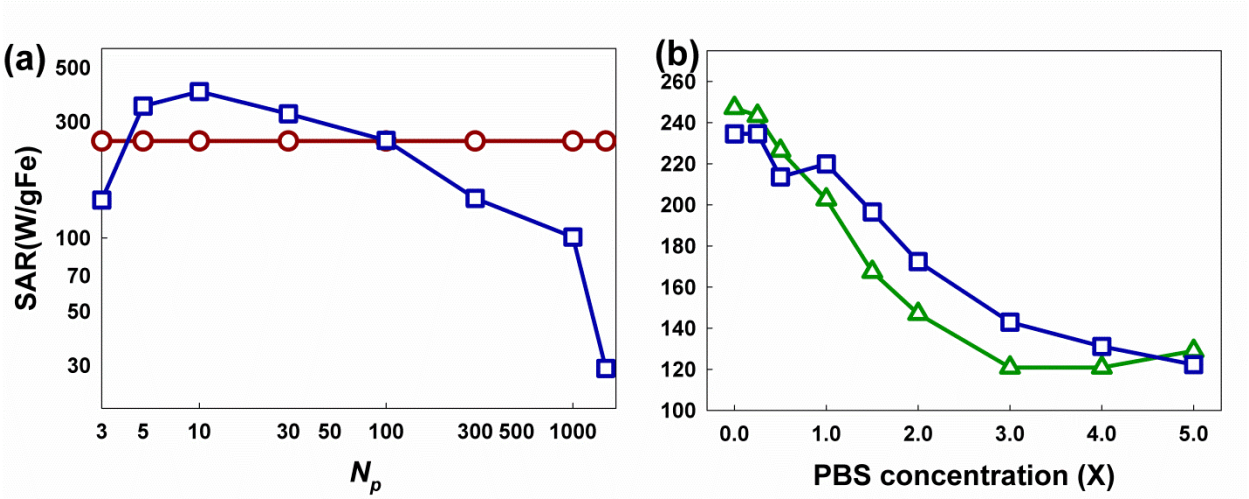

Figure 5.8. **(a)** A plot of the initial guess (red circles) and final inverted (blue squares) SAR (N_p) functions. **(b)** A comparison of the measured (blue squares) SAR values and predicted (green triangles) SAR values based upon the final SAR(N_p) function for suspension in variable PBS concentration suspensions.

The inverted SAR(N_p) function can be used in conjunction with the results presented in Figure 5.5 (image analysis based size distribution results) to develop a SAR distribution function for aggregates in an extra- or intracellular milieu. For each imaged aggregate, we use its inferred number of primary particles to determine its unique SAR.

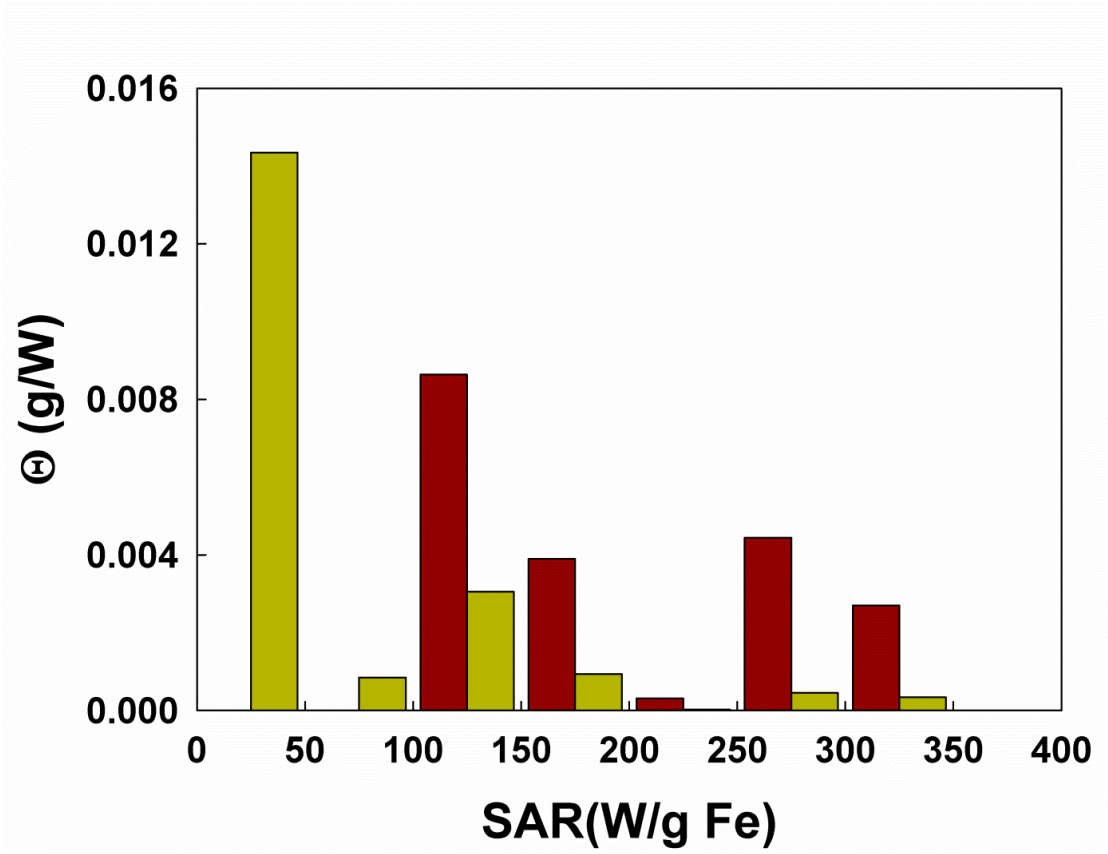

Figure 5.9. The inferred SAR distribution function, Θ, for extracellular (red) and intracellular (yellow) aggregates.

We then bin aggregates by SAR, weighting each aggregate by its number of primary particles. Dividing each bin's total by the bin width (dSAR) and the total number of primary particles for all aggregates leads to a normalized SAR distribution function, Θ (with units of g W^{-1}). This function is plotted in Figure 5.9 for both extra- and intracellular milieu. Apparent in the plot is that a large portion of the intracellular SAR distribution lies at SAR values below 100, i.e. our results suggest that many of the intracellular aggregates (superaggregates) do not contribute substantially to heating. In addition, integration of the SAR distribution function leads to the expected SAR; for extracellular aggregates we find that SAR = 198.5 W g^{-1}, while for intracellular aggregates we find that SAR = 44.4 W g^{-1}. These two values bound the measured value of SAR = 120 +/- 20 reported by Etheridge et

al [206] for the same SPIONs within LNCaP cell suspensions. This provides further evidence that the data analysis approach applied in characterizing aggregates and inverting the function SAR(N_p) are reasonably accurate.

5.4 Conclusions

We apply a combination of transmission electron microscopy, image analysis techniques, nanoparticle tracking analysis, SAR measurements, and novel data deconvolution schemes to examine the structures of SPION aggregates in extra- and intracellular milieu in LNCaP cell suspensions, with the ultimate goal of understanding why SAR decreases for SPIONs in cell suspensions. Overwhelmingly, our results suggest that cellular endocytosis of multiple extracellular aggregates (formed by diffusion- or reaction-limited aggregation, as the environments conducive to cell growth are not suitable to maintain colloidal stability) leads to the formation of superaggregates composed of more than 10^3 primary SPION particles. These superaggregates do not appear to contribute to heating substantially, as their inferred SAR values are an order of magnitude below the inferred SAR of smaller aggregates. Therefore, to apply SPIONs in hyperthermia based therapies, we suggest that it is not essential to avoid aggregation completely, but that it is critical to hinder superaggregate formation. Prior studies focusing on SPION surface functionalization suggest that mitigation of aggregation along these lines is possible.[209, 217, 218]

Although our work provides consistent evidence that superaggregates have substantially reduced SAR, the mechanism by which this is brought about is not investigated, and further studies will be needed to better understand this phenomenon.

Recent Monte Carlo based simulations [261] of SPION heating in alternating magnetic fields do suggest that the crowding of SPIONs close to one another, as is the case in aggregates, leads to a reduction in SAR; however, to-date simulations with aggregates (and superaggregates) have not been reported.

Finally, we remark that the aggregate characterization methods used in this study, in which images are quantitatively analyzed to infer aggregate structural descriptors and these structural descriptors are employed in the analysis of ensemble measurements (i.e. nanoparticle tracking analysis), are quite general. They may find utility in examining nanoparticle aggregation and distribution at the cellular level for a variety of other systems.

Chapter 6

Evaluation of Nanoparticle Aggregate Morphology during Wet Milling

Summary

Recently developed wet mills (bead mills) have been shown capable of dispersing nanoparticle aggregates into primary particles in suspension, even with nanoparticles with primary particle radii as small as 5 nm and at high nanoparticle volume fractions (> 1%). However, to date what has not been examined is the change in aggregate morphology during milling itself, i.e. it is not clear if wet milling simply fragments aggregates into smaller, similarly structured entities, or if milling can simultaneously lead to aggregate restructuring. Here we develop and apply methods to examine the change in morphology in titania and alumina nanoparticle aggregates (primary particle radii of ~8.25 nm and 7.20 nm, respectively) during wet milling with a Kotobuki Industries UAM-015 wet mill. Specifically, via nanoparticle tracking analysis (NTA) with a Nanosight LM-14 and simultaneous viscosity measurements, we characterized the hydrodynamic radius distribution functions and average intrinsic viscosities of both titania and alumina aggregates milled at 1% volume fraction in water. With NTA we found that for both particle types, milling led to a reduction in hydrodynamic radii. Conversely, the average intrinsic viscosity of titania decreased, while it increased for alumina with increasing milling time. By assuming aggregates were quasifractal in morphology (and hence characterized by the number of primary per particles per aggregate, the pre-exponential factor, and the fractal dimension) and by using Monte Carlo based techniques to link quasifractal aggregate descriptors to both the hydrodynamic radius and the intrinsic viscosity for an aggregate, measured hydrodynamic radius distribution functions and average intrinsic viscosities were used to infer titania and alumina aggregate quasifractal descriptors as functions of milling time. Through this analysis we found that both particle types were initially dense aggregates (fractal dimensions > 2.9), and for titania milling did not alter aggregate morphology (i.e. titania aggregates remained dense). However, alumina

aggregates were found to decrease in fractal dimension with increasing milling time, reaching a value near 1.6 after 180 minutes of milling. Such chain-like structures give rise to an increase in suspension viscosity despite the fact that alumina aggregate size decreased with milling. Overall, we show that depending on the particle material (and surfactant employed), milling may simultaneously lead to aggregate size reduction and restructuring, and may be a viable approach to the production of controlled morphology aggregates.

6.1 Introduction

Most industrial and medical applications of inorganic (metal and metal oxide) nanoparticles require that the particles remain stable (i.e. do not aggregate) in a particular solvent [262-266]. However, nanoparticles are rarely synthesized in the solvent in which they will be later dispersed for application, and subsequent to synthesis (either via liquid or gas phase processes) nanoparticles are frequently stored as dried powders [267-270], wherein van der Waals interactions bind nanoparticles together as aggregates. Upon introduction to a given solvent, dried powder aggregates are not necessarily immediately dispersed (even if surfactants which stabilize suspensions are added), as there remains a van der Waals energy barrier to aggregate breakup. The creation of stable nanoparticle dispersions hence typically requires the use of a high energy grinding process, such as wet milling [271-274]. Along these lines, a number of advances have been made in the development of wet bead mills in the past decade. In particular, recently devised bead mills [275-283] can utilize micrometer sized ZrO_2 beads in a slurry to disperse aggregates into individual primary nanoparticles with characteristic sizes as small as 10 nm. With proper suspension conditions, milled nanoparticles can remain dispersed over the course of days, even with nanoparticle mass fractions as high as 10%. Key to the development of such mills has been the addition of a centrifuge downstream of the bead vessel (where bead-

bead collisions occur) which is capable of separating out beads as small as 15 μm from suspensions flowing through the milling system [275].

The efficacy of such bead mills when proper milling conditions are applied and reaggregation is mitigated is not in question. However, lacking are studies which examine changes in the morphologies of aggregates as milling proceeds, both under conditions where a stable nanoparticle dispersion is produced, and under conditions where complete dispersion is not achieved. Aggregate characterization during the milling process is not only of fundamental interest, but could also further aid in advancing milling technology; stable dispersion production can require 6-10 hours [276] and determination of the appropriate surfactant type and concentration needed to maintain suspension stability is often performed with a trial-and-error approach. Additionally, certain applications may benefit not from having stably dispersed primary particles, but rather stably dispersed aggregates where the extent of aggregation is controlled [284-289]. Therefore, techniques to evaluate aggregate morphology during milling would save substantial time in milling protocol design.

In this study, we develop and apply methods to quantitatively characterize aggregate morphologies during bead milling processes for aggregates in the sub-100 nm size range, which are difficult to structurally analyze by static light scattering [290]. Specifically, we used a Kotobuki Industries ultra-apex mill (UAM 015) with 50 μm ZrO_2 beads to disperse commercially produced titania (TiO_2) and alumina (Al_2O_3) nanoparticles in water. The former was chosen as a model system as stable primary particle dispersions have been produced with it previously[275], while studies show the dispersion of the latter is much more challenging [291]. To characterize aggregate morphology during milling,

hydrodynamic radii distribution functions and suspension intrinsic viscosities were measured periodically, and by modeling the aggregates as quasifractal structures [292-295] (described by the number of primary particle per aggregate, the primary particle size/radius, the fractal dimension, and the pre-exponential factor), the fractal descriptors of particles were inferred from measurements. In the sections that follow, the results of titania and alumina dispersion experiments are described in greater detail as is the procedure we have developed to infer aggregate morphology in suspensions. We show that in these two instances aggregate morphologies were initially quite similar, but as milling proceeded, the titania aggregates, while decreasing in size, changed little in morphology, while alumina aggregates both fragmented and underwent substantial restructuring into chain-like aggregates.

6.2 Materials and methods

6.2.1 Materials

Metal oxide nanopowders of anatase titania (TiO_2,CAS registration # 637254) and gamma-phase alumina (Al_2O_3, CAS registration # 544833) were purchased from Sigma-Aldrich (Saint Louis, USA). Titania and alumina nanoparticles were added to ultrapure water (SpectraPure, Tempe, USA) at a volume fraction (V_f) of 1% and a total suspension volume of 500 ml. Sodium hexametaphosphate (Sigma-Aldrich (CAS # 71600)), an ionic surfactant often used to stabilize metal oxide nanoparticles in water, was added to each suspension at a concentration of 50% the mass concentration of nanoparticles. Specific information on the compositions of suspensions is provided in Table 6.1.

6.2.2 Bead milling

A schematic of the UAM 015 bead mill is provided in Figure 6.1, and is also presented in detail in earlier studies [275, 276, 296]. Briefly, the bead mill is composed of a 500 mL suspension reservoir, where samples are initially loaded, a peristaltic pump to facilitate the recirculation of suspensions through the mill, a vessel wherein the beads remain, and a centrifuge to remove beads at the vessel outlet. As milling proceeds, suspensions are recirculated from the reservoir to the vessel and centrifuge and back to the reservoir. For the presented experimental results, the vessel volume of 170 mL was loaded with highly monodisperse ZrO_2 beads with a diameter of 50 μm (obtained directly from Kotobuki Industries) at a volume fraction of 60%. The bead mill functions by harshly agitating beads within the vessel, such that during bead-aggregate-bead three-body collisions, aggregates break at nanoparticle-nanoparticle contact points. As described subsequently for nanoparticle aggregates, beads were periodically imaged via transmission electron microscropy; visible wear of beads subsequent to experiments was not evident in such images. The rotation speed settings of the vessel and the centrifuge region as well as the peristaltic pump must be controlled to ensure that (1) bead impacts do not fragment primary particles and (2) beads are separated from the flowing suspension in the centrifuge region. Such speeds are determined empirically; for the presented results the vessel and centrifuge speed setting was level "4" (out of 5, corresponding to rotation speed of 10 m/s for the centrifuge outer cylinder) and the peristaltic pump speed setting was 1.5 (out of 10). To maintain the vessel at a constant temperature, a sealed cooling water jacket was employed. During all experiments the water temperature was set to 7.5 ^{o}C via use of a recirculating chiller (Kodiak® Recirculating Chiller, Lytron, Woburn, USA). For both test

suspensions milling was carried over 180 minute periods, and 5-15 mL samples were extracted at time periods of 0, 5, 15, 30, 60, 90, 120, & 180 minutes for either hydrodynamic radius distribution function or intrinsic viscosity measurements. Milling experiments were performed twice for titania suspensions and three times for alumina suspensions to ensure that results were repeatable. For all suspensions, after milling for 15 minutes or more, sedimentation of particles from suspension was not observed for at least two week subsequent to experiments.

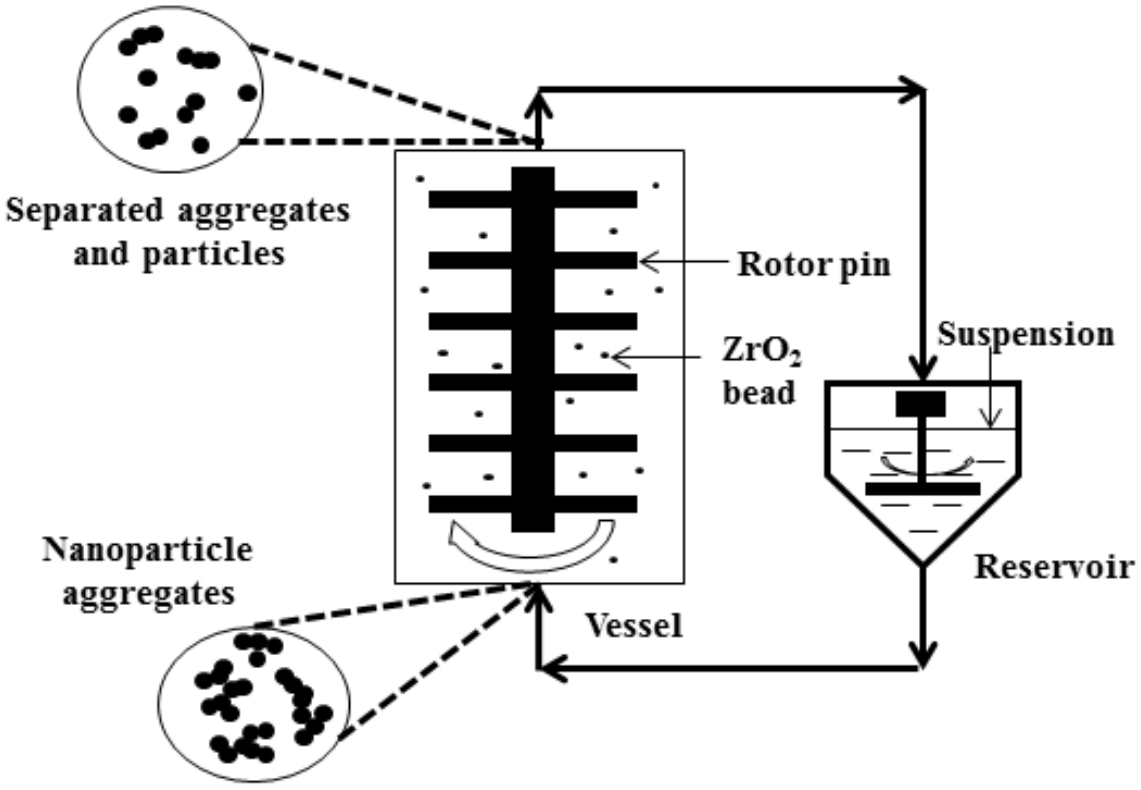

Figure 6.1. Schematic of the UAM-015 bead mill.

Table 6.1. A summary of the properties of the nanoparticles examined, as well as the nanoparticle masses, surfactant masses, and solvent volumes used in preparing suspensions.

Size			
Aluminum oxide (Al_2O_3)	Nanopowder, < 50nm particle size (TEM)		
Titanium oxide (TiO_2)	Nanopowder, 25nm, 99.7% metals basis		
Density (g/cm^3)			
Al_2O_3	3.95	Water	1
TiO_2	4.23	Surfactant	2.48
Material compositions of nanosuspension			
V_f 1% Al_2O_3 nanosuspension		V_f 1% TiO_2 nanosuspension	
m_p	19.75g	m_p	21.15g
V_w	491.02ml	V_w	490.74ml
m_s	9.88g	m_s	10.58g

6.2.3 Nanosight™ and hydrodynamic size distribution

Aggregate hydrodynamic radii (R_H) distribution functions (i.e. the number concentration of aggregates per unit hydrodynamic radius) were measured using 'Nanoparticle Tracking Analysis (NTA)'[297] with a Nanosight™ LM-14 (Malvern Instruments). In NTA, the Brownian motion of aggregates is monitored, yielding the scalar diffusion coefficient (D) for each aggregate. Via application of the Stokes-Einstein equation, $D = \frac{kT}{6\pi\mu R_H}$ (k: Boltzmann constant, T: temperature, μ: solvent dynamic viscosity), the hydrodynamic radius of each aggregate can be inferred, and entities with hydrodynamic radii as small as 5 nm may be directly observed with the LM-14. From measurement results, a fitting procedure can be used to reconstruct a probable hydrodynamic radius distribution function, or alternatively the hydrodynamic radii of all detected particles/aggregates may be directly output. For LM-14 measurements samples taken from the bead mill at specific times were diluted with ultrapure water by a factor of 10^2-10^3. The LM-14 temperature was set to 23°C. Prior to sample measurements, for

calibration NTA was performed on citrate stabilized near-monodisperse 80 nm gold nanoparticles (Nanocomposix, USA). NTA was performed 4 or more times for each sample, and rather than use a fitting procedure to determine the hydrodynamic radius distribution function, we elected to output directly the hydrodynamic radii of all examined particles at milling times of 15, 60, 120 and 180 minutes for both titania and alumina suspensions.

6.2.4 Viscosity measurement and intrinsic viscosity calculation

A glass ubbelohde viscometer (CANNON Instrument Company, PA, USA) was used to measure the kinematic viscosities of both titania and alumina suspensions after selected milling times. The viscometer employed has four measurement bulbs, enabling viscosity measurement at four different shear rates, and further enabling evaluation of Newtonian behavior via comparison of kinematic viscosities measured with different bulbs. We elected to use the first and second bulbs, which had viscosity constants of $0.003412 mm^2/s^2$ and $0.0031496 mm^2/s^2$, respectively, and corresponding shear rate constants 415687 and 219720, respectively, and in which measurement times varied between 300-800 seconds (the kinematic viscosity is calculated as the product of the viscosity constant and the residence time in the bulb, while the wall shear rate is the ratio of the shear rate constant to the residence time in the bulb). The temperature during all measurements was 20 ~ 23^{o}C (room temperature). For calibration, the kinematic viscosity of ultrapure water was measured, as was the kinematic viscosity of the control solution (ultrapure water with the surfactant). Viscosity measurements were made for suspensions milled for 15, 60, 120 and 180 minutes, immediately after collecting samples from the

suspension reservoir. At least three viscosity measurements were performed for each sample to ensure repeatability. From the known density and volume fraction for each suspension, the intrinsic viscosity $[\eta]$ was calculated via two approaches. First, neglecting high concentration effects, we used the equation:

$$\frac{\mu}{\mu_o} = 1 + [\eta]V_f \tag{6.1}$$

where μ is the dynamic viscosity of the suspension and μ_o is the dynamic viscosity of the solvent and solute together, without nanoparticles. The intrinsic viscosity is known be highly dependent on particle shape [298, 299]; for spheres, $[\eta]$ = 2.5, while $[\eta]$ is higher than 2.5 for other nonspherical objects, particularly those of high aspect ratio. These can lead to higher volume effects, hence, we also calculated $[\eta]$ using the equation [300, 301]:

$$\frac{\mu}{\mu_o} = 1 + [\eta]V_f + k_H[\eta]^2{V_f}^2 + \emptyset\left({V_f}^3\right) \tag{6.2}$$

where k_H is the Huggins coefficient, for which we assume a value of 1.0, that which has been found for hard spheres [300]. Inferred $[\eta]$ values and the hydrodynamic radii distribution functions for aggregates were used in conjunction with one another to infer aggregate morphologies, using the procedure described in the '*Results & Discussion*' section. We remark that in using equation (6.1), we neglect any electroviscous influences [302, 303], which are anticipated to be small.

6.2.5 Transmission electron microscopy

In conjunction with NTA and viscosity measurements, transmission electron microscopy (TEM) was used to characterize samples, both to (1) qualitatively examine the morphologies of aggregates at various milling times and (2) determine the primary particle size (radius) distribution functions. For samples milled for 15, 60, and 120 minutes, respectively, we used an FEI Tecnai T12 transmission electron microscope (University of Minnesota Characterization Facility Lab) to image aggregates. TEM samples were prepared by diluting milled suspensions ~1500 fold and drying the diluted suspension on a carbon grid carbon grid (200 mesh, Ted Pella INC, CA, USA). For primary particle radius size distribution evaluation, approximately 500 primary particles for both titania and alumina were examined at various milling times. Energy-dispersive X-ray spectroscopy (EDS) was also employed during TEM analysis to confirm that the observed particles were either completely titania or alumina, and that zirconia beads did not fragment or contaminate experiments.

6.3 Results and discussion

6.3.1 Hydrodynamic radius distribution functions and intrinsic viscosities

Prior to discussing the procedure we developed to infer the fractal descriptors for milled aggregates, we report directly the measured hydrodynamic radius distribution functions as well as the intrinsic viscosities of both titania and alumina samples. In all experiments, milling for 15 minutes or more produced stable suspensions. Particles were not observed to settle out of suspension for several days subsequent to milling and

measured hydrodynamic radii distribution functions remained unchanged during this time period. Figure 6.2 displays normalized hydrodynamic radius size distribution functions for both suspension types after 0, 15, 60, and 120 minutes of milling (for specific milling cases, with highly repeatable results obtained from trial to trial). These plots were constructed by binning the inferred hydrodynamic radii of in bin widths of 5 nm, then dividing the number of aggregates per bin by both the total number of aggregates and the bin width. As is expected in wet milling, with increased milling time the hydrodynamic distribution functions shifted to smaller sizes, confirmed in Figure 6.3, wherein the 50% and 90% hydrodynamic radii of the cumulative distributions functions for the hydrodynamic radius are plotted as functions of milling time. In prior studies [275-277], such shifts alone have been used to characterize the change in aggregate size and shape as milling proceeds, and alone they suggest that milling simply leads to progressively smaller aggregates. However, inference of intrinsic viscosities for milled aggregates alters this picture.

Figure 6.4 displays the intrinsic viscosities inferred from both equations (6.1) and (6.1), respectively, at various milling times, for all measured samples. For TiO_2, equations (6.1) and (6.2) inferred intrinsic viscosities are similar (difference of 3-5%) to one another, and as milling proceeds, they decrease from ~4.8 after 15 minutes of milling to ~3.5 after 120-180 minutes of milling. This is consistent with the results of NTA, milling appears to fragment aggregates into progressively smaller entities, approaching (spherical) primary particles. Conversely, for alumina, after 15 minutes of milling the inferred intrinsic viscosity is 11.7 and 10.5 from equations (6.1) and (6.2), respectively, and increases drastically as milling proceeds; after 180 minutes of milling the average equation (6.1)

intrinsic viscosity is 108 and the average equation (6.2) intrinsic viscosity is 65 (with clear trial-to-trial variation evident, though in all cases the intrinsic viscosity increases).

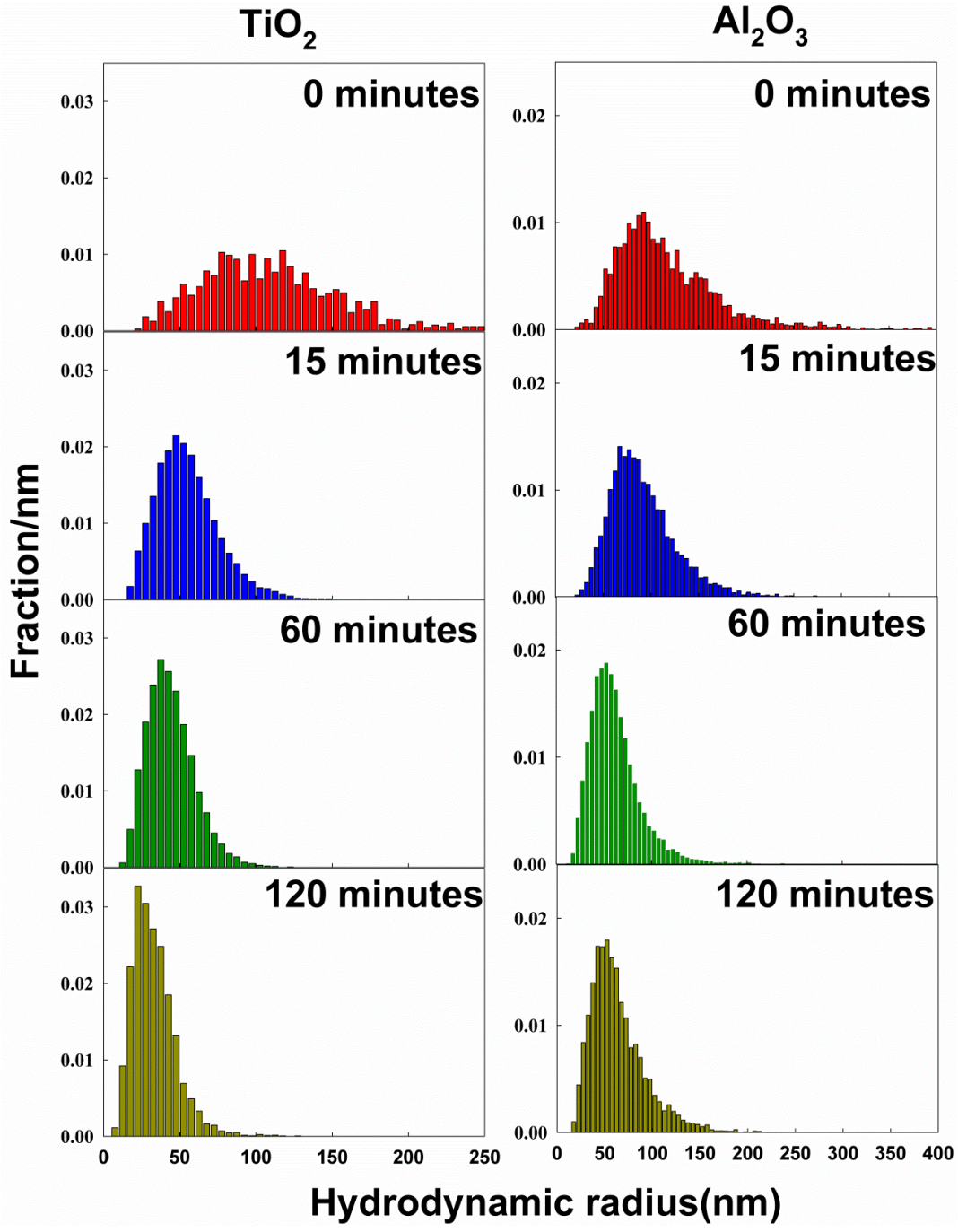

Figure 6.2. Normalized hydrodynamic radius distribution functions for milled titania and alumina aggregates, as measured by nanoparticle tracking analysis. Bin widths of 10 nm were used for construction of all distribution functions.

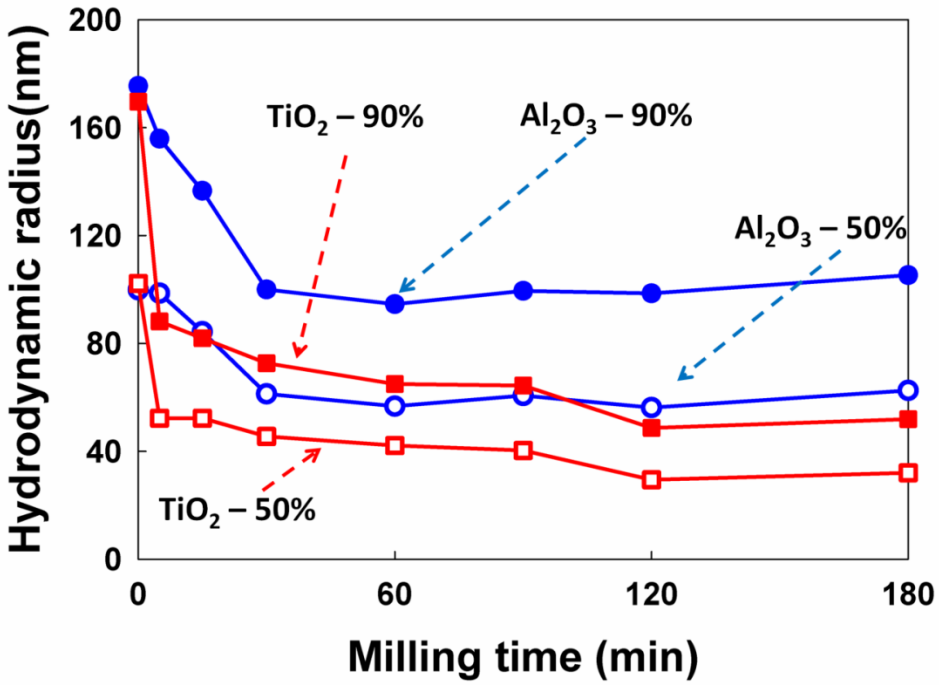

Figure 6.3. The 50% and 90% hydrodynamic radius values from the cumulative distribution functions of milled titania and alumina aggregates, as a function of milling time (min: minutes).

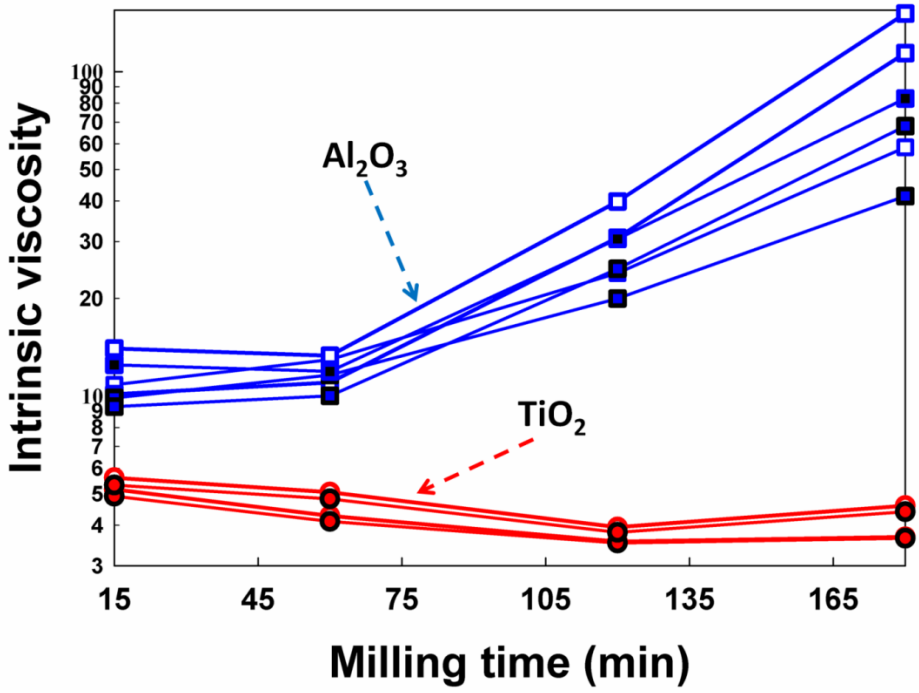

Figure 6.4. The equation 1a (open symbols) and equation 1b (closed symbols) inferred average intrinsic viscosities for titania and alumina suspensions as a function of milling time. Different lines denote different trials.

6.3.2 Transmission electron microscopy analysis

The finding that alumina aggregate hydrodynamic radii distribution functions are shifted to smaller sizes is inconsistent with the drastic increase in intrinsic viscosity observed with increasing milling time. Three possible reasons for this observation are: (1). Alumina primary particles might be highly non-spherical and more aspherical than aggregates themselves; (2) bead milling may have led to the fragmentation of zirconia beads, hence bead fragments were incorporated in alumina suspensions at appreciable concentrations (increasing V_f); (3) milling might lead to a reduction in the number of primary particles per aggregate, but simultaneously might lead to alumina aggregate restructuring into more ramified structures of higher intrinsic viscosity. We will argue here that (3) is the origin of the intrinsic viscosity increase for alumina suspensions. To rule out (1) and (2), TEM images of three suspensions (milled for 15, 60 and 120 minutes) of both titania and alumina aggregates were analyzed. Two TEM images for each suspension are provided in Figures 6.5 and 6.6. For both titania and alumina, while the primary particles (which have sub-15 nm radii) are slightly non-spherical, they are by no means as aspherical as the observed aggregates, dismissing (1). Through EDS, we were only able to observe carbon, copper, and either titanium or aluminum and oxygen in samples, indicating that zirconia bead fragments were not introduced into samples. Figure 6.7 shows examples of EDS analysis of alumina. Regions of highly concentrated alumina were intentionally investigated to confirm the absence of zirconia bead fragments in the nanosuspension. Further, as noted prior, no visible wear was observed on the zirconia beads themselves. These observations lead us to dismiss (2) as well. While we caution that the drying of samples prior to TEM analysis may have altered aggregate architectures from what was

present in suspensions, progressively smaller titania aggregates are evident in Figures 6.5 images with increasing milling time, and qualitatively, the titania aggregates observed are dense (i.e. of low aspect ratio). Conversely, Figures 6.6 images of alumina aggregates after longer milling times display much more branched/linear structures (though smaller in size than the unmilled aggregates) and in several circumstances we observed large, interconnected networks of alumina particles (as seen in the upper 120 minute alumina image). Therefore TEM images provide support for (3), i.e. they suggest that milling differentially fragments and restructures titania and alumina aggregates. As the formation of large alumina nanoparticle networks was undoubtedly facilitated by suspension drying, however, we elect not to perform further analysis of aggregate images, though we note that such analysis is possible when unperturbed aggregate images are obtainable [65, 304-306].

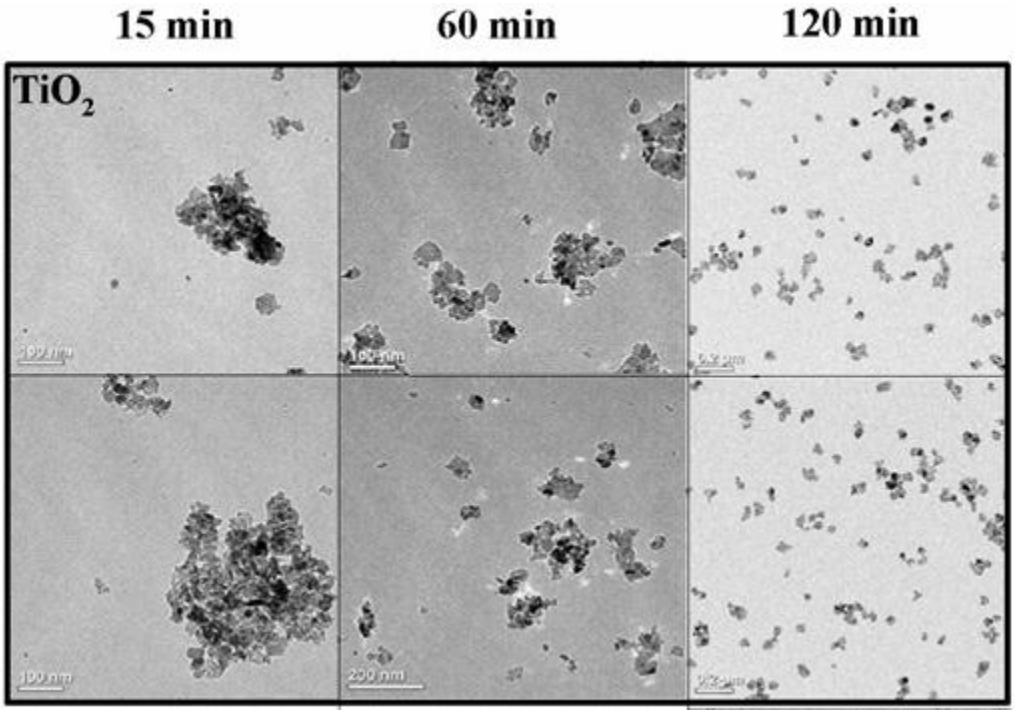

Figure 6.5. TEM images of titania (TiO_2) nanoparticles after selected milling times.

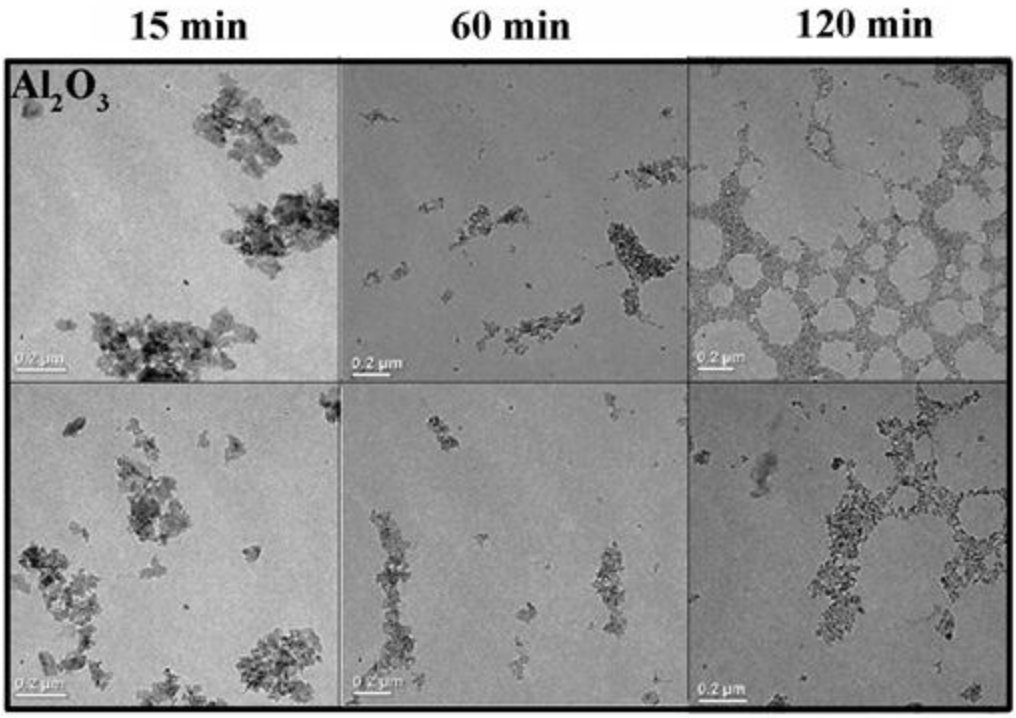

Figure 6.6 TEM images of alumina (Al_2O_3) nanoparticles after selected milling times.

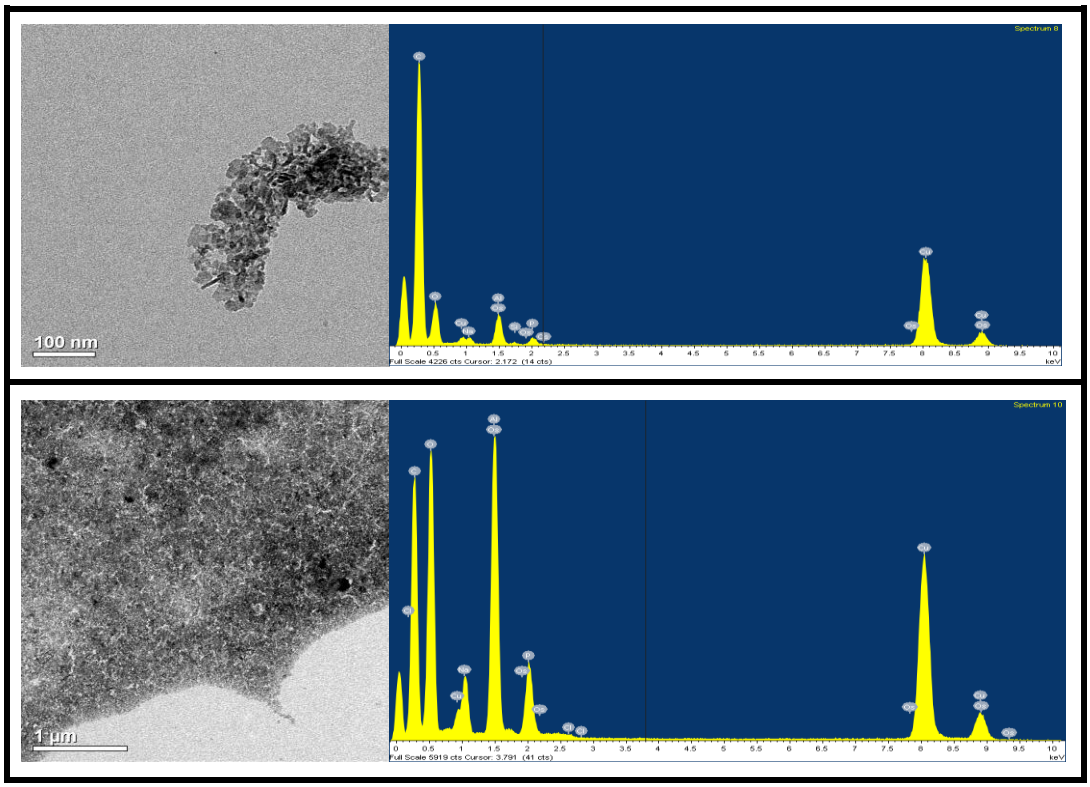

Figure 6.7. EDS analysis of Al_2O_3 aggregates in a 60 min milling sample (individual aggregate-top, highly concentrated aggregates-bottom)

6.3.3 Quasifractal aggregate analysis

With TEM images likely influenced by drying and with the characteristic sizes of aggregates analyzed often in the sub-100 nm range (well below the wavelengths of visible light), we utilize an alternative to infer the structures of aggregates in suspension, which we have also recently employed in the examination of iron oxide nanoparticle aggregates [306]. For structural characterization, we approximate all aggregates as quasifractal structures, approximately obeying the scaling law [307, 308]:

$$N_p = k_f\left(\frac{R_g}{a_p}\right)^{D_f} \tag{6.3}$$

where N_p is the number of primary particles in an aggregate, k_f is the pre-exponential factor, typically in the range from 1.0 to 2.0, a_p is the primary particle radius, R_g is the aggregate's radius of gyration, and D_f is the fractal dimension which can theoretically vary from 1.0 to 3.0.

For each suspension, we infer k_f and D_f at different milling times; we assume these two parameters apply approximately to all aggregates, while there is a distribution in N_p. This assumption is based upon prior examinations of aggregates formed via collisions [309]. Inference of k_f and D_f is carried out as follows: We directly determine the average primary particle radius for alumina and titania particles via direct measurements of primary particles for each material. Milling was not found to change the primary particle size for either material, and mean values of $a_p = 8.25\ nm$ and $a_p = 7.20\ nm$ are obtained for titania and alumina particles, respectively. Complete primary particle radius histograms are provided Figure 6.8. To compare measured hydrodynamic radii distribution function and

intrinsic viscosities to the expected values for quasifractal aggregates we computationally generate 10-20 quasifractal aggregates of prescribed k_f, D_f, and N_p using the cluster-cluster algorithm described by Filippov et al [63] for $1.5 \leq D_f \leq 2.7$, $k_f = 1.2$, 1.3, 1.5, and 1.7, and $4 \leq N_p \leq 1000$. Similarly, for $D_f = 1.3$ & 2.9, with the same k_f and N_p ranges, we generate 10 quasifractal aggregates using the sequential algorithm (also described by Filippov et al).

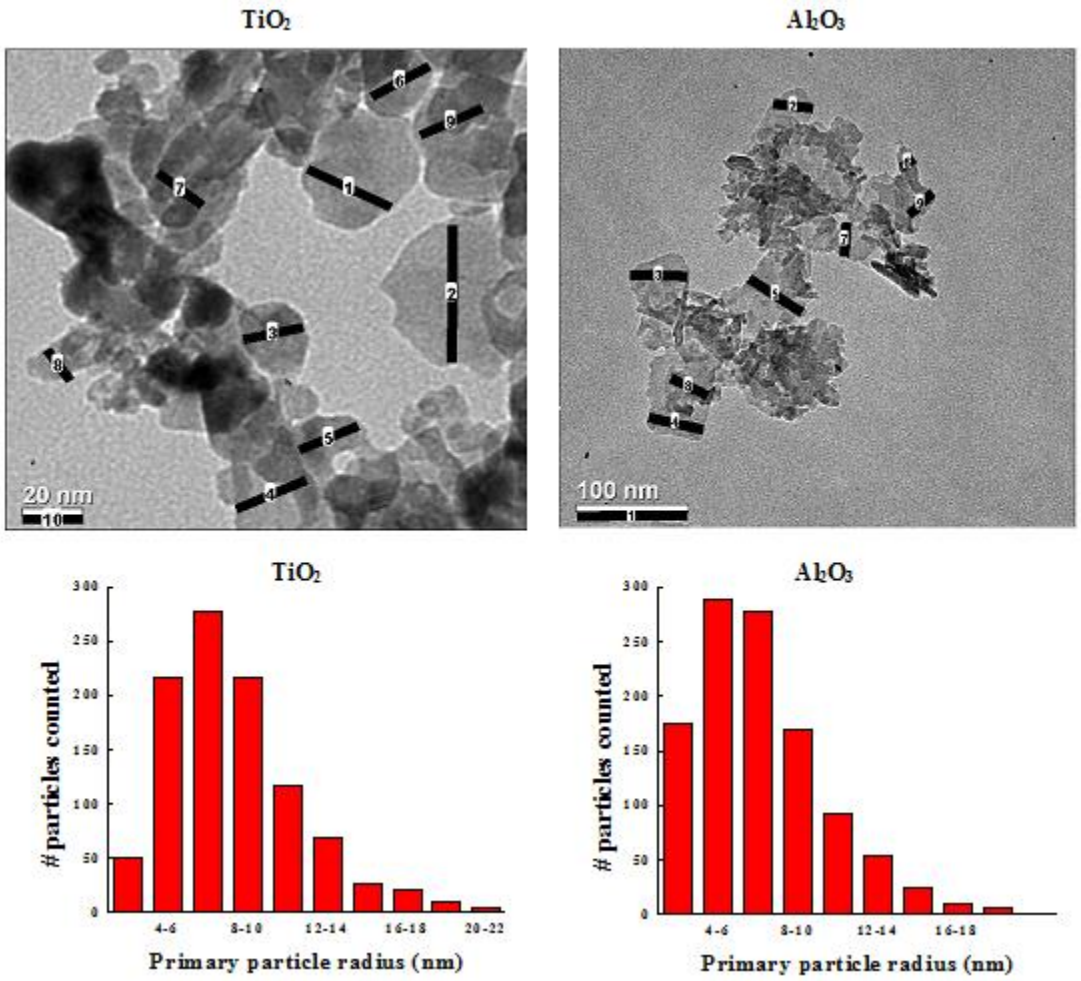

Figure 6.8. Sample TEM images of titania and alumina aggregates, as well as histograms of the primary particle radius distributions.

Sample structures with N_p = 20, 100, & 200, and selected k_f and D_f values are depicted in Figure 6.9. For each simulated aggregate we compute the ratio of the hydrodynamic radius to the primary particle radius (R_H/a_p), by invoking the Hubbard-Douglas approximation [310] (i.e. equating the orientationally averaged hydrodynamic radius with a diffusion limited collision radius) and specifically using the Monte-Carlo algorithm provided in the supplemental information of Gopalakrishnan et al [258] to infer the average value of R_H/a_p (for all aggregates with the same quasifractal descriptors) as a function of k_f, D_f, and N_p. For k_f = 2.0 and selected D_f values the calculated R_H/a_p versus N_p relationships are plotted if Figure 6.10 (a). Such curves are observed to be near log-linear; however, as noted elsewhere [311, 312] for most k_f and D_f combinations N_p does not scale with $(\frac{R_H}{a_p})^{D_f}$, i.e. the scaling in equation (2) only applies for the radius of gyration. Similarly, we use Monte Carlo algorithms based on those described by Mansfield and coworkers [298] and which we have applied previously [288] to determine the intrinsic viscosity for each simulated aggregate, and hence express the intrinsic viscosity as a function of k_f, D_f, and N_p (denoted as $[\eta]_{k_f,D_f,N_p}$ to distinguish calculated values from those determined through measurements). Again for k_f = 2.0 and selected D_f values, these relationships are plotted in Figure 6.10 (b). The intrinsic viscosity is observed to be extremely dependent on aggregate morphology, increasing drastically with both increasing number of primary particles and decreasing fractal dimension.

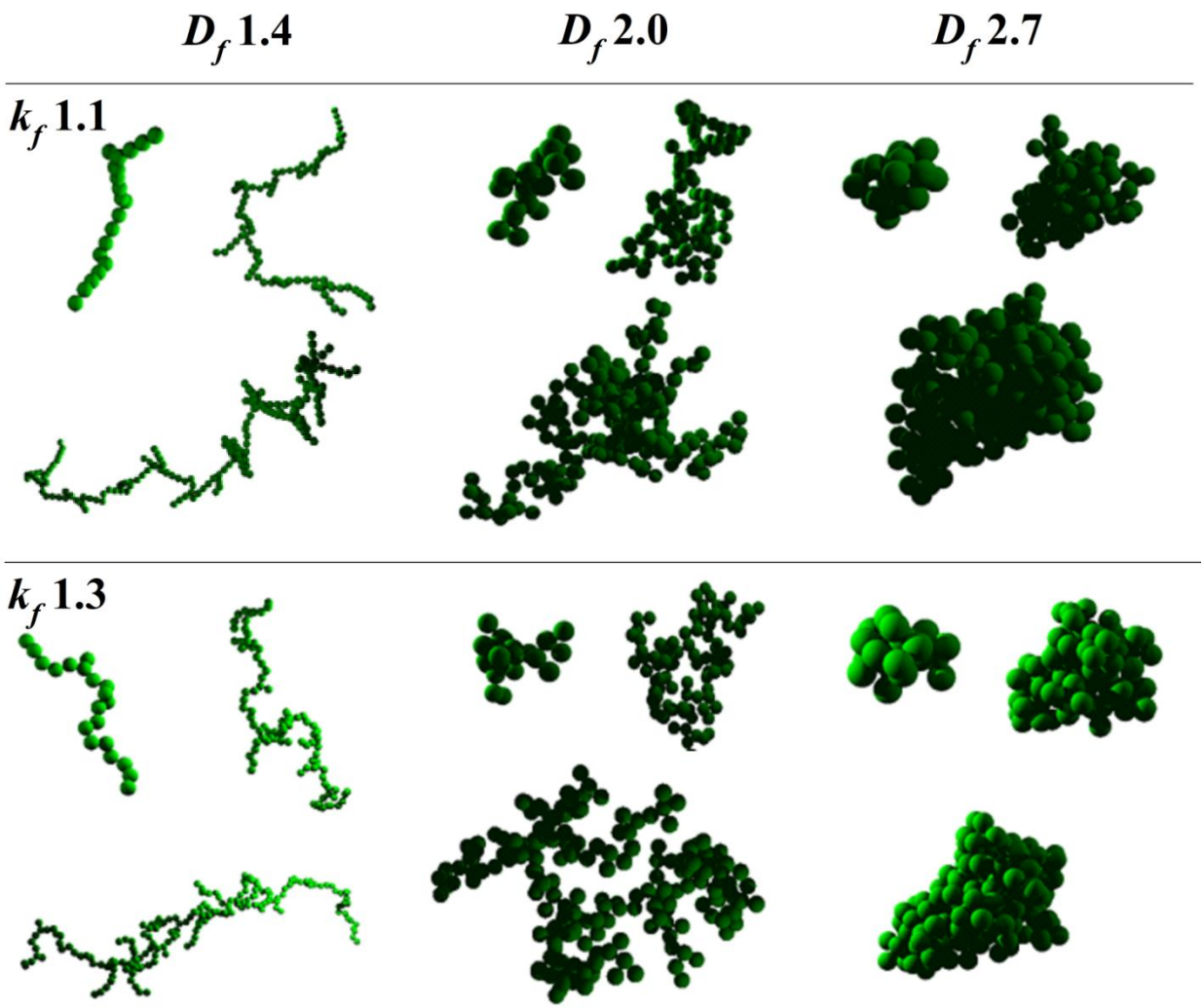

Figure 6.9. Depictions of computational generated quasifractal aggregates composed of 20, 100, & 200 monodisperse primary particles, with prescribed pre-exponential factors (k_f) and fractal dimensions (D_f). Such structures are used to develop functional relationships linking quasifractal descriptors to the hydrodynamic radius and intrinsic viscosity.

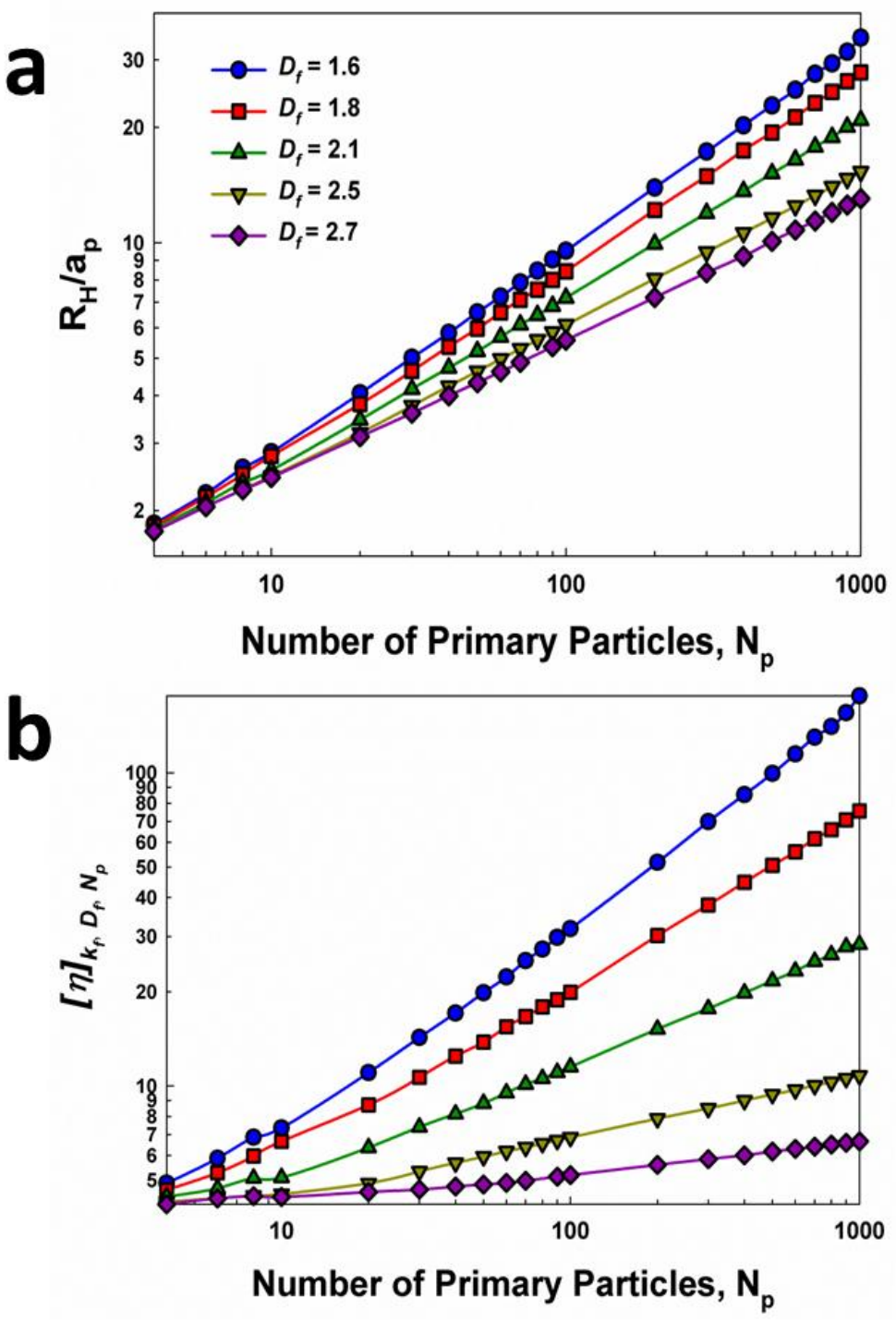

Figure 6.10. The ratio of aggregate hydrodynamic radii to primary particle radii *(R_H/a_p)* **(a.)** and intrinsic viscosities **(b.)** as functions of the number of primary particles per aggregate, for selected fractal dimensions and k_f = 2.0. Functional relationships were established by computationally generating aggregates with prescribed quasifractal descriptors and directly calculating hydrodynamic radii and intrinsic viscosities for each generated structure.

For each sample, from experiments we obtained an intrinsic viscosity, as well as a list of observed values for R_H/a_p, where a_p is the mean primary particle radius. By assuming a specific k_f and D_f for a given suspension and milling time, using relationships such as those shown in Figure 6.10 (a), R_H/a_p values are converted to N_p values, and additionally a value for $[\eta]_{k_f,D_f,N_p}$ is obtained using relationships such as those in Figure 6.10 (b). For the assumed D_f and k_f, an average intrinsic viscosity for the sample (denoted $[\eta]_{k_f,D_f}$) is then calculated using the equation:

$$[\eta]_{k_f,D_f} = \frac{\sum_{j=1}^{j=m} N_{p,j}[\eta_j]_{k_f,D_f,N_p}}{\sum_{j=1}^{j=m} N_{p,j}} \tag{6.4}$$

where the subscript j denotes the properties for the j^{th} aggregate observed in NTA analysis, wherein m total aggregates were observed. Equation (6.4) is used with 85 distinct k_f, D_f pairs. A relative probability ($\mathrm{P}(D_f, k_f)$) that a particular k_f, D_f pair appropriately describes aggregates in a suspension is calculated as:

$$\mathrm{P}(D_f, k_f) = \exp\left(-\left[[\eta]_{k_f,D_f} - [\eta]\right]^2\right) \tag{6.5}$$

Contour plots of P-values at various milling times are shown in Figures 6.11 and 12 for titania and alumina, respectively. In all plots, $[\eta]$ values were calculated from equation (6.2), i.e. including a Huggins coefficient of 1.0. P-values near unity indicate that the k_f, D_f pair in question fits well the measured aggregates. Early in the milling process (after 15 minutes), measurements of alumina and titania aggregates suggest that aggregates are

extremely dense; the highest P-values are obtained for k_f of 2.0 and D_f of 2.9. That the P-values are extremely low for all cases for alumina at 15 minutes suggestions that the quasifractal model may not be an appropriate way to describe aggregates initially.

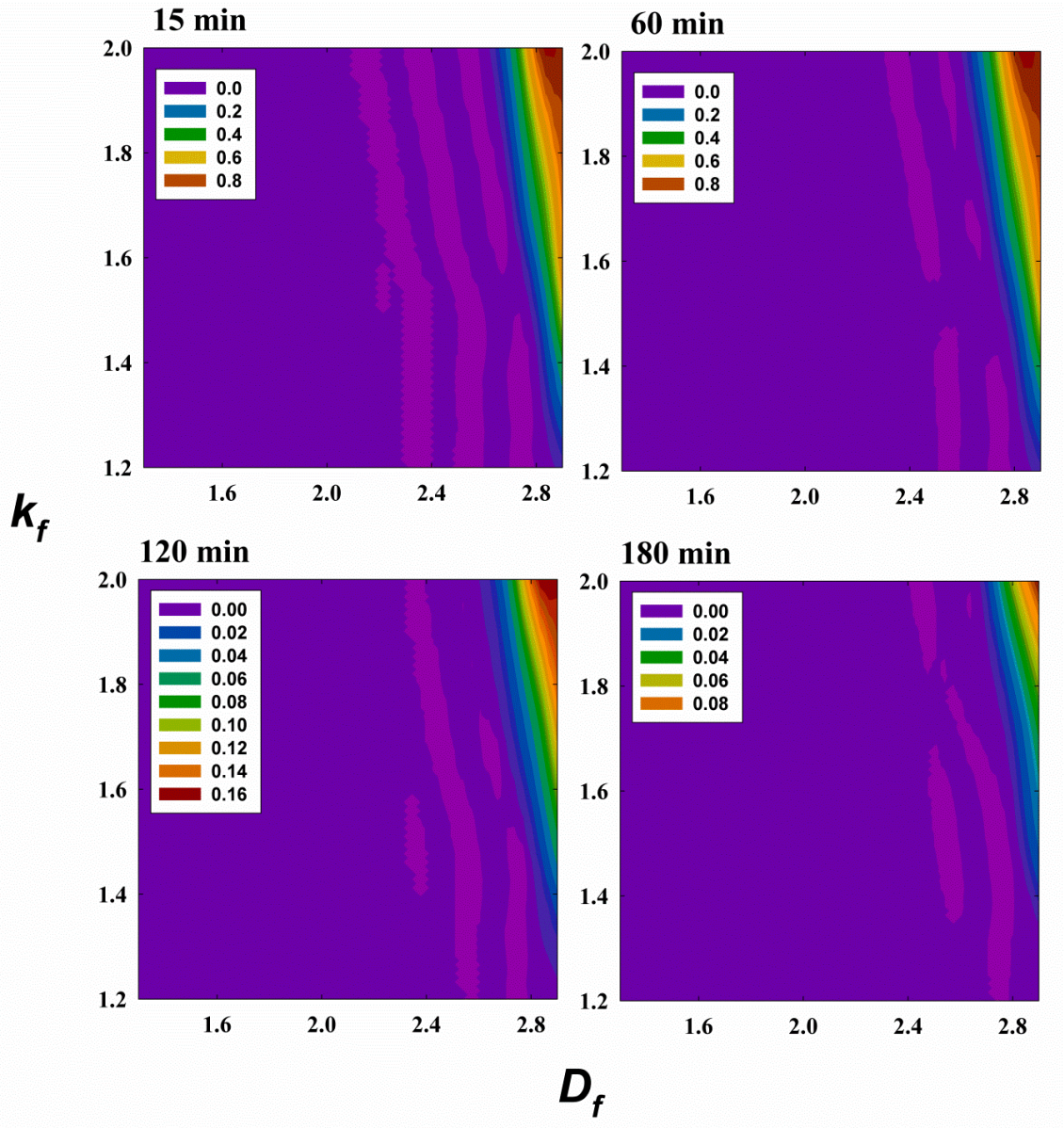

Figure 6.11. Contour plots displaying P-values (equation 4) as functions of k_f and D_f for titania aggregates in milled suspensions.

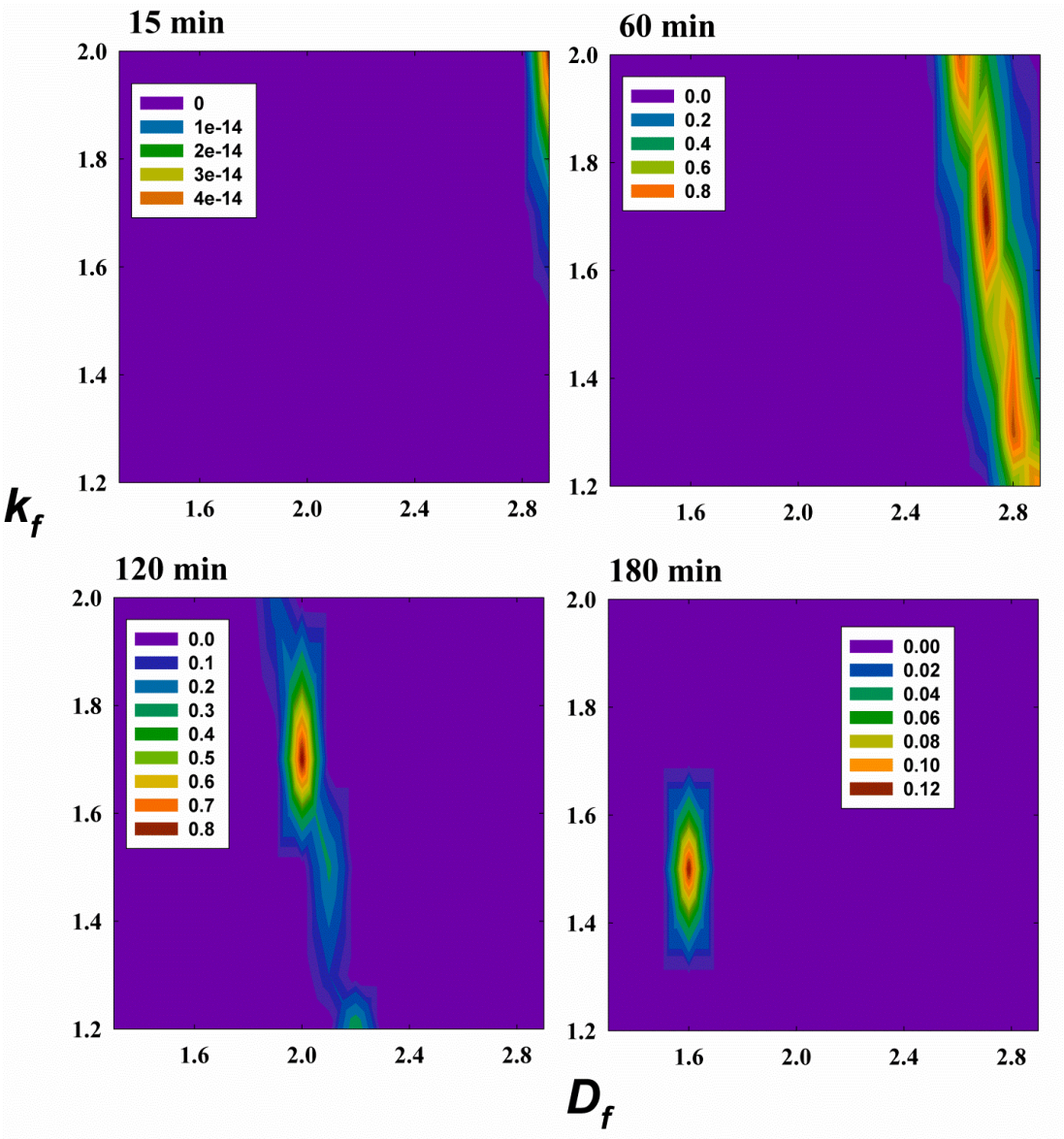

Figure 6.12. Contour plots displaying P-values (equation 4) as functions of k_f and D_f for alumina aggregates in milled suspensions.

As milling proceeds, for the titania aggregates, high pre-exponential factor, high fractal dimensions are consistently found to agree best with experimental measurements. This suggests that in the case of titania, milling serves to break aggregates, and the fragmentation products also adopt compact structures. Conversely, for the alumina aggregates, contour plots show clearly that as milling proceeds, progressively smaller

fractal dimensions lead to the best agreement with experimental measurements (note, although k_f varies in a non-monotonic manner, we find that k_f does not influence aggregate hydrodynamic radii and intrinsic viscosities to the extent that D_f does). After 180 minutes, alumina aggregates appear to have fractal dimensions near 1.6, which are highly chain-like structures, which, with less than 100 primary particles, can have an intrinsic viscosity an order of magnitude higher than spherical particles.

In total, quasifractal analysis appears to explain well how the alumina suspension viscosity can increase with milling time while hydrodynamic radius distribution functions shift to smaller sizes. Using the most probable k_f, D_f pairs in Figures 6.11 and 12, we now transform hydrodynamic radius distribution functions in Figure 6.2 to express measured distributions in terms of the number of primary particles per aggregate (i.e. using the established link between R_H/a_p and N_p for a prescribed k_f and D_f), with results plotted in Figure 6.13. Clearly evident for both materials is that milling does lead to a reduction in the numbers of primary particles in aggregates; simply in the case of titania little aggregate restructuring occurs, while in the case of alumina, restructuring (or finite reaggregation leading to different morphologies than the morphologies of the original aggregates) is significant. To our knowledge, this finding has not been reported previously, though drastic increases in alumina suspension viscosities brought about by the formation of chain-like aggregates have been observed previously [313].

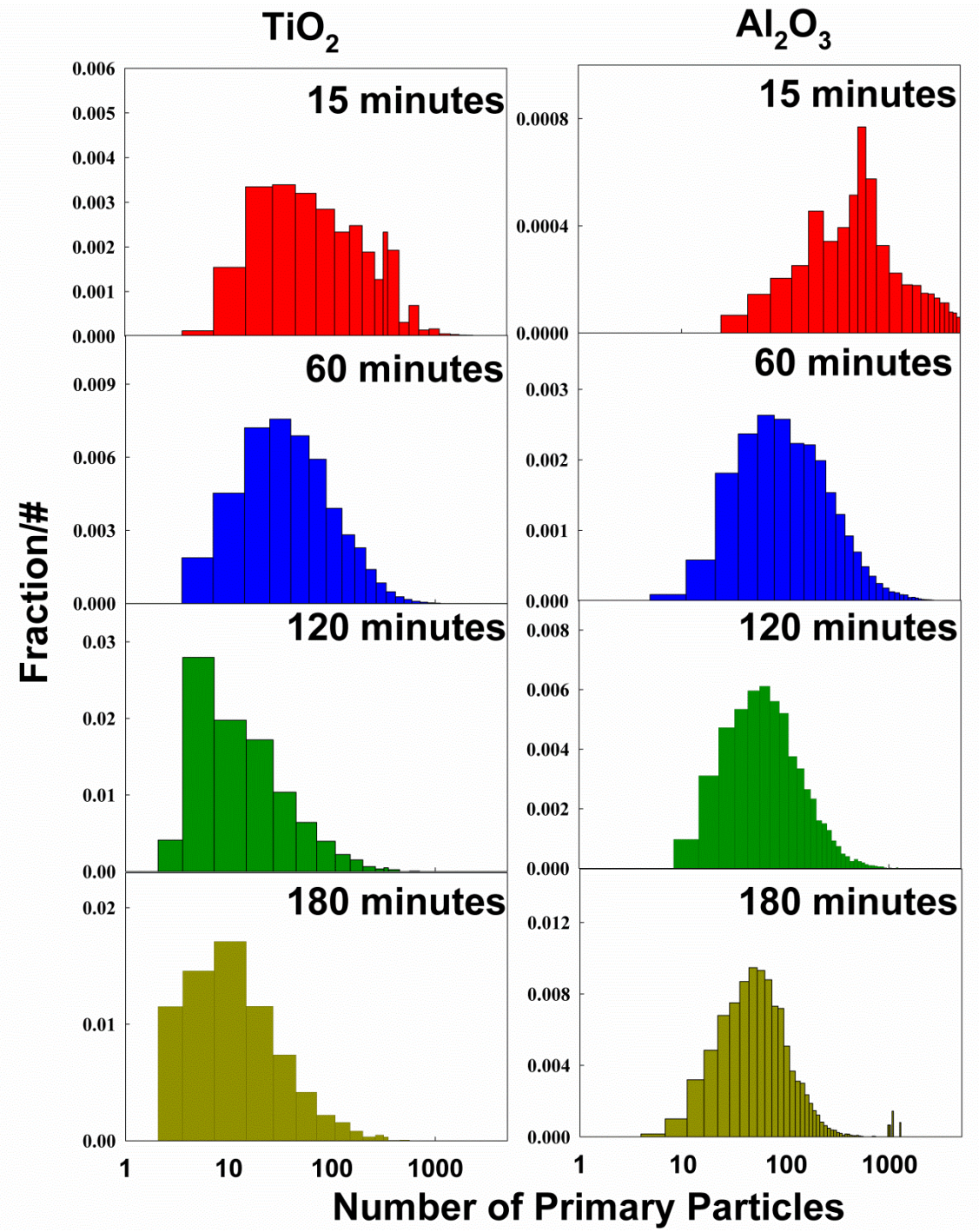

Figure 6.13. The results of NTA analysis recast in terms of the number of primary particles per aggregate.

6.4 Conclusions

We use a combination of nanoparticle tracking analysis, viscosity measurements, and quasifractal modeling to analyze the change in morphology of aggregates undergoing wet milling. Based on this combination of experiments and computations, we conclude the following:

1. Wet milling is found to breakdown nanoparticle aggregates into progressively smaller structures for both titania and alumina. However, analysis suggests that milling simultaneously leads to alumina aggregate restructuring and fragmentation, while does not lead to any restructuring for titania. Such conclusions only apply to the test case examined here (using the noted surfactant and nanoparticle volume fractions); the analysis performed is intended to demonstrate how aggregate structural analysis can be performed, but does not allow us to describe universally how aggregate morphology evolves during wet milling. Further, this work does not elucidate whether the change in alumina aggregate morphology is caused directly in the mill vessel (directly by bead grinding), or is brought about by reaggregation post-milling.
2. While normally only size distribution analysis is performed during wet milling to monitor the process, viscosity measurements are found to yield orthogonal information, as an increase in intrinsic viscosity suggests there is also a change in aggregate structure brought about by milling. However, a modest decrease in aggregate intrinsic viscosity does not necessarily imply aggregate structure is changing beyond a reduction in the number of primary particles per aggregate.

3. The quasifractal analysis procedure developed, in which NTA and viscosity measurements are used to infer the most probable k_f, D_f pair for a suspension, is not limited to the analysis of wet-milled suspensions, and may prove useful in other instances when aggregates are difficult to analyze by static light scattering or other techniques. The method can be applied when suspensions have Newtonian behavior, have sufficiently low volume fraction, and remain stable under viscosity measurements (i.e. do not aggregate orthokinetically).

Chapter 7 Conclusion

The five studies described herein emphasize the importance of the physical structures of nanomaterials and nanomaterial aggregates on their behavior in biological and environmental systems, and serve as demonstrations of new techniques to quantitatively analyze nanomaterial morphology. Specifically, liquid nebulization coupled with ion mobility spectrometry (LN-IMS), introduced in Chapter 2 enables accurate size measurements of sub 30 nm polydisperse particles, which are difficult to perform by conventional techniques. The universal calibration curve developed also indicates that LN-IMS can be used to measure colloidal particle concentrations directly, without the need for particle-specific calibration techniques. The capabilities of LN-IMS additionally enable size shifts of nanoparticles upon interacting with small molecule or macromolecule, as demonstrated in Chapters 3 and 4. Ideally, LN-IMS will find utility as a general technique to both characterize nanomaterial size distribution functions or a variety of nanomaterial chemistries, and additionally to quantify the extent of ligand binding to nanomaterials.

As the extension of Chapter 4, the extent of aggregation of SPIONs via endocytosis of human prostate cancer cells was quantified and its influence on SAR was investigated in Chapter 5. With the fractal aggregate model based image processing technique, three dimensional structures of SPION aggregates in intra- and extra- cellular matrices were inferred from two dimensional microscopy images. A significant fraction of intracellular SPION aggregates are composed of more than 10^3 primary particles, and the Metropolis inversion algorithm combined with SAR and NTA measurements revealed that SARs of SPIONs in these super aggregates are below 100 W/gFe. Superaggregate formation in intracellular structures should hence be avoided in order for the better SPION hyperthermia

applications in clinical therapies. As suggested in Chapter 4, SPION surface functionalization is one of ways to mitigate super-aggregation of SPIONs in cellular environments.

In addition to the image processing technique, the ensemble method introduced in Chapter 6 enables inference of the fractal descriptors of an entire aggregate population from their transport properties, namely the intrinsic viscosities and hydrodynamic radius distribution function. With the developed data inversion process, morphological changes of titania and alumina aggregates during the wet mil process were quantified. Morphological characterization helps to explain why an alumina nanosuspension can become more viscous while a titania nanosuspension exhibited reduced viscosity over the course of milling, even if the hydrodynamic sizes of both materials decreased with milling time.

The studies completed and described here fall broadly within the subdispline of nanomaterial analysis, which is an interdisciplinary topic at the interfaces of chemistry, engineering, and physics. Largely, the advances made deal with quantitation of nanomaterial polydispersity and morphological heterogeneity. Quite often, in controlled studies of the behavior of nanomaterials, researchers seek to avoid both polydispersity and heterogeneity, largely because those have been difficult to quantify. Therefore, it is my hope that the techniques applied in this dissertation will find application as characterization techniques in studies focusing on nanomaterial performance (i.e. nanoparticle catalytic activity, or plasmonic properties). Furthermore, the methods and techniques proposed and developed can be further modified for more detailed analyses. The LN-IMS system can in principle be coupled with inductively coupled plasma mass spectrometry (ICP-MS) or with

aerosol particle mass (APM) analysis; such coupled systems would provide size resolved atomic composition or two dimensional size and mass distributions, respectively. Moreover, in the combination with the Langmuir-like adsorption model, LN-IMS can be employed to quantify binding of polymers, natural organic matter or other ligand molecules on nanomaterials in complex environmental. The presented image processing technique can be used to infer aggregate structures of any nanoparticles in a variety of other systems, including natural water bodies or in wastewater treatment systems. In total, I believe that the presented techniques make possible new ways to quantify nanomaterial size and shape distributions, which should help in developing structure-function relationships in nanoscale systems.

References

1. Mu, L. and R.L. Sprando, *Application of Nanotechnology in Cosmetics.* Pharmaceutical Research, 2010. **27**(8): p. 1746-1749.
2. Lewicka, Z.A., et al., *The structure, composition, and dimensions of TiO2 and ZnO nanomaterials in commercial sunscreens.* Journal of Nanoparticle Research, 2011. **13**(9): p. 3607-3617.
3. Macwan, D.P., P.N. Dave, and S. Chaturvedi, *A review on nano-TiO2 sol-gel type syntheses and its applications.* Journal of Materials Science, 2011. **46**(11): p. 3669-3686.
4. Cushen, M., et al., *Nanotechnologies in the food industry - Recent developments, risks and regulation.* Trends in Food Science & Technology, 2012. **24**(1): p. 30-46.
5. Rashidi, L. and K. Khosravi-Darani, *The Applications of Nanotechnology in Food Industry.* Critical Reviews in Food Science and Nutrition, 2011. **51**(8): p. 723-730.
6. Gelperina, S., et al., *The potential advantages of nanoparticle drug delivery systems in chemotherapy of tuberculosis.* American Journal of Respiratory and Critical Care Medicine, 2005. **172**(12): p. 1487-1490.
7. De Jong, W.H. and P.J.A. Borm, *Drug delivery and nanoparticles: Applications and hazards.* International Journal of Nanomedicine, 2008. **3**(2): p. 133-149.
8. Mudshinge, S.R., et al., *Nanoparticles: Emerging carriers for drug delivery.* Saudi Pharmaceutical Journal, 2011. **19**(3): p. 129-141.
9. Kulkarni, D.P., et al., *Application of aluminum oxide nanofluids in diesel electric generator as jacket water coolant.* Applied Thermal Engineering, 2008. **28**(14-15): p. 1774-1781.
10. De, M., P.S. Ghosh, and V.M. Rotello, *Applications of Nanoparticles in Biology.* Advanced Materials, 2008. **20**(22): p. 4225-4241.
11. Peer, D., et al., *Nanocarriers as an emerging platform for cancer therapy.* Nature Nanotechnology, 2007. **2**(12): p. 751-760.
12. Wang, A.Z., R. Langer, and O.C. Farokhzad, *Nanoparticle Delivery of Cancer Drugs.* Annual Review of Medicine, Vol 63, 2012. **63**: p. 185-198.

13. Davis, M.E., Z. Chen, and D.M. Shin, *Nanoparticle therapeutics: an emerging treatment modality for cancer*. Nature Reviews Drug Discovery, 2008. **7**(9): p. 771-782.
14. Shipway, A.N., E. Katz, and I. Willner, *Nanoparticle arrays on surfaces for electronic, optical, and sensor applications.* Chemphyschem, 2000. **1**(1): p. 18-52.
15. Luo, X.L., et al., *Application of nanoparticles in electrochemical sensors and biosensors.* Electroanalysis, 2006. **18**(4): p. 319-326.
16. Albanese, A., P.S. Tang, and W.C.W. Chan, *The Effect of Nanoparticle Size, Shape, and Surface Chemistry on Biological Systems.* Annual Review of Biomedical Engineering, Vol 14, 2012. **14**: p. 1-16.
17. Xia, L., et al., *Naturally occurring nanoparticles from English ivy: an alternative to metal-based nanoparticles for UV protection.* Journal of Nanobiotechnology, 2010. **8**: p. 12-Article No.: 12.
18. Xu, R., et al., *Shape-dependent catalytic activity of silver nanoparticles for the oxidation of styrene.* Chemistry-an Asian Journal, 2006. **1**(6): p. 888-893.
19. Rudyak, V.Y. and S.L. Krasnolutskii, *Methods of measuring the diffusion coefficient and sizes of nanoparticles in a rarefied gas.* Doklady Physics, 2002. **47**(10): p. 758-761.
20. Pecora, R., *Dynamic light scattering measurement of nanometer particles in liquids.* Journal of Nanoparticle Research, 2000. **2**(2): p. 123-131.
21. Jin, H., et al., *Size-Dependent Cellular Uptake and Expulsion of Single-Walled Carbon Nanotubes: Single Particle Tracking and a Generic Uptake Model for Nanoparticles.* Acs Nano, 2009. **3**(1): p. 149-158.
22. Chithrani, B.D., A.A. Ghazani, and W.C.W. Chan, *Determining the size and shape dependence of gold nanoparticle uptake into mammalian cells.* Nano Letters, 2006. **6**(4): p. 662-668.
23. Arvizo, R., R. Bhattacharya, and P. Mukherjee, *Gold nanoparticles: opportunities and challenges in nanomedicine.* Expert Opinion on Drug Delivery, 2010. **7**(6): p. 753-763.
24. Euliss, L.E., et al., *Imparting size, shape, and composition control of materials for nanomedicine.* Chemical Society Reviews, 2006. **35**(11): p. 1095-1104.

25. Wang, S., et al., *Challenge in understanding size and shape dependent toxicity of gold nanomaterials in human skin keratinocytes.* Chemical Physics Letters, 2008. **463**(1-3): p. 145-149.
26. Kvitek, L., et al., *Effect of surfactants and polymers on stability and antibacterial activity of silver nanoparticles (NPs).* Journal of Physical Chemistry C, 2008. **112**(15): p. 5825-5834.
27. Johnson, S.R., S.D. Evans, and R. Brydson, *Influence of a terminal functionality on the physical properties of surfactant-stabilized gold nanoparticles.* Langmuir, 1998. **14**(23): p. 6639-6647.
28. Jiang, J., G. Oberdorster, and P. Biswas, *Characterization of size, surface charge, and agglomeration state of nanoparticle dispersions for toxicological studies.* Journal of Nanoparticle Research, 2009. **11**(1): p. 77-89.
29. Christian, P., et al., *Nanoparticles: structure, properties, preparation and behaviour in environmental media.* Ecotoxicology, 2008. **17**(5): p. 326-343.
30. El Badawy, A.M., et al., *Impact of Environmental Conditions (pH, Ionic Strength, and Electrolyte Type) on the Surface Charge and Aggregation of Silver Nanoparticles Suspensions.* Environmental Science & Technology, 2010. **44**(4): p. 1260-1266.
31. French, R.A., et al., *Influence of Ionic Strength, pH, and Cation Valence on Aggregation Kinetics of Titanium Dioxide Nanoparticles.* Environmental Science & Technology, 2009. **43**(5): p. 1354-1359.
32. Hotze, E.M., T. Phenrat, and G.V. Lowry, *Nanoparticle Aggregation: Challenges to Understanding Transport and Reactivity in the Environment.* Journal of Environmental Quality, 2010. **39**(6): p. 1909-1924.
33. Nowack, B. and T.D. Bucheli, *Occurrence, behavior and effects of nanoparticles in the environment.* Environmental Pollution, 2007. **150**(1): p. 5-22.
34. Lynch, I. and K.A. Dawson, *Protein-nanoparticle interactions.* Nano Today, 2008. **3**(1-2): p. 40-47.
35. Mahmoudi, M., et al., *Protein-Nanoparticle Interactions: Opportunities and Challenges.* Chemical Reviews, 2011. **111**(9): p. 5610-5637.

36. Pettibone, J.M., et al., *Adsorption of organic acids on TiO2 nanoparticles: Effects of pH, nanoparticle size, and nanoparticle aggregation.* Langmuir, 2008. **24**(13): p. 6659-6667.
37. Bootz, A., et al., *Comparison of scanning electron microscopy, dynamic light scattering and analytical ultracentrifugation for the sizing of poly(butyl cyanoacrylate) nanoparticles.* European Journal of Pharmaceutics and Biopharmaceutics, 2004. **57**(2): p. 369-375.
38. Hoo, C.M., et al., *A comparison of atomic force microscopy (AFM) and dynamic light scattering (DLS) methods to characterize nanoparticle size distributions.* Journal of Nanoparticle Research, 2008. **10**: p. 89-96.
39. Ito, T., et al., *Comparison of nanoparticle size and electrophoretic mobility measurements using a carbon-nanotube-based coulter counter, dynamic light scattering, transmission electron microscopy, and phase analysis light scattering.* Langmuir, 2004. **20**(16): p. 6940-6945.
40. Jans, H., et al., *Dynamic Light Scattering as a Powerful Tool for Gold Nanoparticle Bioconjugation and Biomolecular Binding Studies.* Analytical Chemistry, 2009. **81**(22): p. 9425-9432.
41. Murdock, R.C., et al., *Characterization of nanomaterial dispersion in solution prior to In vitro exposure using dynamic light scattering technique.* Toxicological Sciences, 2008. **101**(2): p. 239-253.
42. Gebhardt, R., et al., *Size distribution of pressure-decomposed casein micelles studied by dynamic light scattering and AFM.* European Biophysics Journal with Biophysics Letters, 2006. **35**(6): p. 503-509.
43. Filipe, V., A. Hawe, and W. Jiskoot, *Critical Evaluation of Nanoparticle Tracking Analysis (NTA) by NanoSight for the Measurement of Nanoparticles and Protein Aggregates.* Pharmaceutical Research, 2010. **27**(5): p. 796-810.
44. Malloy, A. and B. Carr, *Nanoparticle tracking analysis - The Halo (TM) system.* Particle & Particle Systems Characterization, 2006. **23**(2): p. 197-204.
45. Montes-Burgos, I., et al., *Characterisation of nanoparticle size and state prior to nanotoxicological studies.* Journal of Nanoparticle Research, 2010. **12**(1): p. 47-53.

46. Axson, J.L., et al., *An In Situ Method for Sizing Insoluble Residues in Precipitation and Other Aqueous Samples.* Aerosol Science and Technology, 2015. **49**(1): p. 24-34.
47. Yang, D.T., et al., *Evaluation of nanoparticle tracking for characterization of fibrillar protein aggregates.* Aiche Journal, 2014. **60**(4): p. 1236-1244.
48. Gallego-Urrea, J.A., et al., *Measurements of nanoparticle number concentrations and size distributions in contrasting aquatic environments using nanoparticle tracking analysis.* Environmental Chemistry, 2010. **7**(1): p. 67-81.
49. Farkas, J., et al., *Uptake and effects of manufactured silver nanoparticles in rainbow trout (Oncorhynchus mykiss) gill cells.* Aquatic Toxicology, 2011. **101**(1): p. 117-125.
50. Fernandez De La Mora, J., et al., *Differential mobility analysis of molecular ions and nanometer particles.* Trends in Analytical Chemistry, 1998. **17**(6): p. 328-339.
51. Kousaka, Y., K. Okuyama, and M. Adachi, *DETERMINATION OF PARTICLE-SIZE DISTRIBUTION OF ULTRA-FINE AEROSOLS USING A DIFFERENTIAL MOBILITY ANALYZER.* Aerosol Science and Technology, 1985. **4**(2): p. 209-225.
52. Chen, D.R., et al., *Design and evaluation of a nanometer aerosol differential mobility analyzer (Nano-DMA).* Journal of Aerosol Science, 1998. **29**(5-6): p. 497-509.
53. Stolzenburg, M.R. and P.H. Mcmurry, *An Ultrafine Aerosol Condensation Nucleus Counter.* Aerosol Science and Technology, 1991. **14**(1): p. 48-65.
54. McMurry, P.H., *The history of condensation nucleus counters.* Aerosol Science and Technology, 2000. **33**(4): p. 297-322.
55. Wilson, J.C., *AEROSOL TECHNOLOGY - PROPERTIES, BEHAVIOR, AND MEASUREMENT OF AIRBORNE PARTICLES - HINDS,WC.* American Scientist, 1983. **71**(4): p. 430-431.
56. Friedlander, S.K., *Smoke, dust and haze: fundamentals of aerosol dynamics*. 2000, New York: Oxford University Press.
57. Wiedensohler, A., et al., *Mobility particle size spectrometers: harmonization of technical standards and data structure to facilitate high quality long-term*

observations of atmospheric particle number size distributions. Atmospheric Measurement Techniques, 2012. **5**(3): p. 657-685.

58. Pfeifer, S., et al., *A fast and easy-to-implement inversion algorithm for mobility particle size spectrometers considering particle number size distribution information outside of the detection range.* Atmospheric Measurement Techniques, 2014. **7**(1): p. 95-105.
59. Mahurin, S.M. and M.-D. Cheng, *Generating nanoscale aggregates from colloidal nanoparticles by various aerosol spray techniques.* Nanotoxicology, 2007. **1**(2): p. 130-138.
60. Lenggoro, I.W., et al., *Colloidal nanoparticle analysis by nanoelectrospray size spectrometry with a heated flow.* Analytica Chimica Acta, 2007. **585**(2): p. 193-201.
61. deJuan, L. and J.F. delaMora, *On-line sizing of colloidal nanoparticles via electrospray and aerosol techniques.* Nanotechnology: Molecularly Designed Materials, 1996. **622**: p. 20-41.
62. Fissan, H., et al., *Comparison of different characterization methods for nanoparticle dispersions before and after aerosolization.* Analytical Methods, 2014. **6**(18): p. 7324-7334.
63. Filippov, A.V., M. Zurita, and D.E. Rosner, *Fractal-like Aggregates: Relation between Morphology and Physical Properties.* Journal of Colloid and Interface Science, 2000. **229**(1): p. 261-273.
64. Sorensen, C.M. and G.C. Roberts, *The prefactor of fractal aggregates.* Journal of Colloid and Interface Science, 1997. **186**(2): p. 447-452.
65. Brasil, A.M., T.L. Farias, and M.G. Carvalho, *A recipe for image characterization of fractal-like aggregates.* Journal of Aerosol Science, 1999. **30**(10): p. 1379-1389.
66. Gwaze, P., et al., *Comparison of three methods of fractal analysis applied to soot aggregates from wood combustion.* Journal of Aerosol Science, 2006. **37**(7): p. 820-838.
67. Lee, C. and T.A. Kramer, *Prediction of three-dimensional fractal dimensions using the two-dimensional properties of fractal aggregates.* Advances in Colloid and Interface Science, 2004. **112**(1-3): p. 49-57.

68. Chakrabarty, R.K., et al., *Simulation of Aggregates with Point-Contacting Monomers in the Cluster-Dilute Regime. Part 1: Determining the Most Reliable Technique for Obtaining Three-Dimensional Fractal Dimension from Two-Dimensional Images.* Aerosol Science and Technology, 2011. **45**(1): p. 75-80.
69. Chakrabarty, R.K., et al., *Simulation of Aggregates with Point-Contacting Monomers in the Cluster-Dilute Regime. Part 2: Comparison of Two- and Three-Dimensional Structural Properties as a Function of Fractal Dimension.* Aerosol Science and Technology, 2011. **45**(8): p. 903-908.
70. Voisin, C., et al., *Ultrafast electron dynamics and optical nonlinearities in metal nanoparticles.* Journal of Physical Chemistry B, 2001. **105**(12): p. 2264-2280.
71. Nirmal, M. and L. Brus, *Luminescence photophysics in semiconductor nanocrystals.* Accounts of Chemical Research, 1999. **32**(5): p. 407-414.
72. Daniel, M.C. and D. Astruc, *Gold nanoparticles: Assembly, supramolecular chemistry, quantum-size-related properties, and applications toward biology, catalysis, and nanotechnology.* Chemical Reviews, 2004. **104**(1): p. 293-346.
73. Astruc, D., F. Lu, and J.R. Aranzaes, *Nanoparticles as recyclable catalysts: The frontier between homogeneous and heterogeneous catalysis.* Angewandte Chemie-International Edition, 2005. **44**(48): p. 7852-7872.
74. Hinterwirth, H., et al., *Comparative method evaluation for size and size-distribution analysis of gold nanoparticles.* Journal of Separation Science, 2013. **36**(17): p. 2952-2961.
75. Saveyn, H., et al., *Accurate particle size distribution determination by nanoparticle tracking analysis based on 2-D Brownian dynamics simulation.* Journal of Colloid and Interface Science, 2010. **352**(2): p. 593-600.
76. Axson, J.L., et al., *An In Situ Method for Sizing Insoluble Residues in Precipitation and Other Aqueous Samples.* Aerosol Science and Technology, 2014. **49**(1): p. 24-34.
77. Axson, J.L., et al., *Rapid Kinetics of Size and pH-Dependent Dissolution and Aggregation of Silver Nanoparticles in Simulated Gastric Fluid.* The Journal of Physical Chemistry C, 2015. **119**(35): p. 20632-20641.

78. Novak, J.P., et al., *Purification of molecularly bridged metal nanoparticle arrays by centrifugation and size exclusion chromatography.* Analytical Chemistry, 2001. **73**(23): p. 5758-5761.
79. Baalousha, M., B. Stolpe, and J.R. Lead, *Flow field-flow fractionation for the analysis and characterization of natural colloids and manufactured nanoparticles in environmental systems: A critical review.* Journal of Chromatography A, 2011. **1218**(27): p. 4078-4103.
80. Walter, J., et al., *Multidimensional Analysis of Nanoparticles with Highly Disperse Properties Using Multiwavelength Analytical Ultracentrifugation.* ACS Nano, 2014. **8**(9): p. 8871-8886.
81. Walter, J., et al., *New possibilities of accurate particle characterisation by applying direct boundary models to analytical centrifugation.* Nanoscale, 2015. **7**(15): p. 6574-6587.
82. Dudkiewicz, A., et al., *A uniform measurement expression for cross method comparison of nanoparticle aggregate size distributions.* Analyst, 2015. **140**(15): p. 5257-5267.
83. Fernandez de la Mora, J., et al., *Differential mobility analysis of molecular ions and nanometer particles.* Trac-Trends in Analytical Chemistry, 1998. **17**(6): p. 328-339.
84. Wiedensohler, A., et al., *Mobility particle size spectrometers: harmonization of technical standards and data structure to facilitate high quality long-term observations of atmospheric particle number size distributions.* Atmospheric Measurement Techniques, 2012. **5**(3): p. 657-685.
85. Park, J.Y., P.H. McMurry, and K. Park, *Production of Residue-Free Nanoparticles by Atomization of Aqueous Solutions.* Aerosol Science and Technology, 2012. **46**(3): p. 354-360.
86. Kaufman, S.L., *Analysis of biomolecules using electrospray and nanoparticle methods: The gas-phase electrophoretic mobility molecular analyzer (GEMMA).* Journal of Aerosol Science, 1998. **29**(5-6): p. 537-552.
87. de Juan, L. and J. Fernandez de la Mora, *On-line sizing of colloidal nanoparticles via electrospray and aerosol techniques.* Nanotechnology, 1996. **622**: p. 20-41.

88. Bacher, G., et al., *Charge-reduced nano electrospray ionization combined with differential mobility analysis of peptides, proteins, glycoproteins, noncovalent protein complexes and viruses.* Journal of Mass Spectrometry, 2001. **36**(9): p. 1038-1052.

89. Kaufman, S.L., et al., *Macromolecule analysis based on electrophoretic mobility in air: Globular proteins.* Analytical Chemistry, 1996. **68**(11): p. 1895-1904.

90. Han, B., et al., *Measurement of cluster ions and residue nanoparticles from water samples with an electrospray/differential mobility analyzer.* Analytical Sciences, 2003. **19**(6): p. 843-851.

91. Lenggoro, I.W., et al., *Colloidal nanoparticle analysis by nanoelectrospray size spectrometry with a heated flow.* Analytica Chimica Acta, 2007. **585**: p. 193-201.

92. Lenggoro, I.W., et al., *Sizing of colloidal nanoparticles by electrospray and differential mobility analyzer methods.* Langmuir, 2002. **18**(12): p. 4584-4591.

93. Guha, S., et al., *Quantifying Ligand Adsorption to Nanoparticles Using Tandem Differential Mobility Mass Analysis.* Analytical Chemistry, 2012. **84**(15): p. 6308-6311.

94. Tsai, D.H., et al., *Temperature-Programmed Electrospray-Differential Mobility Analysis for Characterization of Ligated Nanoparticles in Complex Media.* Langmuir, 2013. **29**(36): p. 11267-11274.

95. Tsai, D.H., et al., *Quantifying dithiothreitol displacement of functional ligands from gold nanoparticles.* Analytical and Bioanalytical Chemistry, 2012. **404**(10): p. 3015-3023.

96. Pease, L.F., et al., *Packing and Size Determination of Colloidal Nanoclusters.* Langmuir, 2010. **26**(13): p. 11384-11390.

97. Tsai, D.H., et al., *Adsorption and Conformation of Serum Albumin Protein on Gold Nanoparticles Investigated Using Dimensional Measurements and in Situ Spectroscopic Methods.* Langmuir, 2011. **27**(6): p. 2464-2477.

98. Tsai, D.H., et al., *Competitive Adsorption of Thiolated Polyethylene Glycol and Mercaptopropionic Acid on Gold Nanoparticles Measured by Physical Characterization Methods.* Langmuir, 2010. **26**(12): p. 10325-10333.

99. Pease, L.F., et al., *Quantifying the surface coverage of conjugate molecules on functionalized nanoparticles.* Journal of Physical Chemistry C, 2007. **111**(46): p. 17155-17157.
100. Tsai, D.H., et al., *Gas-phase ion-mobility characterization of SAM-functionalized Au nanoparticles.* Langmuir, 2008. **24**(16): p. 8483-8490.
101. Scalf, M., et al., *Controlling charge states of large ions.* Science, 1999. **283**(5399): p. 194-197.
102. Scalf, M., M.S. Westphall, and L.M. Smith, *Charge reduction electrospray mass spectrometry.* Analytical Chemistry, 2000. **72**(1): p. 52-60.
103. Elzey, S., et al., *Real-time size discrimination and elemental analysis of gold nanoparticles using ES-DMA coupled to ICP-MS.* Analytical and Bioanalytical Chemistry, 2013. **405**(7): p. 2279-2288.
104. Ku, B.K., et al., *Mass distribution measurement of water-insoluble polymers by charge-reduced electrospray mobility analysis.* Analytical Chemistry, 2004. **76**(3): p. 814-822.
105. Saucy, D.A., et al., *Mass analysis of water-soluble polymers by mobility measurement of charge-reduced ions generated by electrosprays.* Analytical Chemistry, 2004. **76**(4): p. 1045-1053.
106. Müller, R., et al., *Determination of Molecular Weight, Particle Size, and Density of High Number Generation PAMAM Dendrimers Using MALDI−TOF−MS and nES−GEMMA.* Macromolecules, 2007. **40**(15): p. 5599-5605.
107. Fernandez de la Mora, J., *High-Resolution Mobility Analysis of Charge-Reduced Electrosprayed Protein Ions.* Analytical Chemistry, 2015. **87**(7): p. 3729-3735.
108. Pease, L.F., et al., *Physical Characterization of Icosahedral Virus Ultra Structure, Stability, and Integrity Using Electrospray Differential Mobility Analysis.* Analytical Chemistry, 2011. **83**(5): p. 1753-1759.
109. Allmaier, G., C. Laschober, and W.W. Szymariski, *Nano ES GEMMA and PDMA, new tools for the analysis of nanobioparticles - Protein complexes, lipoparticles, and viruses.* Journal of the American Society for Mass Spectrometry, 2008. **19**(8): p. 1062-1068.

110. Allmaier, G., et al., *Parallel differential mobility analysis for electrostatic characterization and manipulation of nanoparticles and viruses.* Trac-Trends in Analytical Chemistry, 2011. **30**(1): p. 123-132.
111. Hogan, C.J., et al., *Charge reduced electrospray size spectrometry of mega- and gigadalton complexes: Whole viruses and virus fragments.* Analytical Chemistry, 2006. **78**(3): p. 844-852.
112. Thomas, J.J., et al., *Electrospray ion mobility spectrometry of intact viruses.* Spectroscopy-an International Journal, 2004. **18**(1): p. 31-36.
113. Wick, C.H. and P.E. McCubbin, *Characterization of purified MS2 bacteriophage by the physical counting methodology used in the integrated virus detection system (IVDS).* Toxicology Methods, 1999. **9**(4): p. 245-252.
114. Havlik, M., et al., *Comprehensive Size-Determination of Whole Virus Vaccine Particles Using Gas-Phase Electrophoretic Mobility Macromolecular Analyzer, Atomic Force Microscopy, and Transmission Electron Microscopy.* Analytical Chemistry, 2015. **87**(17): p. 8657-8664.
115. Laschober, C., et al., *Gas-Phase Electrophoretic Molecular Mobility Analysis of Size and Stoichiometry of Complexes of a Common Cold Virus with Antibody and Soluble Receptor Molecules.* Analytical Chemistry, 2008. **80**(6): p. 2261-2264.
116. Chen, D.R. and D.Y.H. Pui, *Experimental investigation of scaling laws for electrospraying: Dielectric constant effect.* Aerosol Science and Technology, 1997. **27**(3): p. 367-380.
117. Chen, D.R., D.Y.H. Pui, and S.L. Kaufman, *Electrospraying of Conducting Liquids for Monodisperse Aerosol Generation in the 4 nm to 1.8 mm Diameter Range.* Journal of Aerosol Science, 1995. **26**(6): p. 963-977.
118. Gopalakrishnan, R., P.H. McMurry, and C.J. Hogan, *The Electrical Mobilities and Scalar Friction Factors of Modest to High Aspect Ratio Particles in the Transition Regime.* Journal of Aerosol Science, 2015. **82**: p. 24-39.
119. Li, M., et al., *Evaluating the Mobility of Nanorods in Electric Fields.* Aerosol Science and Technology, 2013. **47**(10): p. 1101-1107.

120. Kallinger, P., G. Steiner, and W. Szymanski, *Characterization of four different bipolar charging devices for nanoparticle charge conditioning.* Journal of Nanoparticle Research, 2012. **14**(6): p. 1-8.
121. Shimada, M., et al., *Bipolar charging of aerosol nanoparticles by a soft X-ray photoionizer.* Journal of Chemical Engineering of Japan, 2002. **35**(8): p. 786-793.
122. Maisser, A., et al., *The Mass-Mobility Distributions of Ions Produced by a Po-210 Source in Air.* Journal of Aerosol Science, 2015. **90**: p. 36-50.
123. Gopalakrishnan, R., et al., *Brownian Dynamics Determination of the Bipolar Steady State Charge Distribution on Spheres and Non-spheres in the Transition Regime.* Journal of Aerosol Science, 2013. **63**: p. 126-145.
124. Wiedensohler, A., *An Approximation of the Bipolar Charge-Distribution for Particles in the Sub-Micron Size Range.* Journal of Aerosol Science, 1988. **19**(3): p. 387-389.
125. Wang, S.C. and R.C. Flagan, *Scanning Electrical Mobility Spectrometer.* Aerosol Science and Technology, 1990. **13**(2): p. 230-240.
126. Jeon, S., T. Thajudeen, and C.J. Hogan, *Evaluation of nanoparticle aggregate morphology during wet milling.* Powder Technology, 2015. **272**: p. 75-84.
127. Larriba, C., et al., *The Mobility-Volume Relationship below 3.0 nm examined by Tandem Mobility-Mass Measurement.* Aerosol Science and Technology, 2011. **45**: p. 453-467.
128. Zhang, C., et al., *Determination of the Scalar Friction Factor for Non-spherical Particles and Aggregates Across the Entire Knudsen Number Range by Direct Simulation Monte Carlo (DSMC).* Aerosol Science and Technology, 2012. **46**: p. 1065-1078.
129. Gormley, P.G. and M. Kennedy, *Diffusion from a stream flowing through a cylindrical tube.* Proceedings of the Irish Royal Academy, 1949. **52A**: p. 163-169.
130. Gopalakrishnan, R., P.H. McMurry, and C.J. Hogan, *Bipolar Charging of Nanoparticles: A Review and Development of Approaches for Non-spherical Particles.* Aerosol Science and Technology, 2015. **In Press**.

131. Bush, M.F., et al., *Collision Cross Sections of Proteins and their Complexes: a Calibration Framework and Database for Gas-Phase Structural Biology.* Analytical Chemistry, 2010. **82**: p. 9557-9565.

132. Hogan, C.J. and J. Fernandez de la Mora, *Ion Mobility Measurements of Non-Denatured 12 - 150 kDa Proteins and Protein Multimers by Tandem Differential Mobility Analysis - Mass Spectrometry (DMA-MS).* Journal of the American Society for Mass Spectrometry, 2011. **22**: p. 158-172.

133. Maiber, A., et al., *Determination of gas phase protein ion densities via ion mobility analysis with charge reduction.* Physical Chemistry Chemical Physics, 2011. **13**(48): p. 21630-21641.

134. Hogan, C.J. and P. Biswas, *Narrow size distribution nanoparticle production by electrospray processing of ferritin.* Journal of Aerosol Science, 2008. **39**(5): p. 432-440.

135. Hogan, C.J. and P. Biswas, *Monte Carlo simulation of macromolecular ionization by nanoelectrospray.* Journal of the American Society for Mass Spectrometry, 2008. **19**(8): p. 1098-1107.

136. Lewis, K.C., et al., *Electrospray-Condensation Particle Counter - a Molecule-Counting Lc-Detector for Macromolecules.* Analytical Chemistry, 1994. **66**(14): p. 2285-2292.

137. Li, M., et al., *Quantification and Compensation of Nonspecific Analyte Aggregation in Electrospray Sampling.* Aerosol Science and Technology, 2011. **45**(7): p. 849-860.

138. Larriba-Andaluz, C., et al., *Gas Molecule Scattering & Ion Mobility Measurements for Organic Macro-ions in He versus N_2 Environments.* Phys Chem Chem Phys, 2015. **17**: p. 15019-15029.

139. Kim, J.H., et al., *Slip correction measurements of certified PSL nanoparticles using a nanometer differential mobility analyzer (nano-DMA) for Knudsen number from 0.5 to 83.* Journal of Research of the National Institute of Standards and Technology, 2005. **110**(1): p. 31-54.

140. Jung, H., et al., *Effect of the surface energy of particle materials on the accommodation of gas molecules to the particle surfaces.* Journal of Aerosol Science, 2013. **65**: p. 42-48.
141. Giechaskiel, B., et al., *Calibration of Condensation Particle Counters for Legislated Vehicle Number Emission Measurements.* Aerosol Science and Technology, 2009. **43**(12): p. 1164-1173.
142. Ouyang, H., et al., *IMS–MS and IMS–IMS Investigation of the Structure and Stability of Dimethylamine-Sulfuric Acid Nanoclusters.* The Journal of Physical Chemistry A, 2015. **119**(10): p. 2026-2036.
143. Rader, D.J. and P.H. McMurry, *Application of the Tandem Differential Mobility Analyzer to Studies of Droplet Growth or Evaporation.* Journal of Aerosol Science, 1986. **17**(5): p. 771-787.
144. Tajima, N., et al., *Design Considerations and Performance Evaluation of a Compact Aerosol Particle Mass Analyzer.* Aerosol Science and Technology, 2013. **47**(10): p. 1152-1162.
145. Ashby, J., et al., *High-Throughput Profiling of Nanoparticle-Protein Interactions by Fluorescamine Labeling.* Analytical Chemistry, 2015. **87**(4): p. 2213-2219.
146. Ashby, J., et al., *Dissociation-Based Screening of Nanoparticle-Protein Interaction via Flow Field-Flow Fractionation.* Analytical Chemistry, 2013. **85**(15): p. 7494-7501.
147. Maiolo, D., et al., *Surfactant Titration of Nanoparticle-Protein Corona.* Analytical Chemistry, 2014. **86**(24): p. 12055-12063.
148. Mudalige, T.K., H.O. Qu, and S.W. Linder, *Asymmetric Flow-Field Flow Fractionation Hyphenated ICP-MS as an Alternative to Cloud Point Extraction for Quantification of Silver Nanoparticles and Silver Speciation: Application for Nanoparticles with a Protein Corona.* Analytical Chemistry, 2015. **87**(14): p. 7395-7401.
149. Cedervall, T., et al., *Understanding the nanoparticle-protein corona using methods to quantify exchange rates and affinities of proteins for nanoparticles.* Proceedings of the National Academy of Sciences of the United States of America, 2007. **104**(7): p. 2050-2055.

150. Liu, R., et al., *Prediction of nanoparticles-cell association based on corona proteins and physicochemical properties.* Nanoscale, 2015. **7**(21): p. 9664-9675.
151. Sykes, E.A., et al., *Investigating the Impact of Nanoparticle Size on Active and Passive Tumor Targeting Efficiency.* Acs Nano, 2014. **8**(6): p. 5696-5706.
152. Walkey, C.D. and W.C.W. Chan, *Understanding and controlling the interaction of nanomaterials with proteins in a physiological environment.* Chemical Society Reviews, 2012. **41**(7): p. 2780-2799.
153. Walkey, C.D., et al., *Protein Corona Fingerprinting Predicts the Cellular Interaction of Gold and Silver Nanoparticles.* Acs Nano, 2014. **8**(3): p. 2439-2455.
154. Dobrovolskaia, M.A., et al., *Interaction of colloidal gold nanoparticles with human blood: effects on particle size and analysis of plasma protein binding profiles.* Nanomedicine: Nanotechnology, Biology and Medicine, 2009. **5**(2): p. 106-117.
155. Dominguez-Medina, S., et al., *Adsorption of a Protein Monolayer via Hydrophobic Interactions Prevents Nanoparticle Aggregation under Harsh Environmental Conditions.* ACS Sustainable Chemistry & Engineering, 2013. **1**(7): p. 833-842.
156. Calzolai, L., et al., *Protein−Nanoparticle Interaction: Identification of the Ubiquitin−Gold Nanoparticle Interaction Site.* Nano Letters, 2010. **10**(8): p. 3101-3105.
157. Montes-Burgos, I., et al., *Characterisation of nanoparticle size and state prior to nanotoxicological studies.* Journal of Nanoparticle Research, 2009. **12**(1): p. 47-53.
158. James, A.E. and J.D. Driskell, *Monitoring gold nanoparticle conjugation and analysis of biomolecular binding with nanoparticle tracking analysis (NTA) and dynamic light scattering (DLS).* Analyst, 2013. **138**(4): p. 1212-1218.
159. Chen, A.L., et al., *Quantifying spectral changes experienced by plasmonic nanoparticles in a cellular environment to inform biomedical nanoparticle design.* Nanoscale Research Letters, 2014. **9**.
160. Zijlstra, P., P.M.R. Paulo, and M. Orrit, *Optical detection of single non-absorbing molecules using the surface plasmon resonance of a gold nanorod.* Nature Nanotechnology, 2012. **7**(6): p. 379-382.
161. Bohrer, B.C., et al., *Biomolecule Analysis by Ion Mobility Spectrometry.* Annual Review of Analytical Chemistry, 2008. **1**: p. 293-327.

162. Jeon, S., et al., *Nanomaterial size distribution analysis via liquid nebulization coupled with ion mobility spectrometry (LN-IMS).* Analyst, 2016. **141**(4): p. 1363-1375.

163. Stolzenburg, M.R. and P.H. McMurry, *Equations governing single and tandem DMA configurations and a new lognormal approximation to the transfer function.* Aerosol Science and Technology, 2008. **42**(6): p. 421-432.

164. Gopalakrishnan, R., P.H. McMurry, and C.J. Hogan, *Bipolar Charging of Nanoparticles: A Review and Development of Approaches for Non-spherical Particles.* Aerosol Science and Technology, 2015. **49**: p. 1181-1194.

165. Brewer, S.H., et al., *Probing BSA Binding to Citrate-Coated Gold Nanoparticles and Surfaces.* Langmuir, 2005. **21**(20): p. 9303-9307.

166. Kaufman, E.D., et al., *Probing Protein Adsorption onto Mercaptoundecanoic Acid Stabilized Gold Nanoparticles and Surfaces by Quartz Crystal Microbalance and ζ-Potential Measurements.* Langmuir, 2007. **23**(11): p. 6053-6062.

167. Oberreit, D., et al., *Analysis of heterogeneous water vapor uptake by metal iodide cluster ions via differential mobility analysis-mass spectrometry*. The Journal of Chemical Physics, 2015. **143**(10): p. 104204.

168. Oberreit, D.R., P.H. McMurry, and C.J. Hogan, *Analysis of heterogeneous uptake by nanoparticles via differential mobility analysis-drift tube ion mobility spectrometry*. Physical Chemistry Chemical Physics, 2014. **16**(15): p. 6968-6979.

169. Rawat, V.K., G. Vidal-de-Miguel, and C.J. Hogan, *Modeling vapor uptake induced mobility shifts in peptide ions observed with transversal modulation ion mobility spectrometry-mass spectrometry.* Analyst, 2015. **140**(20): p. 6945-6954.

170. Lacerda, S.H.D.P., et al., *Interaction of Gold Nanoparticles with Common Human Blood Proteins.* Acs Nano, 2010. **4**(1): p. 365-379.

171. Teichroeb, J.H., J.A. Forrest, and L.W. Jones, *Size-dependent denaturing kinetics of bovine serum albumin adsorbed onto gold nanospheres.* The European Physical Journal E, 2008. **26**(4): p. 411-415.

172. Northrup, S.H., S.A. Allison, and J.A. McCammon, *Brownian Dynamics Simulation of Diffusion-Influenced Bimolecular Reactions*. Journal of Chemical Physics, 1984. **80**(4): p. 1517-1526.

173. Smith, M. and T. Matsoukas, *Constant-number Monte Carlo simulation of population balances.* Chemical Engineering Science, 1998. **53**(9): p. 1777-1786.
174. Ruotolo, B.T., et al., *Ion mobility-mass spectrometry analysis of large protein complexes.* Nature Protocols, 2008. **3**(7): p. 1139-1152.
175. Laurent, S., et al., *Magnetic fluid hyperthermia: Focus on superparamagnetic iron oxide nanoparticles.* Advances in Colloid and Interface Science, 2011. **166**(1–2): p. 8-23.
176. Hergt, R., et al., *Physical limits of hyperthermia using magnetite fine particles.* IEEE Transactions on Magnetics, 1998. **34**(5): p. 3745-3754.
177. Rosensweig, R.E., *Heating magnetic fluid with alternating magnetic field.* Journal of Magnetism and Magnetic Materials, 2002. **252**: p. 370-374.
178. Thorek, D.L.J., et al., *Superparamagnetic Iron Oxide Nanoparticle Probes for Molecular Imaging.* Annals of Biomedical Engineering, 2006. **34**(1): p. 23-38.
179. Chertok, B., et al., *Iron oxide nanoparticles as a drug delivery vehicle for MRI monitored magnetic targeting of brain tumors.* Biomaterials, 2008. **29**(4): p. 487-496.
180. Lee, H., et al., *Antibiofouling Polymer-Coated Superparamagnetic Iron Oxide Nanoparticles as Potential Magnetic Resonance Contrast Agents for in Vivo Cancer Imaging.* Journal of the American Chemical Society, 2006. **128**(22): p. 7383-7389.
181. Saini, S., et al., *Ferrite particles: a superparamagnetic MR contrast agent for the reticuloendothelial system.* Radiology, 1987. **162**(1): p. 211-216.
182. Stark, D.D., et al., *Superparamagnetic iron oxide: clinical application as a contrast agent for MR imaging of the liver.* Radiology, 1988. **168**(2): p. 297-301.
183. Hachani, R., et al., *Polyol synthesis, functionalisation, and biocompatibility studies of superparamagnetic iron oxide nanoparticles as potential MRI contrast agents.* Nanoscale, 2016. **8**(6): p. 3278-3287.
184. Shi, Z., et al., *(Carboxymethyl)chitosan-Modified Superparamagnetic Iron Oxide Nanoparticles for Magnetic Resonance Imaging of Stem Cells.* ACS Applied Materials & Interfaces, 2009. **1**(2): p. 328-335.

185. Lu, B.-Q., et al., *Synthesis and Characterization of Magnetic Iron Oxide/Calcium Silicate Mesoporous Nanocomposites as a Promising Vehicle for Drug Delivery.* ACS Applied Materials & Interfaces, 2012. **4**(12): p. 6969-6974.

186. Zhou, L., B. He, and F. Zhang, *Facile One-Pot Synthesis of Iron Oxide Nanoparticles Cross-linked Magnetic Poly(vinyl alcohol) Gel Beads for Drug Delivery.* ACS Applied Materials & Interfaces, 2012. **4**(1): p. 192-199.

187. Balcioglu, M., et al., *DNA-Length-Dependent Quenching of Fluorescently Labeled Iron Oxide Nanoparticles with Gold, Graphene Oxide and MoS2 Nanostructures.* ACS Applied Materials & Interfaces, 2014. **6**(15): p. 12100-12110.

188. Clay, N., et al., *Flow-Mediated Stem Cell Labeling with Superparamagnetic Iron Oxide Nanoparticle Clusters.* ACS Applied Materials & Interfaces, 2013. **5**(20): p. 10266-10273.

189. He, J., et al., *Magnetic separation techniques in sample preparation for biological analysis: A review.* Journal of Pharmaceutical and Biomedical Analysis, 2014. **101**: p. 84-101.

190. Espinosa, A., et al., *Duality of Iron Oxide Nanoparticles in Cancer Therapy: Amplification of Heating Efficiency by Magnetic Hyperthermia and Photothermal Bimodal Treatment.* ACS Nano, 2016. **10**(2): p. 2436-2446.

191. Goya, G.F., V. Grazu, and M.R. Ibarra, *Magnetic Nanoparticles for Cancer Therapy.* Current Nanoscience, 2008. **4**(1): p. 1-16.

192. Jordan, A., et al., *Magnetic fluid hyperthermia (MFH): Cancer treatment with AC magnetic field induced excitation of biocompatible superparamagnetic nanoparticles.* Journal of Magnetism and Magnetic Materials, 1999. **201**(1–3): p. 413-419.

193. Di Corato, R., et al., *Magnetic hyperthermia efficiency in the cellular environment for different nanoparticle designs.* Biomaterials, 2014. **35**(24): p. 6400-6411.

194. Etheridge, M.L., et al., *RF heating of magnetic nanoparticles improves the thawing of cryopreserved biomaterials.* Technology, 2014. **02**(03): p. 229-242.

195. Grüttner, C., et al., *Synthesis and antibody conjugation of magnetic nanoparticles with improved specific power absorption rates for alternating magnetic field*

cancer therapy. Journal of Magnetism and Magnetic Materials, 2007. **311**(1): p. 181-186.

196. Gonzales-Weimuller, M., M. Zeisberger, and K.M. Krishnan, *Size-dependant heating rates of iron oxide nanoparticles for magnetic fluid hyperthermia.* Journal of Magnetism and Magnetic Materials, 2009. **321**(13): p. 1947-1950.
197. Etheridge, M.L. and J.C. Bischof, *Optimizing Magnetic Nanoparticle Based Thermal Therapies Within the Physical Limits of Heating.* Annals of Biomedical Engineering, 2012. **41**(1): p. 78-88.
198. Ashby, J., S. Pan, and W. Zhong, *Size and Surface Functionalization of Iron Oxide Nanoparticles Influence the Composition and Dynamic Nature of Their Protein Corona.* ACS Applied Materials & Interfaces, 2014. **6**(17): p. 15412-15419.
199. Casals, E., et al., *Time Evolution of the Nanoparticle Protein Corona.* ACS Nano, 2010. **4**(7): p. 3623-3632.
200. Townson, J.L., et al., *Re-examining the Size/Charge Paradigm: Differing in Vivo Characteristics of Size- and Charge-Matched Mesoporous Silica Nanoparticles.* Journal of the American Chemical Society, 2013. **135**(43): p. 16030-16033.
201. Shah, N.B., et al., *Blood-Nanoparticle Interactions and in Vivo Biodistribution: Impact of Surface PEG and Ligand Properties.* Molecular Pharmaceutics, 2012. **9**(8): p. 2146-2155.
202. Albanese, A. and W.C.W. Chan, *Effect of Gold Nanoparticle Aggregation on Cell Uptake and Toxicity.* ACS Nano, 2011. **5**(7): p. 5478-5489.
203. Zhang, D., et al., *Gold Nanoparticles Can Induce the Formation of Protein-based Aggregates at Physiological pH.* Nano Letters, 2009. **9**(2): p. 666-671.
204. Safi, M., et al., *The effects of aggregation and protein corona on the cellular internalization of iron oxide nanoparticles.* Biomaterials, 2011. **32**(35): p. 9353-9363.
205. Mahmoudi, M., et al., *Protein−Nanoparticle Interactions: Opportunities and Challenges.* Chemical Reviews, 2011. **111**(9): p. 5610-5637.
206. Etheridge, M.L., et al., *Accounting for biological aggregation in heating and imaging of magnetic nanoparticles.* TECHNOLOGY, 2014. **02**(03): p. 214-228.

207. Ovejero, J.G., et al., *Effects of inter- and intra-aggregate magnetic dipolar interactions on the magnetic heating efficiency of iron oxide nanoparticles.* Physical Chemistry Chemical Physics, 2016.

208. Fortin, J.-P., F. Gazeau, and C. Wilhelm, *Intracellular heating of living cells through Néel relaxation of magnetic nanoparticles.* European Biophysics Journal, 2007. **37**(2): p. 223-228.

209. Hurley, K.R., et al., *Predictable Heating and Positive MRI Contrast from a Mesoporous Silica-Coated Iron Oxide Nanoparticle.* Molecular Pharmaceutics, 2016.

210. Jeon, S., et al., *Quantifying Intra- and Extracellular Aggregation of Iron Oxide Nanoparticles and its Influence on Specific Absorption Rate.* Submitted to: Nanoscale, 2016.

211. Hurley, K.R., et al., *Characterization of Magnetic Nanoparticles in Biological Matrices.* Analytical Chemistry, 2015. **87**(23): p. 11611-11619.

212. Baalousha, M., *Aggregation and disaggregation of iron oxide nanoparticles: Influence of particle concentration, pH and natural organic matter.* Science of The Total Environment, 2009. **407**(6): p. 2093-2101.

213. Odriozola, G., et al., *A Light Scattering Study of the Transition Region between Diffusion- and Reaction-Limited Cluster Aggregation.* Journal of Colloid and Interface Science, 2001. **240**(1): p. 90-96.

214. Alwi, R., et al., *Silica-coated super paramagnetic iron oxide nanoparticles (SPION) as biocompatible contrast agent in biomedical photoacoustics.* Biomedical Optics Express, 2012. **3**(10): p. 2500-2509.

215. Santra, S., et al., *Synthesis and Characterization of Silica-Coated Iron Oxide Nanoparticles in Microemulsion: The Effect of Nonionic Surfactants.* Langmuir, 2001. **17**(10): p. 2900-2906.

216. Tsoncheva, T., et al., *Critical evaluation of the state of iron oxide nanoparticles on different mesoporous silicas prepared by an impregnation method.* Microporous and Mesoporous Materials, 2008. **112**(1–3): p. 327-337.

217. Tong, S., et al., *Coating Optimization of Superparamagnetic Iron Oxide Nanoparticles for High T2 Relaxivity.* Nano Letters, 2010. **10**(11): p. 4607-4613.

218. Xie, J., et al., *Controlled PEGylation of Monodisperse Fe3O4 Nanoparticles for Reduced Non-Specific Uptake by Macrophage Cells.* Advanced Materials, 2007. **19**(20): p. 3163-3166.
219. Egger, S.M., et al., *Ultraporous Mesostructured Silica Nanoparticles.* Chemistry of Materials, 2015. **27**(9): p. 3193-3196.
220. Hurley, K.R., et al., *Effects of Mesoporous Silica Coating and Postsynthetic Treatment on the Transverse Relaxivity of Iron Oxide Nanoparticles.* Chemistry of Materials, 2013. **25**(9): p. 1968-1978.
221. Lin, Y.-S. and C.L. Haynes, *Synthesis and Characterization of Biocompatible and Size-Tunable Multifunctional Porous Silica Nanoparticles.* Chemistry of Materials, 2009. **21**(17): p. 3979-3986.
222. Ruotolo, B.T., et al., *Evidence for macromolecular protein rings in the absence of bulk water.* Science, 2005. **310**: p. 1658-1661.
223. Kulmala, M., et al., *Toward Direct Measurement of Atmospheric Nucleation.* Science, 2007. **318**: p. 89-92.
224. Kirkby, J., et al., *Role of sulphuric acid, ammonia and galactic cosmic rays in atmospheric aerosol nucleation.* Nature, 2011. **476**(7361): p. 429-U77.
225. Jeon, S., et al., *Liquid Nebulization-Ion Mobility Spectrometry Based Quantification of Nanoparticle-Protein Conjugate Formation.* Submitted to: Analytical Chemistry, 2016.
226. Jeon, S., T. Thajudeen, and C.J. Hogan Jr, *Evaluation of nanoparticle aggregate morphology during wet milling.* Powder Technology, 2015. **272**: p. 75-84.
227. Kim, A.Y. and J.C. Berg, *Fractal Aggregation: Scaling of Fractal Dimension with Stability Ratio.* Langmuir, 2000. **16**(5): p. 2101-2104.
228. Schwarzer, H.C. and W. Peukert, *Prediction of aggregation kinetics based on surface properties of nanoparticles.* Chemical Engineering Science, 2005. **60**(1): p. 11-25.
229. Vemury, S. and S.E. Pratsinis, *Self-Preserving Size Distributions of Agglomerates.* Journal of Aerosol Science, 1995. **26**(2): p. 175-185.
230. Coral, D.F., et al., *Effect of Nanoclustering and Dipolar Interactions in Heat Generation for Magnetic Hyperthermia.* Langmuir, 2016. **32**(5): p. 1201-1213.

231. Gupta, A.K. and M. Gupta, *Synthesis and surface engineering of iron oxide nanoparticles for biomedical applications.* Biomaterials, 2005. **26**(18): p. 3995-4021.

232. Liu, H., et al., *Application of iron oxide nanoparticles in glioma imaging and therapy: from bench to bedside.* Nanoscale, 2016. **8**(15): p. 7808-7826.

233. Quinto, C.A., et al., *Multifunctional superparamagnetic iron oxide nanoparticles for combined chemotherapy and hyperthermia cancer treatment.* Nanoscale, 2015. **7**(29): p. 12728-12736.

234. Bordelon, D.E., et al., *Magnetic nanoparticle heating efficiency reveals magneto-structural differences when characterized with wide ranging and high amplitude alternating magnetic fields.* Journal of Applied Physics, 2011. **109**(12): p. 124904.

235. DeNardo, S.J., et al., *Development of Tumor Targeting Bioprobes (111In-Chimeric L6 Monoclonal Antibody Nanoparticles) for Alternating Magnetic Field Cancer Therapy.* Clinical Cancer Research, 2005. **11**(19): p. 7087s-7092s.

236. Polo-Corrales, L. and C. Rinaldi, *Monitoring iron oxide nanoparticle surface temperature in an alternating magnetic field using thermoresponsive fluorescent polymers.* Journal of Applied Physics, 2012. **111**(7): p. 07B334.

237. Zhang, L.-Y., H.-C. Gu, and X.-M. Wang, *Magnetite ferrofluid with high specific absorption rate for application in hyperthermia.* Journal of Magnetism and Magnetic Materials, 2007. **311**(1): p. 228-233.

238. Asín, L., et al., *Controlled Cell Death by Magnetic Hyperthermia: Effects of Exposure Time, Field Amplitude, and Nanoparticle Concentration.* Pharmaceutical Research, 2012. **29**(5): p. 1319-1327.

239. Johannsen, M., et al., *Clinical hyperthermia of prostate cancer using magnetic nanoparticles: Presentation of a new interstitial technique.* International Journal of Hyperthermia, 2005. **21**(7): p. 637-647.

240. Petri-Fink, A., et al., *Development of functionalized superparamagnetic iron oxide nanoparticles for interaction with human cancer cells.* Biomaterials, 2005. **26**(15): p. 2685-2694.

241. Materia, M.E., et al., *Mesoscale Assemblies of Iron Oxide Nanocubes as Heat Mediators and Image Contrast Agents.* Langmuir, 2015. **31**(2): p. 808-816.

242. Chen, K.L., S.E. Mylon, and M. Elimelech, *Enhanced Aggregation of Alginate-Coated Iron Oxide (Hematite) Nanoparticles in the Presence of Calcium, Strontium, and Barium Cations.* Langmuir, 2007. **23**(11): p. 5920-5928.

243. Illés, E. and E. Tombácz, *The effect of humic acid adsorption on pH-dependent surface charging and aggregation of magnetite nanoparticles.* Journal of Colloid and Interface Science, 2006. **295**(1): p. 115-123.

244. Liu, Z., et al., *A magnetic-dependent protein corona of tailor-made superparamagnetic iron oxides alters their biological behaviors.* Nanoscale, 2016. **8**(14): p. 7544-7555.

245. Thajudeen, T., S. Jeon, and C.J. Hogan Jr, *The mobilities of flame synthesized aggregates/agglomerates in the transition regime.* Journal of Aerosol Science, 2015. **80**: p. 45-57.

246. Koeylue, U., Y. Xing, and D.E. Rosner, *Fractal Morphology Analysis of Combustion-Generated Aggregates Using Angular Light Scattering and Electron Microscope Images.* Langmuir, 1995. **11**(12): p. 4848-4854.

247. Hoffmann, N.E. and J.C. Bischof, *The cryobiology of cryosurgical injury*. Urology, 2002. **60**(2, Supplement 1): p. 40-49.

248. Heinson, W.R., C.M. Sorensen, and A. Chakrabarti, *A three parameter description of the structure of diffusion limited cluster fractal aggregates.* Journal of Colloid and Interface Science, 2012. **375**: p. 65-69.

249. Meakin, P. and R. Jullien, *The effects of restructuring on the geometry of clusters formed by diffusion-limited, ballistic, and reaction-limited cluster–cluster aggregation.* The Journal of Chemical Physics, 1988. **89**(1): p. 246-250.

250. Lin, M.Y., et al., *Universal diffusion-limited colloid aggregation.* Journal of Physics: Condensed Matter, 1990. **2**(13): p. 3093.

251. Meakin, P., *Diffusion-limited aggregation in three dimensions: Results from a new cluster-cluster aggregation model.* Journal of Colloid and Interface Science, 1984. **102**(2): p. 491-504.

252. Weitz, D.A., et al., *Limits of the Fractal Dimension for Irreversible Kinetic Aggregation of Gold Colloids.* Physical Review Letters, 1985. **54**(13): p. 1416-1419.

253. Schaefer, D.W., et al., *Fractal Geometry of Colloidal Aggregates.* Physical Review Letters, 1984. **52**(26): p. 2371-2374.
254. Kimura, H., *Light-scattering properties of fractal aggregates: numerical calculations by a superposition technique and the discrete-dipole approximation.* Journal of Quantitative Spectroscopy and Radiative Transfer, 2001. **70**(4–6): p. 581-594.
255. Douglas, J.F., H.-X. Zhou, and J.B. Hubbard, *Hydrodynamic friction and the capacitance of arbitrarily shaped objects.* Physical Review E, 1994. **49**(6): p. 5319-5331.
256. Given, J.A., J.B. Hubbard, and J.F. Douglas, *A first-passage algorithm for the hydrodynamic friction and diffusion-limited reaction rate of macromolecules.* The Journal of Chemical Physics, 1997. **106**(9): p. 3761-3771.
257. Zhou, H.X., et al., *A Brownian dynamics algorithm for calculating the hydrodynamic friction and the electrostatic capacitance of an arbitrarily shaped object.* The Journal of Chemical Physics, 1994. **100**(5): p. 3821-3826.
258. Gopalakrishnan, R., T. Thajudeen, and C.J. Hogan, *Collision Limited Reaction Rates for Arbitrarily Shaped Particles across the Entire Diffusive Knudsen Number Range.* Journal of Chemical Physics, 2011. **135**: p. 054302.
259. Klaus, M. and S. Malcolm, *Monte Carlo analysis of inverse problems.* Inverse Problems, 2002. **18**(3): p. R29.
260. Mosegaard, K. and A. Tarantola, *Monte Carlo sampling of solutions to inverse problems.* Journal of Geophysical Research: Solid Earth, 1995. **100**(B7): p. 12431-12447.
261. Ruta, S., R. Chantrell, and O. Hovorka, *Unified model of hyperthermia via hysteresis heating in systems of interacting magnetic nanoparticles.* Scientific Reports, 2015. **5**: p. 9090.
262. Chow, A.H.L., et al., *Particle engineering for pulmonary drug delivery.* Pharmaceutical Research, 2007. **24**(3): p. 411-437.
263. Hilding, J., et al., *Dispersion of carbon nanotubes in liquids.* Journal of Dispersion Science and Technology, 2003. **24**(1): p. 1-41.

264. Yu, W.W., et al., *Aqueous dispersion of monodisperse magnetic iron oxide nanocrystals through phase transfer.* Nanotechnology, 2006. **17**(17): p. 4483-4487.
265. Kim, J.W., L.U. Kim, and C.K. Kim, *Size control of silica nanoparticles and their surface treatment for fabrication of dental nanocomposites.* Biomacromolecules, 2007. **8**(1): p. 215-222.
266. Hasany, S.F., et al., *Magnetic Iron Oxide Nanoparticles: Chemical Synthesis and Applications Review.* Current Nanoscience, 2013. **9**(5): p. 561-575.
267. Ogi, T., A.B.D. Nandiyanto, and K. Okuyama, *Nanostructuring strategies in functional fine-particle synthesis towards resource and energy saving applications.* Advanced Powder Technology, 2014. **25**(1): p. 3-17.
268. Okuyama, K. and I.W. Lenggoro, *Preparation of nanoparticles via spray route.* Chemical Engineering Science, 2003. **58**(3-6): p. 537-547.
269. Stark, W.J. and S.E. Pratsinis, *Aerosol flame reactors for manufacture of nanoparticles.* Powder Technology, 2002. **126**(2): p. 103-108.
270. Strobel, R., A. Baiker, and S.E. Pratsinis, *Aerosol flame synthesis of catalysts.* Advanced Powder Technology, 2006. **17**(5): p. 457-480.
271. Muller, F., et al., *Dispersing nanoparticles in liquids.* International Journal of Mineral Processing, 2004. **74**: p. S31-S41.
272. Sommer, M., et al., *Agglomeration and breakage of nanoparticles in stirred media mills - a comparison of different methods and models.* Chemical Engineering Science, 2006. **61**(1): p. 135-148.
273. Peukert, W., H.C. Schwarzer, and F. Stenger, *Control of aggregation in production and handling of nanoparticles.* Chemical Engineering and Processing, 2005. **44**(2): p. 245-252.
274. Stenger, F., et al., *Nanomilling in stirred media mills.* Chemical Engineering Science, 2005. **60**(16): p. 4557-4565.
275. Inkyo, M., et al., *Experimental investigation of nanoparticle dispersion by beads milling with centrifugal bead separation.* Journal of Colloid and Interface Science, 2006. **304**(2): p. 535-540.

276. Inkyo, M., et al., *Beads mill-assisted synthesis of poly methyl methacrylate (PMMA)-TiO2 nanoparticle composites.* Industrial & Engineering Chemistry Research, 2008. **47**(8): p. 2597-2604.
277. Tahara, T., et al., *Change in Characteristics of Titania Nanoparticles during the Process of Dispersion, Agglomeration and Re-Dispersion with a Dual-Axis Beads-Mill.* Kagaku Kogaku Ronbunshu, 2013. **39**(5): p. 426-432.
278. Joni, I.M., et al., *Dispersion Stability Enhancement of Titania Nanoparticles in Organic Solvent Using a Bead Mill Process.* Industrial & Engineering Chemistry Research, 2009. **48**(15): p. 6916-6922.
279. Lee, S.H., et al., *Modeling of a bead mill process for dispersion of coagulated nano particles.* Powder Technology, 2013. **233**: p. 96-102.
280. Yoshio, S., et al., *Dispersion of carbon nanotubes in ethanol by a bead milling process.* Carbon, 2011. **49**(13): p. 4131-4137.
281. Jung, M.H., et al., *Dispersion behaviors of AlN nanoparticles in coolant oil by high speed bead-mill.* Journal of Ceramic Processing Research, 2011. **12**: p. S130-S133.
282. Jung, M., C. Choi, and J. Oh, *Optimum Operating Parameters of a Beads Mill for an AIN Containing Nanofluids.* Journal of Nanoscience and Nanotechnology, 2011. **11**(1): p. 507-510.
283. Yamamoto, T., et al., *AFM investigation of the surface properties of silica particles dispersed by bead milling.* Colloids and Surfaces a-Physicochemical and Engineering Aspects, 2010. **362**(1-3): p. 97-101.
284. Iskandar, F., et al., *Functional nanostructured silica powders derived from colloidal suspensions by sol spraying.* Journal of Nanoparticle Research, 2001. **3**(4): p. 263-270.
285. Iskandar, F., Mikrajuddin, and K. Okuyama, *Controllability of pore size and porosity on self-organized porous silica particles.* Nano Letters, 2002. **2**(4): p. 389-392.
286. Iskandar, F., et al., *Enhanced photocatalytic performance of brookite TiO2 macroporous particles prepared by spray drying with colloidal templating.* Advanced Materials, 2007. **19**(10): p. 1408-+.

287. Nam, K., et al., *Mechanical milling of catalyst support for enhancing the performance in fuel cells.* Powder Technology, 2011. **214**(3): p. 423-430.
288. Thajudeen, T. and C.J. Hogan, *Forced and natural convection in aggregate-laden nanofluids.* Journal of Nanoparticle Research, 2011. **13**(12): p. 7099-7113.
289. Thajudeen, T. and C.J. Hogan, *First Passage Calculation of the Conductivity of Particle Aggregate-Laden Suspensions and Composites* Powder Technology, 2012. **218**: p. 31-39.
290. Holthoff, H., et al., *Coagulation Rate Measurements of Colloidal Particles by Simultaneous Static and Dynamic Light Scattering.* Langmuir, 1996. **12**(23): p. 5541-5549.
291. Furushima, R., et al., *Quantitative analysis of de-aggregation behavior in alumina suspension by beads milling.* Powder Technology, 2012. **217**: p. 619-623.
292. Lattuada, M., et al., *Estimation of fractal dimension in colloidal gels.* Langmuir, 2003. **19**(15): p. 6312-6316.
293. Lattuada, M., H. Wu, and M. Morbidelli, *Hydrodynamic radius of fractal clusters.* Journal of Colloid and Interface Science, 2003. **268**(1): p. 96-105.
294. Lattuada, M., H. Wu, and M. Morbidelli, *A simple model for the structure of fractal aggregates.* Journal of Colloid and Interface Science, 2003. **268**(1): p. 106-120.
295. Kim, A.Y. and J.C. Berg, *Fractal Aggregation: Scaling of Fractal Dimension with Stability Ratio.* Langmuir, 1999. **16**(5): p. 2101-2104.
296. Inkyo, M. and T. Tahara, *Dispersion of agglomerated nanoparticles by micromedia mill, ultra apex mill.* J. Soc. Powder Technol. Jap., 2004. **41**.
297. Filipe, V., A. Hawe, and W. Jiskoot, *Critical Evaluation of Nanoparticle Tracking Analysis (NTA) by NanoSight for the Measurement of Nanoparticles and Protein Aggregates.* Pharmaceutical Research, 2010. **27**: p. 796.
298. Mansfield, M.L., J.F. Douglas, and E.J. Garboczi, *Intrinsic viscosity and the electrical polarizability of arbitrarily shaped objects.* Physical Review E, 2001. **64**(6): p. 61401.
299. Heine, D.R., M.K. Petersen, and G.S. Grest, *Effect of particle shape and charge on bulk rheology of nanoparticle suspensions.* The Journal of Chemical Physics, 2010. **132**(18): p. -.

300. Batchelor, G.K., *The effect of Brownian motion on the bulk stress in a suspension of spherical particles.* Journal of Fluid Mechanics, 1977. **83**(01): p. 97-117.
301. Russel, W.B., *The Huggins coefficient as a means for characterizing suspended particles.* Journal of the Chemical Society, Faraday Transactions 2: Molecular and Chemical Physics, 1984. **80**(1): p. 31-41.
302. Booth, F., *The Electroviscous Effect for Suspensions of Solid Spherical Particles.* Proceedings of the Royal Society of London. Series A. Mathematical and Physical Sciences, 1950. **203**(1075): p. 533-551.
303. Rubio-Hernández, F.J., et al., *Intrinsic viscosity of SiO2, Al2O3 and TiO2 aqueous suspensions.* Journal of Colloid and Interface Science, 2006. **298**(2): p. 967-972.
304. Latin, D., et al., *On methods determining the fractal dimension of combustion aerosols and particle clusters.* Journal of Aerosol Science, 2013. **58**: p. 41-49.
305. Thajudeen, T., S. Jeon, and C.J. Hogan, *The Mobilities of Flame Synthesized Aggregates/Agglomerates in the Transition Regime.* Submitted To: The Journal of Aerosol Science, 2014.
306. Etheridge, M.L., et al., *Accounting for biological aggregation in heating and imaging of magnetic nanoparticles.* Technology, 2014. **In Press**.
307. Cai, J., N.L. Lu, and C.M. Sorensen, *Analysis of Fractal Cluster Morphology Parameters - Structural Coefficient and Density Autocorrelation Function Cutoff.* Journal of Colloid and Interface Science, 1995. **171**(2): p. 470-473.
308. Filippov, A.V., M. Zurita, and D.E. Rosner, *Fractal-like Aggregates: Relation between Morphology and Physical Properties.* J. Colloid Interface Sci., 2000. **229**(1): p. 261-273.
309. Meakin, P., *Diffusion-Limited Aggregation in 3 Dimensions - Results From a New Cluster Aggregation Model.* Journal of Colloid and Interface Science, 1984. **102**(2): p. 491-504.
310. Hubbard, J.B. and J.F. Douglas, *Hydrodynamic Friction of Arbitrarily Shaped Brownian Particles.* Physical Review E, 1993. **47**(5): p. R2983-R2986.
311. Sorensen, C.M., *The Mobility of Fractal Aggregates: A Review.* Aerosol Science and Technology, 2011. **45**(7): p. 765-779.

312. Thajudeen, T., R. Gopalakrishnan, and C.J. Hogan, *The Collision Rate of Non-spherical Particles and Aggregates for all Diffusive Knudsen Numbers.* Aerosol Science and Technology, 2012. **46**(11): p. 1174-1186.
313. Duan, F., D. Kwek, and A. Crivoi, *Viscosity affected by nanoparticle aggregation in Al2O3-water nanofluids.* Nanoscale Research Letters, 2011. **6**(1): p. 1-5.